STOCHASTIC MODELING OF MULTIAXIAL FATIGUE AND FRACTURE

By

Yongming Liu

Dissertation

Submitted to the Faculty of the

Graduate School of Vanderbilt University

in partial fulfillment of the requirements

for the degree of

DOCTOR OF PHILOSOPHY

in

Civil Engineering

May, 2006

Nashville, Tennessee

Approved:

Professor Sankaran Mahadevan

Professor Prodyot K. Basu

Professor Carol Rubin

Professor William H. Hofmeister

To my wife and parents

ACKNOWLEDGEMENT

This work could not have been completed without the help from various people. I thank all my committee members for their guidance and suggestion from beginning to end. Especially, to my advisor, Dr. Sankaran Mahadevan, I am very grateful for your support and encouragement throughout my stay at Vanderbilt. I would like to thank Dr. Prodyot K Basu for his emotional support and advice during my graduate career. I truly appreciate both Brant Stratman and Liming Liu for their kind help and valuable discussions. Thanks to Robert Guratzsch, Ramesh Rebba, Ned Mitchell and all IGERT students for their encouragement and friendship. I also wish to acknowledge the helpful discussions and technical help from Dr. Shuping Huang and Dr. Xiaomo Jiang.

The research reported in this dissertation was supported by funds from Union Pacific Railroad and Meridian Railroad. The support is gratefully acknowledged. I also would like to thank Mr. Rex Beck and Dr. Todd Snyder for their guidance and advice during the completion of this work.

And finally thanks are owned to my wife and parents for their constant support and unwavering love. Without their support and love, I could never have succeeded.

TABLE OF CONTENTS

LIST OF TABLES

Page

LIST OF FIGURES

Page

CHAPTER I

INTRODUCTION

1.1 Overview

Many critical mechanical components experience multiaxial cyclic loadings during their service life, such as railroad wheels, crankshafts, axles, and turbine blades, etc. Different from the uniaxial fatigue problem, the multiaxial fatigue problem is more involved due to the complex stress states, loading histories and different orientations of the fatigue crack in the components. Fundamental understanding of multiaxial fatigue problem is essential for the reliability assessment under realistic service condition and is valuable for the design and maintenance against fatigue failure.

The fatigue process of mechanical components under service loading is stochastic in nature. Life prediction and reliability evaluation is still a challenging problem despite extensive progress made in the past decades. Compared to fatigue under constant amplitude loading, the fatigue modeling under stochastic loading becomes more complex both from deterministic and probabilistic points of view. An appropriate uncertainty modeling technique is required to include the stochasticity in both material properties and external loadings, which is critical in evaluating the long-term reliability of mechanical component.

Damage accumulation due to fatigue, plastic deformation and wear significantly reduce the service life of the railway track and wheels. In recent years, higher strain speeds and increased axle loads led to larger wheel/rail contact forces. Also, efforts have

been made to optimize wheel and rail design. This evolution tends to change the major wheel rim damage from wear to fatigue. Unlike the slow deterioration process of wear, fatigue causes abrupt fractures in wheels or material loss in the tread surface. These failures may cause damage to rails, damage to the train suspensions and, in rare case, serious derailments of the train. The failures may be very expensive in terms of human and economic loss. Thus, an accurate understanding of the underlying physical mechanism and a methodology to prevent fatigue failure have become important research needs for the railroad industry.

This study combines structural failure analysis, reliability methods, and advanced finite element method to develop a methodology for the reliability assessment of railroad wheels. Failure analysis focuses on developing fundamental multiaxial fatigue and fracture models to analyze the fatigue crack initiation and propagation behavior, and implement these methods with finite element analysis. Reliability analysis focuses on uncertainty quantification and propagation from laboratory conditions to service conditions. The randomness observed in the fatigue life of mechanical components is represented using the proposed numerical methods. Mechanics analysis is combined with limit state-based reliability analysis methods, inspection, testing, and failure data, to develop failure probability estimates of railroad wheels.

1.2 Research objectives

Based on the discussion above, the research objectives are summarized below:

1. Develop fundamental multiaxial fatigue and fracture models. Both crack initiation and propagation models are explored. As fundamental models for

fatigue damage evaluation, the models' performance against various materials and loading conditions is the major concern in the current study. The objective is to develop a general multiaxial model not only applicable to the railroad industry but also to many other situations.

2. Develop a general methodology for stochastic fatigue damage accumulation of mechanical/structural components. The major focus is on the uncertainty quantification and probabilistic life distribution under laboratory and realistic conditions. The objective is to integrate the randomness in material, applied loading and geometry to the proposed mechanical modeling, which can accurately and efficiently predict the long term reliability of mechanical components.

3. Develop a computational methodology for the complex rolling contact fatigue simulation of railroad wheels. Advanced finite element analysis, fatigue theory and fracture mechanics are combined. Due to the expensive computational effort in highly nonlinear finite element analysis, the major objective is to develop a suitable technique to simulate the fatigue and fracture processes efficiently and accurately.

4. Collect and analyze existing manufacturing, testing, inspection, and failure data in the open literature and from the Union Pacific database. One objective of this work is to validate the proposed multiaxial fatigue and fracture models for various materials. The other objective is to collect appropriate statistics as input random variables for reliability prediction and future inspection planning.

1.3 Advantages of the proposed methodology

Although numerous models for multiaxial fatigue analysis are available and some of them try to integrate randomness into reliability estimation, none of them have achieved universal acceptance, and many are limited in applicability. The proposed methodology is seen to have broad applicability, using a set of comparisons with the available methods in the literature and validations with the experimental results. Very few assumptions and empirical formulas are used in the proposed model. This feature of the proposed model makes it more attractive because it can be easily extended to the fatigue analysis of other mechanical systems.

The numerical simulation method of rail-wheel contact analysis is more accurate than classical contact theory results. The method is efficient in computation and can include many factors which are ignored by the classical contact theory. The finite element model is flexible and suitable in describing different types of motion of the railroad wheels, such as rotating, sliding, impacting and hunting movement. Both crack initiation and propagation are simulated and compared with field observations. The proposed methodology is seen to represent the failure behavior of railroad wheels very well, both qualitatively and quantitatively.

The reliability analysis method in this study includes both time and space variation. This methodology is especially suitable for large systems and complicated problems. The covariance structure of the fatigue damage accumulation process is considered and found to be important in reliability analysis, which is commonly ignored by previous existing models. The response surface method combined with Monte Carlo

simulation techniques used in the reliability analysis method can significantly reduce the calculation time.

1.4 Organization of the dissertation

The dissertation is organized as follows: In Chapter 2, fatigue life under multiaxial loading is predicted with the help of fundamental mechanicals modeling. The present work focuses on both fatigue crack initiation life and crack propagation life under proportional and non-proportional multiaxial loading. The terms “crack initiation” and “crack propagation” are somewhat unclear since both of them include crack growth and damage accumulation but on different scales. Usually, fracture mechanics is used to deal with crack propagation analysis and damage mechanics is used to deal with crack initiation analysis. Both crack initiation and propagation analysis are explored in this study. A new multiaxial fatigue theory is developed based on a characteristic plane approach. The results of crack initiation analysis and crack propagation analysis are combined together to predict the total life of materials under cyclic fatigue loading.

Chapter 3 focuses on the application of the proposed multiaxial fatigue theory to the rolling contact fatigue problem of railroad wheels. This problem differs from the usual fatigue problems in mechanical systems. The loading in rolling contact fatigue causes a non-proportional multiaxial stress state in railroad wheel. The principal stress direction in a fixed point rotates during one loading cycle. Traditional fatigue analysis cannot be applied to this type of loading. The fatigue crack initiation and propagation are subject to overall compressive loading, which is different from the “classical” fatigue problem (tensile stress state). The subsurface fatigue crack behavior is the major focus in

the current study and known as “shattered rim” failure. The failure pattern and crack profile is numerically simulated and compared with field data qualitatively. Several factors affecting the fatigue life of railroad wheels are explored in detail.

Chapter 4 focuses on the stochastic modeling of fatigue damage in the railroad wheels. Large variations and uncertainties in applied loadings, material properties, and environmental conditions cause much variation in wheel reliability and quality. One important benefit of this study is to develop a reliability-based inspection planning methodology. Accurate and efficient reliability calculation is a key factor in achieving this benefit. First, numerical simulation results from finite element analysis and fatigue analysis are used to construct the response surface of the fatigue damage index with respect to the geometry, loading, material properties and other random variables. Next, the Karhunen-Loeve expansion technique is applied for increased accuracy in describing the random damage field/process. Then a simulation-based method is used to estimate the reliability of railroad wheels under rolling contact fatigue loading. Finally, probabilistic life distribution using the proposed methodology is compared with field failure statistics.

CHAPTER II

MULTIAXIAL FATIGUE AND FRACTURE

2.1 Overview

The word fatigue originated from the Latin expression fatigue which means 'to tire'. The terminology used in engineering refers to the damage and failure of materials under cyclic loads, including mechanical loads, thermal loads, etc. Major advances have been made during the past hundred years in fatigue analysis. However, the application of fatigue concepts to practical situations encounters many complicated conditions and is far from final solution. These conditions include multiaxial stress state, stochastic load spectra, detrimental environments, etc (Suresh, 1998). Fatigue failure is one the most important failure modes of mechanical components, including railroad wheels. Fatigue failure can significantly reduce the system reliability and durability and cause economic and human lose. Table 1 summarizes the types of fatigue analysis for different conditions.

Many critical mechanical components experience multiaxial cyclic loadings during their service life, such as railroad wheels, crankshafts, axles, turbine blades, etc. Different from the uniaxial fatigue problem, the multiaxial fatigue problem is more complex due to the complex stress states, loading histories and different orientations of the initial crack in the components. The railroad wheel fatigue problem belongs to high-cycle multiaxial fatigue and includes both fatigue crack initiation and fatigue crack propagation. The main objective of this chapter is to develop a general methodology for

fundamental multiaxial fatigue analysis, which is to be used for railroad wheel fatigue life prediction in Chapter 3.

Table 1. Classification of various types of fatigue analysis

Classification basis	Fatigue analysis type	Description
Loading	Uniaxial	One cyclic stress or strain component dominates during the life
	Multiaxial	Multiaxial cyclic stress or strain components dominates during the life
Fatigue life	High-cycle	Fatigue life $>10^{3\sim4}$ cycles
	Low-cycle	Fatigue life $<10^{3\sim4}$ cycles
Damage stage	Crack initiation	From no macro crack to macro crack
	Crack propagation	From macro crack to final failure
Analysis approach	Stress-life approach (S-N)	Stress is used to predict fatigue life
	Strain-life approach (e-N)	Strain is used to predict fatigue life
	Energy approach	Energy is used to predict fatigue life
	Fracture mechanics approach (K, J, COD)	Fracture parameters are used to predict fatigue life

2.2 Stress-based high cycle multiaxial fatigue crack initiation

In recent decades, numerous studies have attempted to develop multiaxial fatigue damage criteria. Several reviews and comparisons of existing multiaxial fatigue models can be found elsewhere (Garud, 1981; You and Lee, 1996; Papadopoulos, 1997; Wang and Yao, 2004). Despite the differences in different multiaxial models, the general idea is similar, which is to reduce the complex multiaxial stress state to an equivalent uniaxial stress state or an equivalent damage scalar. Thus the fatigue life is assessed based on the

equivalent parameter. All fatigue damage models for crack initiation analysis can be classified into three groups: stress approach, strain approach and energy approach (Wang and Yao, 2004). The stress approach has been commonly used for high-cycle fatigue problems.

Although there are many proposed models for multiaxial fatigue damage modeling, most of them are limited to specific materials or loading conditions. Some of them cannot predict the initial crack orientation, which is another distinct characteristic of multiaxial fatigue damage compared with the uniaxial fatigue problem. To the author's knowledge, no existing multiaxial fatigue damage model is universally accepted.

In recent years, criteria based on the critical plane approach for multiaxial fatigue evaluation are becoming more popular because they generally give more accurate predictions of the fatigue damage (Socie, 1989; You and Lee, 1996). According to this approach, the fatigue evaluation is performed on one plane across a critical location in the component. This plane is called the critical plane, which is usually different for different fatigue models. However, one disadvantage of the common critical plane approach is that the definition of the critical plane is often related to the maximum value of one stress component or the combination of several stress components. It is doubtful whether the critical plane only depends on the stress state and has no relation with the material properties. Carpinteri and Spagnoli (2001) gave a new definition of the critical plane considering both the stress state and the material properties. However, their proposed formula is empirical and can be applied only to a range of metals.

In this section, first several high-cycle fatigue damage models are briefly discussed. Then a new fatigue criterion based on characteristic plane approach is

proposed. Unlike the previous critical plane approaches, the characteristic plane in the current model is theoretically correlated with the fatigue crack initiation plane and also depends on the material properties. Next a correction factor considering the effect of the mean stress is introduced. The current model is compared with other existing criteria using the available experimental data in the literature. The fatigue criterion is then extended to predict the fatigue life under multiaxial loading conditions. The predicted lives are compared with experimental observations in the literature.

2.2.1 Existing high-cycle multiaxial fatigue criterion

Since the main focus of this section is multiaxial high-cycle fatigue problem, only the stress-based approach is reviewed in this section. Strain-based approach for low-cycle fatigue will be covered in the next section. The stress-based approaches can be divided into four groups based on empirical equivalent stress, stress invariants, average stress and critical plane stress.

In the empirical equivalent stress approach, the criteria based on yield theories are most often used because of the simplicity of the formula. Langer (1979) proposed an equivalent stress based on the Tresca equivalent stress. For sinusoidal, fully-reversed, out-of-phase bending and torsion, the equivalent stress amplitude (SALT) is:

$$SALT = \frac{\sigma_a}{\sqrt{2}}\left[1 + K^2 + \left(1 + 2K^2\cos(2\phi) + K^4\right)^{\frac{1}{2}}\right]^{\frac{1}{2}} \quad (1)$$

where: σ_a is the bending stress amplitude, τ_a is the torsion stress amplitude, $K = 2\tau_a / \sigma_a$ and ϕ is the phase angle between bending and torsion. For proportional loading ($\phi = 0$), Eq. (1) reduces to Tresca stress:

$$SALT = \sqrt{\sigma_a^2 + 4\tau_a^2} \quad (2)$$

A modified Langer's Method, which is based on Von Mises equivalent stress, is expressed as: (ASME, 1978)

$$SEQA = \frac{\sigma_a}{\sqrt{2}}[1 + \frac{3}{4}K^2 + (1 + \frac{3}{2}K^2 \cos(2\phi) + \frac{9}{16}K^4)^{\frac{1}{2}}]^{\frac{1}{2}} \qquad (3)$$

For proportional loading ($\phi = 0$), Eq. (3) reduces to the Von Mises stress:

$$SALT = \sqrt{\sigma_a^2 + 3\tau_a^2} \qquad (4)$$

Another popularly used formula is suggested by Gough and Pollard (1935, 1951).

For a ductile material, the fatigue criterion follows an eclipse equation:

$$\frac{\sigma_a^2}{f_{-1}^2} + \frac{\tau_a^2}{t_{-1}^2} = 1 \qquad (5)$$

For a brittle material, the fatigue criterion follows the equation:

$$(\frac{f_{-1}}{t_{-1}} - 1)\frac{\sigma_a^2}{f_{-1}^2} + (2 - \frac{f_{-1}}{t_{-1}})\frac{\sigma_a}{f_{-1}} + \frac{\tau_a^2}{t_{-1}^2} = 1 \qquad (6)$$

where f_{-1} and t_{-1} are fatigue limits in fully reversed bending and torsion, respectively. If we rewrite Eq. (5) as

$$\sqrt{\sigma_a^2 + \frac{f_{-1}^2}{t_{-1}^2}\tau_a^2} = f_{-1} \qquad (7)$$

The left hand side of Eq. (7) can be treated as an equivalent stress amplitude. For a material with $t_{-1} / f_{-1} = 0.5$, Eq. (7) coincides with the equivalent Tresca stress (Eq. (2)). For material with $t_{-1} / f_{-1} = 1/\sqrt{3}$, Eq. (7) coincides with the equivalent Von Mises stress (Eq. (4)).

Lee (1985) proposed an empirical equivalent stress based on Gough's formula as follows:

$$SLEE = \sigma_a [1 + (\frac{f_{-1}}{2t_{-1}} K)^{2(1+\beta \sin\phi)}]^{\frac{1}{2(1+\beta \sin\phi)}} \quad (8)$$

where β is material constant need to be calibrated using experimental data.

The empirical equivalent stress approach is easy to calculate and convenient for engineering application. However, it has been shown that the results based on Tresca or Von Mises stresses are non-conservative (You and Lee, 1996). Gough's formula can only be used for proportional loading conditions. Lee's formula has a material constant which requires extra experimental work and thus limits the application of the method.

The basic idea in the stress invariants approach is to directly relate the fatigue strength with the second invariant of the stress deviator and first invariant of the stress (3 times the hydrostatic stress). The general form is as follows:

$$f((J_1)_a, (J_2')_a, (J_1)_m, (J_2')_m) = \xi \quad (9)$$

where

$$J_1 = \sigma_1 + \sigma_2 + \sigma_3 \quad (10)$$

$$J_2' = \frac{1}{6}[(\sigma_1 - \sigma_2)^2 + (\sigma_2 - \sigma_3)^2 + (\sigma_3 - \sigma_1)^2] \quad (11)$$

The subscripts a and m in Eq. (9) refer to the stress amplitude value and mean stress value respectively; ξ is a material constant calibrated using fatigue experiments.

Sines (1959) gave a popular criterion based on $(J_1)_m$ and $(J_2')_a$ as:

$$\sqrt{(J_2')_a} + \lambda (J_1)_m = \xi \quad (12)$$

where $\lambda = (3t_{-1} - \sqrt{3} f_{-1}^m) / \sigma_m$, $\xi = t_{-1}$ and f_{-1}^m is the uniaxial fatigue limit with mean stress σ_m.

Crossland (1956) suggested that fatigue evaluation should consider the maximum value of the hydrostatic stress:

$$\sqrt{(J_2^{'})_a} + \lambda[(J_1)_m + (J_1)_a] = \xi \qquad (13)$$

Kakuno and Kawada (1979) suggested that the contribution of $(J_1)_m$ and $(J_1)_a$ should be different:

$$\sqrt{(J_2^{'})_a} + \kappa(J_1)_m + \lambda(J_1)_a = \xi \qquad (14)$$

where in Eq. (12) to (14), λ, ξ and κ are material constants, which are generally different for different models.

One limitation of the stress invariant approach is that the orientation of the initial crack cannot be predicted (Papadopoulos, 1997). The other drawback is that non-conservative results may be obtained (You and Lee, 1996). The other issue is that, although not clearly stated in the equation, some methods based on this approach can only be applied to a range of metals. For example, in Crossland's criterion, λ equals $(3t_{-1}/f_{-1} - \sqrt{3})$. Considering that the tensile mean stress will reduce the fatigue limit. λ should be positive, ie., $t_{-1}/f_{-1} > 1/\sqrt{3}$. Thus Crossland's criterion can only be applied to metals with $t_{-1}/f_{-1} > 1/\sqrt{3}$.

The average stress approach uses an average of the stress components involving the critical point. This quantity is treated as an equivalent stress and correlated to the fatigue damage. Papadopoulos (1997) gave a simple formula through a complex double integral calculation:

$$\sqrt{\langle T_a^2 \rangle} + \lambda[(J_1)_a + (J_1)_m] = \sqrt{\frac{\sigma_a^2}{3} + \tau_a^2} + \lambda[(J_1)_a + (J_1)_m] = \xi \qquad (15)$$

where $\left\langle T_a^2 \right\rangle$ is the average quantity within a volume, $\lambda = (3t_{-1} / f_{-1} - \sqrt{3})$ and $\xi = t_{-1}$.

The formula looks similar with the Crossland's criterion except the second invariant of the stress deviator is replaced by the average stress quantity. It also has the limitation of the material. As stated by Papadopoulos, t_{-1} / f_{-1} is better to be between 0.577 and 0.8. The other limitation of the model is that non-proportional loading has no effect based on Eq. (15), which is in conflict with experimental observations (You and Lee, 1996).

Papadopoulos (2001) improved the model using a critical plane type model:

$$\max(T_a^{\Delta}) + \lambda[(J_1)_a + (J_1)_m] = \xi \qquad (16)$$

where T_a^{Δ} is an average stress quantity (named generalized shear stress amplitude by Papadopoulos) on the critical plane Δ. The critical plane is defined as the plane Δ where T_a achieves the maximum value. For this model, although stated by the author that no particular form is required for the basic fatigue S-N curve, there does seem to be an implicit assumption that the uniaxial S-N curve is parallel to the torsional S-N curve. Generally this assumption holds for some materials or for the life regime close to the fatigue limit life.

The other average stress approaches can be found elsewhere (e.g. Liu and Zenner, 1993; Grubisic and Simburger, 1976).

The concept of the critical plane approach is very simple and convenient to apply to the multiaxial fatigue problem. Despite the different definitions of the critical plane in different methods, the general methodology is the same. First a material plane is determined, and then the fatigue damage is evaluated using one or a combination of the stress components on the critical plane. Although there are some critiques on the critical

plane approach, the results based on this approach have been shown to have a good correlation with the experimental observations.

Findley (1959) proposed a damage parameter based on the linear combination of the shear stress amplitude and maximum normal stress acting on the critical plane. The critical plane is defined as the plane where the damage parameter achieves the maximum value:

$$\begin{cases} (\phi_c, \theta_c) = \max\limits_{(\phi,\theta)} [\tau_a(\phi,\theta) + k\sigma_{\max}(\phi,\theta)] \\ \tau_a(\phi_c, \theta_c) + k\sigma_{\max}(\phi_c, \theta_c) = \xi \end{cases} \quad (17)$$

where the material constants k and ξ are computed as:

$$k = (2 - f_{-1}/t_{-1})/(2\sqrt{f_{-1}/t_{-1} - 1}); \xi = \sqrt{(f_{-1})^2/(4f_{-1}/t_{-1} - 4)} \quad (18)$$

Matake (1977) uses the same form of the damage parameter as Findley but defines the critical plane as the plane on which the shear stress amplitude achieves the maximum value:

$$\begin{cases} (\phi_c, \theta_c) = \max\limits_{(\phi,\theta)} [\tau_a(\phi,\theta)] \\ \tau_a(\phi_c, \theta_c) + k\sigma_{\max}(\phi_c, \theta_c) = \xi \end{cases} \quad (19)$$

where the material constants k and ξ are given as:

$$k = (2t_{-1}/f_{-1} - 1); \xi = t_{-1} \quad (20)$$

McDiarmid (1991) uses the concept of case A and case B cracks (Brown and Millar, 1973). Case A cracks propagate along the component surface, while case B cracks propagate inwards the surface. The fatigue damage is evaluated on the critical plane corresponding to the two crack cases. The critical plane is defined same as in Matake's model.

$$\begin{cases} (\phi_c, \theta_c) = \max\limits_{(\phi,\theta)}[\tau_a(\phi,\theta)] \\ \tau_a(\phi_c,\theta_c) + \dfrac{\tau_{A,B}}{2\sigma_u}\sigma_{\max}(\phi_c,\theta_c) = \tau_{A,B} \end{cases} \quad (21)$$

where $\tau_{A,B}$ is the material parameter according to case A or case B cracks, σ_u is the ultimate tensile strength of the material.

Carpinteri and Spagnoli (2001) proposed a criterion based on the critical plane for hard metals. The calculation of the critical plane is performed in two steps. First the weighted mean direction of the maximum principal stress is evaluated (Carpinteri et al, 1999(a), Carpinteri et al, 1999(b)). This direction is also believed to be the initial fatigue fracture plane. Then an empirical formula is used to correlate the critical plane to the fatigue fracture plane. After determining the critical plane, the fatigue criterion is expressed by a nonlinear combination of the maximum normal stress and shear stress amplitude acting on the critical plane.

$$\begin{cases} \delta = 45\dfrac{3}{2}[1-(\dfrac{t_{-1}}{f_{-1}})^2] \\ (\dfrac{\sigma_{\max}}{f_{-1}})^2 + (\dfrac{\tau_a}{t_{-1}})^2 = 1 \end{cases} \quad (22)$$

where δ is the angle between w_c and l_c in degrees, w_c is the normal vector of the critical plane, l_c is the direction of the weighted mean direction of the maximum principle stress.

Some of the critical plane methods have the limitations with respect to the applicable range of the material properties. For Findley's criterion, t_{-1}/f_{-1} should be less than one. For the model suggested by Carpinteri and Spagnoli (2001), t_{-1}/f_{-1} should be between 0.577 and 1. Another aspect of the critical plane approach is that most of the critical plane definitions only depend on the stress state. Carpinteri and Spagnoli define

the critical plane which depends on both stress state and material properties. But the relation between fatigue fracture plane and critical plane is purely empirical, which is a parabolic interpolation between two assumed values.

2.2.2 Proposed new multiaxial fatigue model

The definitions of the fatigue fracture plane and the characteristic plane should be clarified first. Experimental results show that for commonly used metallic materials, fatigue crack first occurs along the crystal slip plane, and then propagates perpendicular to the maximum principal stress direction. The fatigue fracture plane here refers to the crack plane observed at the macro level. The characteristic plane is not an actual crack plane. It is a material plane on which the fatigue damage is evaluated. The two planes may or may not coincide with each other. Several authors proposed different methods to predict the fatigue fracture plane. McDiarmid (1991) defines the fracture plane as the plane which experiences the maximum principal stress. Carpinteri et al (1999(a), 1999(b)) suggest that the fracture plane coincides with the weighted mean principal stress direction. Socie (1987) proposed to correlate the fatigue fracture plane to either a Mode I crack or a Mode II growth mechanism. Here in this chapter, the fatigue fracture plane is assumed to be the plane which experiences the maximum normal stress amplitude.

The characteristic plane orientation may differ from the fatigue fracture plane for different materials. However, in this chapter, it is not arbitrarily assumed. The calculation of the characteristic plane orientation is derived as below.

First consider the fully reversed bending-torsion fatigue problem (with no mean stress). A new fatigue damage parameter is proposed based on the nonlinear combination

of the normal stress amplitude, shear stress amplitude and hydrostatic stress amplitude acting on the characteristic plane, as

$$\sqrt{(\frac{\sigma_{a,c}}{f_{-1}})^2+(\frac{\tau_{a,c}}{t_{-1}})^2+k(\frac{\sigma^H_{a,c}}{f_{-1}})^2}=\beta \qquad (23)$$

where $\sigma_{a,c}$, $t_{a,c}$ and $\sigma^H_{a,c}$ are the normal stress amplitude, shear stress amplitude and hydrostatic stress amplitude acting on the characteristic plane respectively. k and β are material parameters which can be determined by uniaxial and torsional fatigue limits.

It should be noted that the expression in Eq. (23) is not a required assumption of the current methodology. The damage parameter can also be assumed as linear or other combinations of the stress amplitudes. If a different damage parameter is used, a different fatigue damage model can be obtained following the procedure described in this section.

Since the relationship between the characteristic plane and fatigue fracture plane has not been determined yet, suppose that for one type of material the characteristic plane coincides with the fatigue fracture plane. In other words, the angle between these two planes is zero.

For a fully reversed uniaxial fatigue experiment $(\sigma_a = f_{-1}, \tau_a = 0)$, the fatigue fracture plane is perpendicular to the normal stress direction. Thus we obtain:

$$\begin{cases}\sigma_{a,c} = f_{-1}\\ \tau_{a,c} = 0\\ \sigma^H_{a,c} = f_{-1}/3\end{cases} \qquad (24)$$

For a fully reversed pure torsional fatigue experiment $(\sigma_a = 0, \tau_a = t_{-1})$, the fatigue fracture plane has an angle of 45 degrees with the shear stress direction. Thus

$$\begin{cases} \sigma_{a,c} = t_{-1} \\ \tau_{a,c} = 0 \\ \sigma_{a,c}^{H} = 0 \end{cases} \tag{25}$$

Substitute Eq. (24) and (25) to Eq. (23), we can get:

$$\begin{cases} \sqrt{1 + \frac{k}{9}} = \beta \\ \sqrt{\left(\frac{t_{-1}}{f_{-1}}\right)^2} = \beta \end{cases} \tag{26}$$

Solve Eq. (26) for material parameters.

$$\begin{cases} k = 9[(\frac{t_{-1}}{f_{-1}})^2 - 1] \\ \beta = \frac{t_{-1}}{f_{-1}} \end{cases} \tag{27}$$

Notice that the physical meaning of k is the contribution of damage caused by the hydrostatic stress amplitude. It should be non-negative. So t_{-1} / f_{-1} should not be less than one. Materials with $t_{-1} / f_{-1} \le 1/\sqrt{3}$ are usually known as ductile (mild) metals. For Materials with $1/\sqrt{3} \le t_{-1} / f_{-1} \le 1$ are usually known as brittle (hard) metals (Carpinteri and Spagnoli, 2001). Materials with $t_{-1} / f_{-1} \ge 1$ are referred as extremely brittle (hard) metals in this chapter. Recall the assumption made before this calculation. It is only possible for an extremely brittle material ($t_{-1} / f_{-1} \ge 1$) that the characteristic plane coincides with the fatigue fracture plane using the present damage parameter (Eq. (23)). It is also interesting to notice that k equals zero when $t_{-1} / f_{-1} = 1$, which means (from Eq. (23)) that the hydrostatic stress amplitude has no contribution to the fatigue damage for this material according to the present definition of the damage parameter (Eq. (23)).

Now suppose that for one type of material, the characteristic plane is 45 degrees off the fatigue fracture plane, which is the maximum shear stress plane for uniaxial and torsional loading. Following the steps described above, the material parameters k and β are once again calculated.

For a fully reversed uniaxial fatigue experiment $(\sigma_a = f_{-1}, \tau_a = 0)$, the stress components on the characteristic plane are

$$\begin{cases} \sigma_{a,c} = f_{-1} / 2 \\ \tau_{a,c} = f_{-1} / 2 \\ \sigma_{a,c}^{H} = f_{-1} / 3 \end{cases} \tag{28}$$

For a fully reversed pure torsional fatigue experiment $(\sigma_a = 0, \tau_a = t_{-1})$, the stress components on the characteristic plane are

$$\begin{cases} \sigma_{a,c} = 0 \\ \tau_{a,c} = t_{-1} \\ \sigma_{a,c}^{H} = 0 \end{cases} \tag{29}$$

Substituting Eqs. (28) and (29) in Eq. (23):

$$\begin{cases} \sqrt{\dfrac{1}{4} + \dfrac{f_{-1}^{\,2}}{4 t_{-1}^{\,2}} + \dfrac{k}{9}} = \beta \\ 1 = \beta \end{cases} \tag{30}$$

Solving Eq. (30) for the material parameters, we obtain:

$$\begin{cases} k = \dfrac{3}{2} \sqrt{3 - \left(\dfrac{f_{-1}}{t_{-1}} \right)^2} \\ \beta = 1 \end{cases} \tag{31}$$

From Eq. (31), t_{-1} / f_{-1} should not be less than $1/\sqrt{3}$. This type of material $(t_{-1} / f_{-1} \geq 1/\sqrt{3})$ is often known as a brittle (hard) metal. Recall the assumption made

before this calculation. Thus, it is only possible for brittle metals ($t_{-1} / f_{-1} \geq 1/\sqrt{3}$) that the characteristic plane could be 45 degrees off the fatigue fracture plane using the present damage parameter. Similar to the first case, k equals zero when $f_{-1} / t_{-1} = \sqrt{3}$, which means (From Eq. (23)) that the hydrostatic stress amplitude $\sigma_{a,c}^{H}$ has no contribution to the fatigue damage for this material according to the present definition of the damage parameter.

Several conclusions can be drawn based on the derivations of the characteristic plane orientations for the two cases above. The contribution of the hydrostatic stress amplitude is different for different materials if the characteristic plane is fixed for all materials. There are two materials ($t_{-1} / f_{-1} = 1$ and $t_{-1} / f_{-1} = 1/\sqrt{3}$), for which the contribution of the hydrostatic stress amplitude is zero if the characteristic plane is defined as shown in these two cases. It is also noticed that, if the characteristic plane is fixed, the range of applicable material parameters are limited.

Instead of fixing the characteristic plane, the current model searches for the characteristic plane orientations on which the contribution of the hydrostatic stress amplitude is minimized to zero. This is a general approach that can be applied to all material.

For an arbitrary material, let the angle between the characteristic plane and the fatigue fracture plane be α. Since the contribution of the hydrostatic stress amplitude is zero, Eq. (23) is rewritten as:

$$\sqrt{(\frac{\sigma_{a,\alpha}}{f_{-1}})^2 + (\frac{\tau_{a,\alpha}}{t_{-1}})^2} = \beta \qquad (32)$$

The objective is to find α and β for an arbitrary material, following the steps described for the first two cases.

For a fully reversed uniaxial fatigue experiment $(\sigma_a = f_{-1}, \tau_a = 0)$, the fatigue fracture plane is perpendicular to the normal stress direction. The characteristic plane is at an angle α off the fatigue fracture plane. Thus, we obtain:

$$\begin{cases} \sigma_{a,\alpha} = \dfrac{f_{-1}}{2} \pm \dfrac{f_{-1}}{2} cos(2\alpha) \\ \tau_{a,\alpha} = \pm \dfrac{f_{-1}}{2} sin(2\alpha) \end{cases} \quad (33)$$

For fully reversed pure torsional fatigue experiment $(\sigma_a = 0, \tau_a = t_{-1})$, the characteristic plane is at an angle α degree off the maximum normal stress plane. Thus:

$$\begin{cases} \sigma_{a,\alpha} = \pm t_{-1} cos(2\alpha) \\ \tau_{a,\alpha} = \pm t_{-1} sin(2\alpha) \end{cases} \quad (34)$$

Substituting Eqs. (33) and (34) in Eq. (32),

$$\begin{cases} \dfrac{[1 \pm cos(2\alpha)]^2}{4} + \dfrac{1}{4}(\dfrac{f_{-1}}{t_{-1}})^2 sin^2(2\alpha) = \beta^2 \\ (\dfrac{t_{-1}}{f_{-1}})^2 cos^2(2\alpha) + sin^2(2\alpha) = \beta^2 \end{cases} \quad (35)$$

Solving Eq. (35) for α and β, we obtain

$$\begin{cases} cos(2\alpha) = \dfrac{-2 + \sqrt{4 - 4(1/s^2 - 3)(5 - 1/s^2 - 4s^2)}}{2(5 - 1/s^2 - 4s^2)} \\ \beta = [cos^2(2\alpha)s^2 + sin^2(2\alpha)]^{\frac{1}{2}} \end{cases} \quad (36)$$

where $s = \dfrac{t_{-1}}{f_{-1}}$ is a material constant. Here α takes values from 0 to $\dfrac{\pi}{2}$. As shown in Eq. (36), both α and β are the functions of the material property s. It is found that α

increases as s decreases. α equals 0 when s equals 1, and α equals $\frac{\pi}{2}$ when s equals zero. β does not change monotonically with respect to s, but all the β values are close to 1 for materials with $1/\sqrt{3} < s < 1$.

From Eq. (36), α has no real solution for $s > 1$. This indicates that for an extremely brittle material, the contribution of hydrostatic stress amplitude cannot be minimized to zero and must be considered during the fatigue damage evaluation. We use the results in case 1 for the material with $s > 1$. The summary of material parameters for all types of materials are listed in Table 2.

As a result of the above derivation, the methodology becomes very simple with the current model. First the plane with maximum normal stress amplitude is identified during one stress cycle. For an arbitrary loading history, the plane is searched numerically by checking the normal stress amplitude on all possible planes. In this chapter, an angle increment of 1 degree is used during the numerical computation. Then the characteristic plane and material parameters are determined for different materials according to Table 2. Finally the stress components on the characteristic plane are calculated and the fatigue damage is evaluated using Eq. (23).

Practical mechanical components generally experience cyclic fatigue loading together with the mean stress. The mean stress could also be introduced by residual stress, environmental effects, etc. It is well known that the mean normal stress has an important effect on fatigue life. Normally, tensile mean stress reduces the fatigue life, while compressive mean stress increases the fatigue life (Sines, 1961).

There are many models for mean normal stress effect correction. Gerber (1874), Goodman (1899), Soderberg (1939) and Morrow (1969) proposed different correction

factors. Kujawski and Ellyin (1995) proposed a unified approach to mean. For the multiaxial fatigue problem, mean normal stress is included in the model in different ways (Socie, 2000) depending on different models. Fatemi and Socie (1988) considered the maximum normal stress acting on the critical plane. Papadopoulos (1997) considered the hydrostatic mean stress. Farahani (2000) used a correction factor based on the mean stress on the critical plane.

Table 2. Material parameters for fatigue damage evaluation

Material Property	$s = \frac{t_{-1}}{f_{-1}} \le 1$	$s = \frac{t_{-1}}{f_{-1}} > 1$
α	$cos(2\alpha) = \frac{-2+\sqrt{4-4(1/s^2-3)(5-1/s^2-4s^2)}}{2(5-1/s^2-4s^2)}$	$\alpha = 0$
k	$k = 0$	$k = 9(s^2-1)$
β	$\beta = [cos^2(2\alpha)s^2 + sin^2(2\alpha)]^{\frac{1}{2}}$	$\beta = s$

In the case of mean shear stress effect, there is still much argument as to the proper way to include this effect. From many experimental observations, Smith (1942) concluded that mean shear stress has little effect on the fatigue life and endurance limit. Sines (1959) stated that a superimposed mean static torsion has no effect on the fatigue limit of metals subjected to cyclic torsion. A similar conclusion was also found by Davoli et al (2003). The mean shear stress effect is often neglected in the high cycle fatigue analysis (Davoli et al 2003). Therefore in the current model, the mean shear stress is also assumed to have no effect on the fatigue criterion and fatigue life in high-cycle fatigue regime. Based on the experimental data collected from the literature, the mean stress is

introduced to the fatigue model by a correction factor $(1+\eta\frac{\sigma_{m,c}}{f_{-1}})$. Thus, Eq. (23) is rewritten as:

$$\sqrt{[\frac{\sigma_{a,c}(1+\eta\frac{\sigma_{m,c}}{f_{-1}})}{f_{-1}}]^2+(\frac{\tau_{a,c}}{t_{-1}})^2+k(\frac{\sigma_{a,c}^H}{f_{-1}})^2}=\beta \qquad (37)$$

where η is a material parameter, which can be calibrated using uniaxial fatigue tests with mean stress. For different materials used in this chapter, η ranges from 0.60 to 1.3. If fatigue tests with mean stress are not available, a simplified function (Eq. (38)) is suggested. The experimental value and the simplified formula of η are plotted in Fig. 1.

$$\begin{cases}\eta=\frac{3}{4}+\frac{1}{4}(\frac{\sqrt{3}-\frac{f_{-1}}{t_{-1}}}{\sqrt{3}-1}) & (\frac{t_{-1}}{f_{-1}}\le 1)\\ \eta=1 & (\frac{t_{-1}}{f_{-1}}\ge 1)\end{cases} \qquad (38)$$

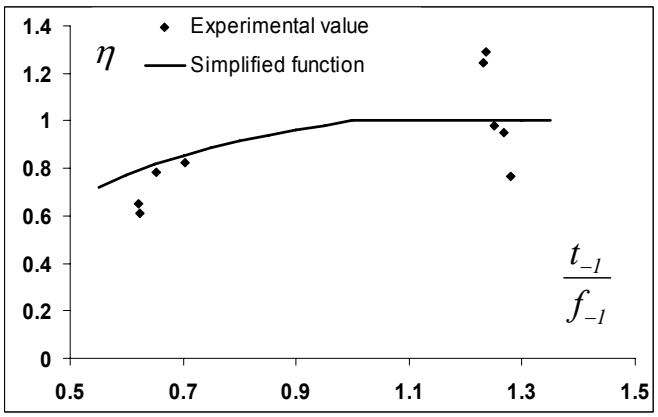

Fig. 1 Experimental value and simplified value of mean stress factor

After developing the fatigue limit criterion as above, the methodology for fatigue life prediction is relatively easy. Notice that the fatigue limit is often referred to the fatigue strength at very high cycle (usually 10^6 ~10^7 cycles). For finite fatigue life prediction, the damage parameter should be correlated with the life (number of loading cycles). Eq. (37) can be rewritten as

$$\frac{1}{\beta}\sqrt{[\sigma_{a,c}(1+\eta\frac{\sigma_{m,c}}{f_{-1}})]^2+(\frac{f_{-1}}{t_{-1}})^2(\tau_{a,c})^2+k(\sigma_{a,c}^H)^2}=f_{-1} \qquad (39)$$

The left hand side of Eq. (39) can be treated as an equivalent stress amplitude. It can be used to correlate with the fatigue life using the uniaxial S-N curve. Thus the fatigue life model is expressed as:

$$\frac{1}{\beta}\sqrt{[\sigma_{a,c}(1+\eta_{N_f}\frac{\sigma_{m,c}}{f_{N_f}})]^2+(\frac{f_{N_f}}{t_{N_f}})^2(\tau_{a,c})^2+k(\sigma_{a,c}^H)^2}=f_{N_f} \qquad (40)$$

and

$$\begin{cases}\eta_{N_f}=\dfrac{3}{4}+\dfrac{1}{4}\left(\dfrac{\sqrt{3}-\dfrac{f_{N_f}}{t_{N_f}}}{\sqrt{3}-1}\right) & \left(\dfrac{f_{N_f}}{t_{N_f}}>1\right)\\ \eta_{N_f}=1 & \left(\dfrac{f_{N_f}}{t_{N_f}}\le 1\right)\end{cases} \qquad (41)$$

where N_f is the number of cycles to failure. Notice here f_{-1} and t_{-1} in Eq. (37) and Eq. (38) change to f_{N_f} and t_{N_f} respectively, which are fatigue strength coefficients at finite life N_f for uniaxial and torsional loadings. Eq. (40) has no closed form solution. In practical calculation, a trial and error method can be used to find N_f. For high cycle fatigue, f_{N_f} and t_{N_f} take initial values as f_{-1} and t_{-1}. It is found that usually a few

iterations are enough to make N_f converge. Eq. (40) and Eq. (41) together with the parameters in Table 2 are used for fatigue life prediction in this chapter. The quantity s in Table 2 is redefined as $s = \frac{t_{N_f}}{f_{N_f}}$.

2.2.3 Comparison with experimental observations

Two sets of bending and torsion experimental fatigue limit data are used to validate the current fatigue criterion in this section. The first one contains four different materials (Papadopoulos et al, 1997). Some material properties are reported in Table 3. The error index of the current model is compared with three other models: Matake's (1977), McDiarmid's (1991) and Papadopoulos's (1997). The error index is defined same as in Papadopoulos (1997): the relative difference between the left and right hand sides of each criterion.

$$I = \frac{left\ hand\ side - right\ hand\ side}{right\ hand\ side}(\%) \qquad (42)$$

Table 3. Material properties employed by Papadopoulos (1997)

Material	f_{-1} (Mpa)	t_{-1} (Mpa)	t_{-1} / f_{-1}	σ_u (Mpa)
Hard Steel	313.9	196.2	0.63	680
42CrMo4	398	260	0.65	1025
34Cr4	410	256	0.62	795
30NCD16	660	410	0.62	1880

The experimentally observed fatigue fracture plane orientations are not reported by Papadopoulos (1997). Only the experimental fatigue limit data are compared with the model predictions. The main objective of the comparison is to find the model's applicability to different materials and loading conditions. So the comparisons here are

performed using the mean absolute error for different phase differences according to different materials through Fig. 2.

In Fig. 2, it is seen that both the Papadopoulos' model and the proposed model give a good estimation of the fatigue limit. For some materials, the results of the proposed model give slightly smaller errors, while for others Papadopoulos' results are better. Both Matake's model and McDiarmid's model give a relatively larger error. It also seems that the error in McDiarmid's model increases as the phase difference increases. Notice that the t_{-1} / f_{-1} values of all the materials fall into a very small range (0.62~0.65, Table 3), making it difficult to predict the performance of the models for other materials outside this narrow range.

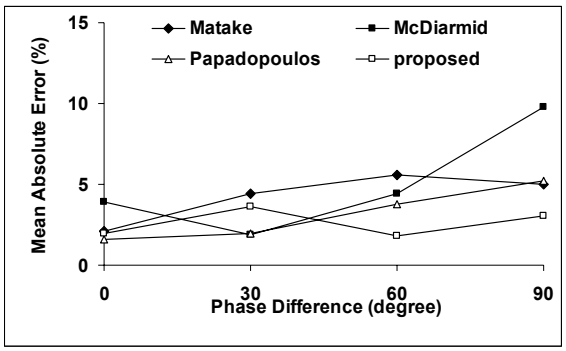

a) Hard Steel

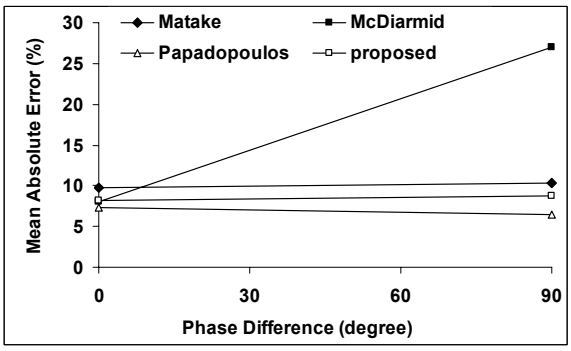

b) 42CrMo4

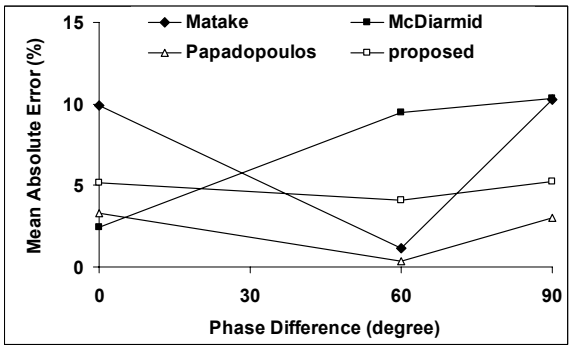

c) 34Cr4

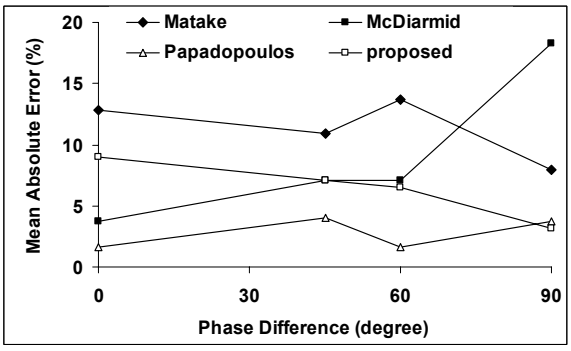

d) 30NCD16

Fig. 2 Mean absolute error comparisons under different phase

Another set of experimental data (Carpinteri and Spagnoli, 2001) is used to test the model's performance for different materials. The material properties are listed in Table 4. It should be noted that the experimental work for Hard Steel in Table 3 is exactly same as that for Hard Steel in Table 4. This was originally done by Nishihara and Kawamoto (1945). Different other fatigue limit data have been reported by several authors. Papadopoulos (1997) uses the data reported by McDiarmid (1987). Carpinteri and Spagnoli (2001) use the data reported by Macha (1989). In order to diminish the data estimation error introduced by different authors, both data sets are used here.

Table 4. Material properties employed by Carpinteri (2001)

Material	f_{-1} (Mpa)	t_{-1} (Mpa)	t_{-1} / f_{-1}	σ_u (Mpa)
Hard Steel	313.9	196.2	0.63	704.1
Mild Steel	235.4	137.3	0.58	518.8
Cast Iron	96.1	91.2	0.95	230.0

The fatigue fracture plane orientation is reported by Macha (1989). The comparisons of the fatigue fracture orientations between experimental observations and present model predictions are listed together in Table 5. The present model predictions of the fatigue fracture orientation agree with the experimental observations very well. Although not listed in this chapter, both McDiarmid's model and Carpinteri's model gave almost the same predictions as the current model.

The comparisons of the fatigue limits for different models are plotted in Fig. 3. Since Matake's model fails to determine the critical plane under some loading cases (Carpinteri and Spagnoli, 2001), Carpinteri and Spagnoli's model is used in the current comparison.

Table 5. Comparisons of fatigue fracture orientations

Hard Steel			Mild Steel			Cast Iron		
Test No	$\theta_{\exp}(^o)$	$\theta_{cal}(^o)$	Test No	$\theta_{\exp}(^o)$	$\theta_{cal}(^o)$	Test No	$\theta_{\exp}(^o)$	$\theta_{cal}(^o)$
1	0	0	1	0	0	1	0	0
2	12	11	2	12	11	2	12	11
3	22	22	3	22	22	3	25	22
4	34	34	4	30	34	4	34	34
5	45	45	5	45	45	5	49	45
6	16	22	6	12	18	6	0	0
7	32	34	7	8	35	7	0	0
8	8	18	8	0	0	8	37	39
9	22	35	9	8	0			
10	0	0	10	39	39			
11	0	0						
12	28	39						

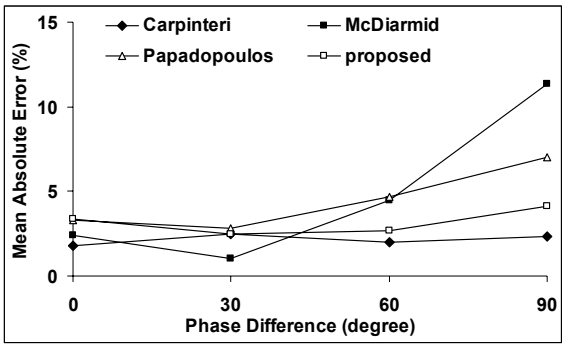

a) Hard Steel

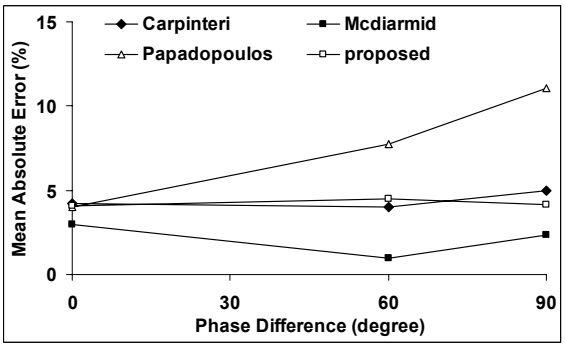

b) Mild Steel

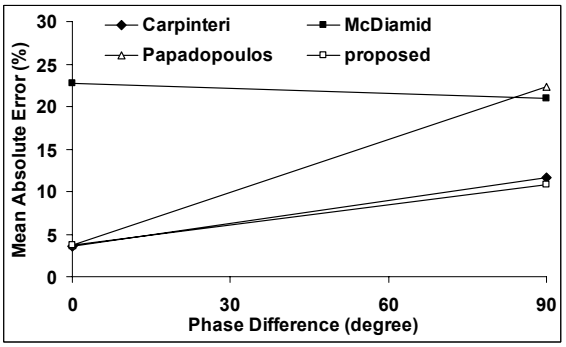

c) Cast Iron

Fig. 3 Mean absolute error comparisons under different phase differences

From Fig. 3, both Carpinteri's model and the present model give an overall small error. McDiarmid's model gives a poor estimation for cast iron. Papadopoulos' model seems to have an increased error as the phase difference increases, especially for cast iron. It is interested to find that Carpinteri's model and the present model gave very close predictions for all the material and loading conditions. For the experimental data used by Carpinteri and Spagnoli (2001), mean stress is zero and t_{-1}/f_{-1} is less than one. Their criterion (Eq. (22)) is rewritten as

$$\begin{cases} \alpha = 45\dfrac{3}{2}[1-(\dfrac{t_{-1}}{f_{-1}})^2] \\ \sqrt{(\dfrac{\sigma_{a,c}}{f_{-1}})^2+(\dfrac{\tau_{a,c}}{t_{-1}})^2} = \beta = 1 \end{cases} \tag{43}$$

The present model (Eq. 37) can be rewritten as

$$\begin{cases} cos(2\alpha) = \dfrac{-2+\sqrt{4-4(1/s^2-3)(5-1/s^2-4s^2)}}{2(5-1/s^2-4s^2)} \\ \sqrt{(\dfrac{\sigma_{a,c}}{f_{-1}})^2+(\dfrac{\tau_{a,c}}{t_{-1}})^2} = \beta \end{cases} \tag{44}$$

Since the fatigue fracture planes predicted by the two models are almost the same, the only differences between the two criteria are the material parameters α and β. Their values are plotted in Fig. 4. As shown in Fig. 4, it is found that the two sets values of the material parameters α and β are close for hard metals ($1/\sqrt{3} < t_{-1}/f_{-1} < 1$), especially for the materials used by Carpinteri and Spagnoli (2001). Thus the two models give very close results in this case. However, Carpinteri and Spagnoli's model is empirical and cannot be applied to extreme brittle metals ($t_{-1}/f_{-1} > 1$) and ductile

metals ($t_{-1}/f_{-1} < 1/\sqrt{3}$), because the critical plane is not defined in those range by Carpinteri.

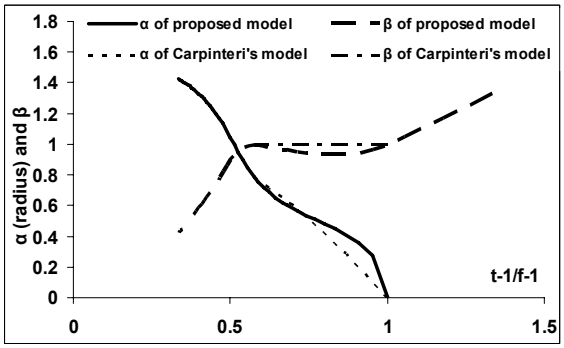

Fig. 4 Comparison of the material parameters for present model and Carpinteri's model

Four sets of fatigue experimental data are employed to validate the fatigue life prediction model. They are SAE-1045-1 steel reported by Kurath et al (1989), SAE-1045-2 steel reported by Fatemi and Stephens (1989), SM45C steel reported by Lee (1989), 5% chrome work roll steel reported by Kim et al (2004). Some material axial and torsion fatigue properties are listed in Table 6.

Notice that the proposed model has no special requirement of the S-N curve format. Different formats can be used for best regression results. The R^2 values are also listed in Table 6. The four materials cover a wide range of steel, from extremely brittle steel to ductile steel (t_{-1}/f_{-1} ranges from 0.57 to 1.28). The comparisons of the present model predictions and experimental observations are plotted together in Fig. 5. Two bounds are also plotted. The inner bound is according to the life factor of 2. The outer bound is according to the life factor of 3.

Table 6. Material fatigue properties of four different steels

Material	Fully Reversed S-N Curve		R^2	Fatigue Limits (Mpa)	$\frac{t_{-1}}{f_{-1}}$
SAE-1045-1	Axi.	$\sigma_a = 1261.8(Log(N))^{-0.9315}$	0.98	237.76	0.61
	Tor.	$\sigma_a = 603.33(Log(N))^{-0.8303}$	0.98	136.29	
SAE-1045-2	Axi.	$\sigma_a = 1248.7(Log(N))^{-0.9157}$	0.99	242.05	0.57
	Tor.	$\sigma_a = 558.84(Log(N))^{-0.7402}$	0.98	148.35	
SM45C	Axi.	$\sigma_a = 445.75 + \frac{378.25}{1+(\frac{Log(N)}{4.23})^{8.25}}$	0.99	445.75	0.71
	Tor.	$\sigma_a = 317.12 + \frac{158.63}{1+(\frac{Log(N)}{4.60})^{9.30}}$	0.99	317.12	
5% chrome work roll steel	Axi.	$\sigma_a = -125.46Log(N) + 1256.8$	0.99	504.04	1.28
	Tor.	$\sigma_a = -145.3Log(N) + 1515.8$	0.91	644.00	

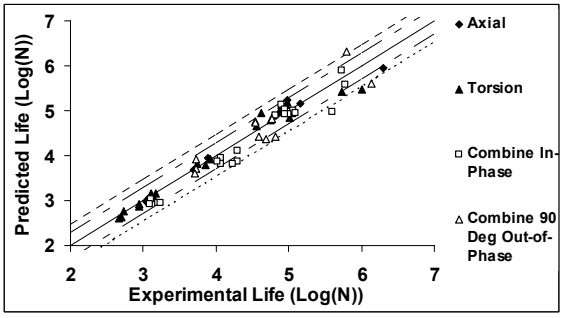

a) SAE-1045-1

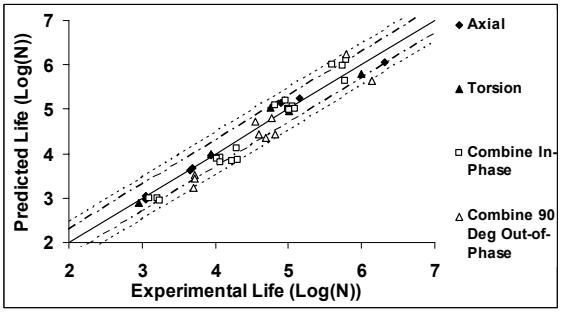

b) SAE-1045-2

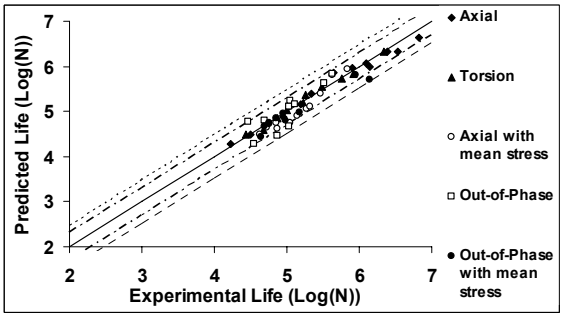

c) SM45C

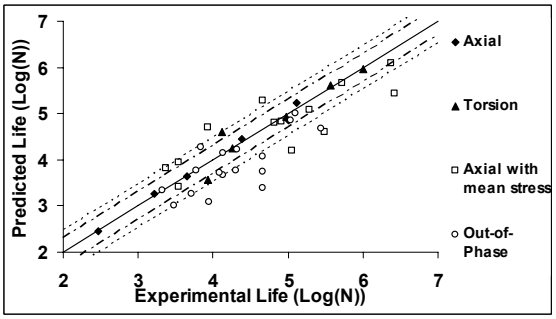

d) 5% chrome work roll steel

Fig. 5 Comparisons of life predictions and experimental observations

From Fig. 5, it is seen that the proposed model agrees with the experimental observations very well. 78% of the total points fall into the range of life factor 2 and 92% of the total points fall into the range of life factor 3. There are no systemic errors for the loading conditions, material properties and mean stress effect in the present model. The error index is defined as the relative difference from the experimental observations. The histogram of the error index considering all the experimental specimens is plotted in Fig. 6.

The worst case of the proposed model's life prediction is for 5% chrome work roll steel. As mentioned by Kim et al (2004), there is more scatter in life data for this material than usually observed in the laboratory for ductile metals. This is believed to be an inherent characteristic of materials whose life is controlled by defects (Hanlon et al, 1997; Nadot et al, 1999). Despite the larger scatter, the proposed model predicts the trend very well. The fatigue fracture plane orientations are also reported by Kim et al (2004). The present model predictions and experimental observations are listed in Table 7.

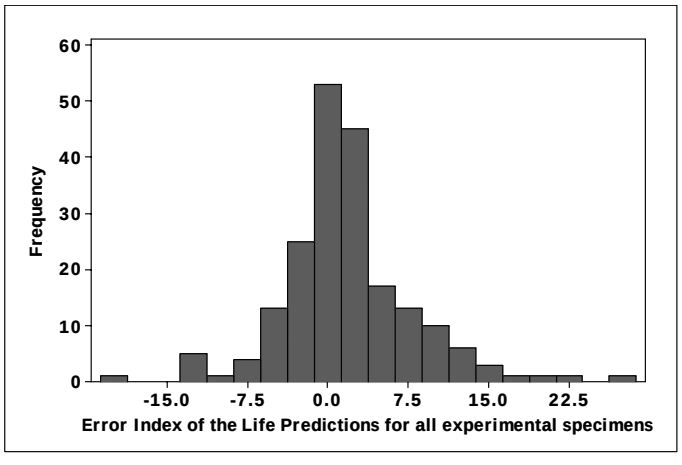

Fig. 6 Histogram of the error index of fatigue life (log scale)

Table 7. Comparisons of fatigue fracture orientations between experimental observations and model predictions for 5% chrome work roll steel

Test No	$\theta_{\exp}(^o)$	$\theta_{cal}(^o)$	Test No	$\theta_{\exp}(^o)$	$\theta_{cal}(^o)$
1	25	24	11	10	17
2	10	21	12	170	163
3	172	173	13	39	32
4	31	32	14	32	34
5	25	33	15	35	34
6	143	146	16	40	38
7	41	37	17	31	34
8	40	38	Uniaxial	0	0
9	135	139	Torsion	45	45
10	21	24			

2.3 Strain-based low cycle multiaxial fatigue crack initiation

For low-cycle multiaxial fatigue problems, strain-based or energy-based models are commonly used. Similar to high-cycle multiaxial fatigue problems, the effectiveness of individual methods varies with material, fracture mechanism and loading conditions (Kim et al, 1999). No single theory has been applied to a wide variety of materials and loading conditions (Socie, 1987). To the authors' knowledge, no existing multiaxial fatigue damage model is universally accepted. This paper focused on the strain-based models and thus only those models are briefly described below.

2.3.1 Existing low-cycle fatigue models

Early investigations used the equivalent strain approach (Pascoe and Devilliers, 1967) and plastic work or plastic strain energy approach (Garud, 1979, Ellyin and Valarie, 1982). In recent years, fatigue models based on the critical plane approach for multiaxial fatigue evaluation have been gaining popularity due to their success in accurately predicting lives (Socie, 1989; You and Lee, 1996). A number of the critical plane

approaches that are based on strain or energy, are for the shear failure mode (Brown and Miller, 1973; Kandil et al, 1982; Lohr and Ellison, 1980; Socie et al, 1989; Fatemi and Socie, 1988; Farahani, 2000; Pan, 1999). Some other models are based on tensile failure mode (Smith et al, 1970; Socie, 1987; Chu et al, 1993; Kim et al, 2004). It has been found that the methods based on one failure mode perform poorly for the fatigue modeling of the other failure mode (Socie, 1987; Farahani, 2000; Kim et al, 2004). Bannantine and Socie (1991) suggest using two different models for different failure modes and choosing the better prediction as the final result. Similar methodologies are used by other researchers (Chen et al, 1999; Liu and Wang, 2001). Park and Nelson (2000) reviewed the two-model methodology suggested by Socie (1987) and stated that the failure modes depend on the materials. It appears that the failure mode depends not only on the material properties but also on the stress state (Socie, 1987; Lee et al, 2003). Lee et al (2003) found that STS304 shows different failure modes in low-cycle regime and high-cycle regime. This type of observations make the two-model approach some what difficult to apply because no information is available for choosing the model before the failure modes are observed. Sometimes, the crack information is not available as it may be not possible due to the nature of the loadings or equipments (Kim et al ,1999; Kallmeyer et al, 2002).

The critical plane approach was originally proposed based on the observations that the fatigue crack nucleation occurs at the persistent slip bands, formed in some grains (crystals) of the materials. The planes are named critical plane and the stress (strain) components on it are used for fatigue analysis (Papadopoulos, 1997). That is the physical basement of the critical plane approach. This assumption or basement makes it difficult to

apply the model to the material with different microstructures as normally used metals. Also, this assumption usually requires cracking analysis to distinguish the failure modes before you apply the appropriate critical-plane based model (Fatemi and Socie, 1988). If both failure modes occur and neither of them dominates in the experiments, the decision of choosing the appropriate model is hard to make.

In this section, a new fatigue damage model based on the characteristic approach is proposed. The characteristic plane approach is similar with the critical plane in the calculation procedure. A plane is first determined and the strain components on the plane are combined together and used for fatigue life prediction. Unlike most of existing critical plane-based models, the characteristic plane in the proposed model is not based on the physical observations of the crack but arises from the idea of dimension reduction. It assumes the complex multiaxial fatigue problem can be approximated by using the strain components on a certain plane (named characteristic plane in this paper). Then the objectives are to find the plane and the formula of combinations of the strain components on that plane. Through this type of definition of the characteristic plane, failure mode analysis is not required and the proposed model can automatically adapt for different materials. Also, this definition makes the proposed model have the potential to apply to the materials with non-metal microstructures. The correction factors for the extra out-of phase plastic hardening and mean stress are also introduced to the proposed model. A wide range of experimental observations for metals available in the literature are used to validate the proposed model. Very good correlations are found between predicted and experimental fatigue lives under proportional and nonproportional loading for both low-cycle and high-cycle regimes.

2.3.2 Proposed new multiaxial fatigue model

Multiaxial fatigue problem is complex because it usually involves 3D stress (strain) histories. To directly analysis the multiaxial fatigue problem is either cumbersome or unpractical, as it may require too much computational and experimental effort. Moreover, when the applied multiaxial loadings are non-proportional, the determination of the stress (or strain) amplitudes becomes difficult (Papadopoulos et al, 1997). In this work, we are trying to reduce the dimension of the problem and approximate the complex 3D fatigue problem by using the strain components on a certain plane, which reduce the dimension of the problem and simplified the calculation. This plane is named characteristic plane in the proposed model.

In the proposed model, we make an assumption that there exists a characteristic plane, on which the strain components or their combinations can be used to approximate the complex multiaxial fatigue problem. Following this assumption, the two objectives of this paper become clear. One objective is to find the characteristic plane for different materials. The other is to find the formula for the combination of those strain components acting on the plane.

Before we process to the detailed derivation of the proposed method, a short discussion is given here to distinguish the difference between the characteristic plane-based model and the critical plane-based model. These two methods differed in three main aspects as described below.

Their physical bases are different. As described in the previous section, the critical plane approach originates from the observations of the fatigue crack, which is usually either the maximum normal stress (strain) plane (Mode I) or the maximum shear

stress (strain) plane (Mode II or III). The characteristic plane approach originates from the dimension reduction idea, in which the main objective is to reduce the complexity of the multiaxial fatigue problem. The resulting characteristic plane is only a material plane, on which the fatigue damage is evaluated. It may or may not have a direct relation with the fatigue crack orientation observed in the experiments. The physical difference makes the characteristic plane approach not require failure modes analysis before application to multiaxial fatigue damage calculation, which is usually required by the critical plane-based models. Also, the characteristic plane approach has the potential to apply to the non-metals, in which the non-crystal like microstructure violates the physical basis of the critical plane approach.

The identification procedures of the characteristic plane and the critical plane are different. Once the material failure mode is observed, the identification of the critical plane is straightforward. It only relies on stress (or strain) analysis. For different materials with the same failure mode, the critical plane orientation is fixed. It is either the maximum normal stress (or strain) plane or the maximum shear stress (or strain) plane. The characteristic plane in the proposed model is determined through minimizing the contributions of the hydrostatic strain amplitude to zero. It explicitly relies both on the material properties and strain analysis. For different materials with the same failure mode, the characteristic plane could be different since it is depends on both the uniaxial and pure torsional e-N curves. From this point of view, the determination of the critical plane is semi-analytical because it requires that the analyst determine the failure modes first from experimental data or assumes from experience. The characteristic plane

determination is fully analytical since it only requires the quantitative data from uniaxial and torsional experiments.

The results and robustness of the characteristic plane approach and the critical plane approach are different. The result of the critical plane is a discrete function, which is either maximum normal strain plane or maximum shear strain plane. The result of the characteristic plane is a quantitative and continuous function. In the multiaxial fatigue experiments, usually both Mode I and Mode II cracks exist. For example, under pure shear tests, the crack usually occurs along the maximum shear strain plane then propagates along the maximum principle stress plane. In that case, only visual or empirical observation is not good enough to decide which model to use. Also, if you make a decision based on a certain parameter exceeding a threshold value (e.g. Life of Mode II crack exceeds 70% of the total life), there is still a problem because you create a discontinuity subjectively. The material with 69% uses the critical plane of maximum normal strain amplitude and the material with 71% uses the critical plane which is 45 degree off the maximum normal strain amplitude plane. Therefore, a quantitative and continuously varying model is more desirable. For the material changing failure modes with respect to loadings and environmental conditions or the material with out failure mode information, it is risky to apply either of those models, because their error is unpredictable. From this point of view, the proposed model is more robust since it can automatically adapt to those conditions.

A new damage parameter defined on the characteristic plane is proposed. Consider the fully reversed uniaxial-torsional fatigue problem (with no mean stress). The strain tensors under plane stress condition are given in Eq. (45):

$$\begin{bmatrix} \varepsilon_a & \frac{\gamma_a}{2} & 0 \\ \frac{\gamma_a}{2} & -v_{eff}\varepsilon_a & 0 \\ 0 & 0 & -v_{eff}\varepsilon_a \end{bmatrix} \quad (45)$$

where ε_a and γ_a are the normal and shear strain amplitude (half of the strain range), respectively. v_{eff} is the effective Poisson's ratio which is given by:

$$v_{eff} = \frac{v_e \varepsilon_{ae} + v_p \varepsilon_{ap}}{\varepsilon_a} \quad (46)$$

where v_e is the elastic Poisson's ratio. If no experimental value is available, a value of 0.3 can be used instead. v_p is the plastic Poisson's ratio and takes the value of 0.5. ε_{ae} and ε_{ap} are the elastic and plastic strain amplitude, respectively. They can be calculated from a cyclic stress-strain relationship, such as the Ramberg-Osgood equation:

$$\varepsilon_a = \varepsilon_{ae} + \varepsilon_{ap} = \frac{\sigma_a}{E} + \left(\frac{\sigma_a}{K'}\right)^{\frac{1}{n'}} \quad (47)$$

where E is the Young's modulus. K' and n' are the cyclic strength coefficient and the cyclic strength exponent, respectively.

To simplify the discussion, we first investigate the fatigue failure criteria at the fatigue limit stage. As stated in the previous section, one objective in the proposed method is to find an appropriate formula to combine the strain components for fatigue damage evaluation. It is obvious that both shear stress (or strain) and normal stress (or strain) contribute to the final failure of mechanical components under multiaxial fatigue loading. However, several researchers have also noticed the importance of hydrostatic stress and included its effect in their models (Papadopoulos, 1997). It was also shown that

the contribution of hydrostatic stress is different for different models and seems to vary with materials. The proposed model includes damage contribution from three sources - the normal strain ($\varepsilon_{a,c}$), shear strain acting ($\gamma_{a,c}$) on the characteristic plane and hydrostatic strain amplitude ($\varepsilon_{a,c}^{H}$). It assumes that the material fails when the summation of the normalized energies due to the three strain components reaches a critical value. A mathematical expression is formulated as

$$\frac{\varepsilon_{a,c}\sigma_{a,c}}{\varepsilon_{-1}\sigma_{-1}}+\frac{\gamma_{a,c}\tau_{a,c}}{\gamma_{-1}\tau_{-1}}+A\frac{\varepsilon_{a}^{H}\sigma_{a}^{H}}{\varepsilon_{-1}\sigma_{-1}}=B \qquad (48)$$

where $\sigma_{a,c}, \tau_{a,c}$ and $\sigma_{a,c}^{H}$ are the normal stress amplitude, shear stress amplitude acting on the characteristic plane, and hydrostatic stress amplitude, respectively. ε_{-1} and γ_{-1} are uniaxial and torsional fatigue strain limits, respectively. σ_{-1} and τ_{-1} are uniaxial and torsional fatigue stress limits, respectively. A and B are material parameters which are determined from uniaxial and torsional fatigue tests.

The physical meaning of Eq. (48) is that the final damage is the summation of the damage caused by different energy components. Parameter A is a materials parameter and considers the different contributions of the hydrostatic strain amplitude corresponding to different materials. Under the fatigue limit state, the material is usually elastic. In that case Eq. (48) can be simplified only using strain terms.

$$\sqrt{(\frac{\varepsilon_{a,c}}{\varepsilon_{-1}})^{2}+(\frac{\gamma_{a,c}}{\gamma_{-1}})^{2}+k(\frac{\varepsilon_{a}^{H}}{\varepsilon_{-1}})^{2}}=\beta \qquad (49)$$

where k and β are material parameters which can be determined by uniaxial and torsional fatigue tests. The strain-based version is easy to calculate compared with the model directly using energy terms. Also, the fatigue properties expressed in e-N curves

are in common use already. This makes it easy to implement the proposed method to practical applications.

Since the orientation of the characteristic plane has not been determined yet, suppose that for one type of material the characteristic plane coincides with the maximum normal strain amplitude plane. In this case, the characteristic plane is similar with the critical plane definition of tensile failure mode.

For a fully reversed uniaxial fatigue experiment $(\varepsilon_a = \varepsilon_{-1}, \gamma_a = 0)$, the strain components on the characteristic plane are:

$$\begin{cases} \varepsilon_{a,c} = \varepsilon_{-1} \\ \gamma_{a,c} = 0 \\ \varepsilon_a^H = \varepsilon_{-1}(1 - 2v_{eff})/3 \end{cases} \tag{50}$$

For a fully reversed pure torsional fatigue experiment $(\varepsilon_a = 0, \gamma_a = \gamma_{-1})$, the strain components on the characteristic plane are:

$$\begin{cases} \varepsilon_{a,c} = \gamma_{-1}/2 \\ \gamma_{a,c} = 0 \\ \varepsilon_a^H = 0 \end{cases} \tag{51}$$

Substitute Eq. (50) and (51) to Eq. (49) and solve for material parameters, we obtain:

$$\begin{cases} \beta = \dfrac{1}{2}\dfrac{\gamma_{-1}}{\varepsilon_{-1}} \\ k = \left[\dfrac{1}{4}\left(\dfrac{\gamma_{-1}}{\varepsilon_{-1}}\right)^2 - 1\right]\dfrac{9}{(1 - 2v_{eff})^2} \end{cases} \tag{52}$$

Notice that the physical meaning of k is the contribution of damage caused by the hydrostatic strain amplitude. It should be non-negative. So $\gamma_{-1}/\varepsilon_{-1}$ should not be less

than two. Recall the assumption made before this calculation. It is only possible for a material ($\gamma_{-1} / \varepsilon_{-1} \geq 2$) that the characteristic plane coincides with the maximum normal strain plane using the present damage parameter (Eq. (49)). It is also interesting to notice that k equals zero when $\gamma_{-1} / \varepsilon_{-1} = 2$, which means (from Eq. (49)) that the hydrostatic strain amplitude has no contribution to the fatigue damage for this material according to the present definition of the damage parameter (Eq. (49)).

Now suppose that for one type of material, the characteristic plane is 45 degrees off the maximum normal strain amplitude plane, which is the maximum shear strain amplitude plane for uniaxial and torsional loading. In this case, the characteristic plane is similar with the critical plane of shear failure mode. Following the steps described above, the material parameters k and β are once again calculated.

For a fully reversed uniaxial fatigue experiment $(\varepsilon_a = \varepsilon_{-1}, \gamma_a = 0)$, the strain components on the characteristic plane are

$$\begin{cases} \varepsilon_{a,c} = \varepsilon_{-1}(1 + v_{eff})/2 \\ \gamma_{a,c} = \varepsilon_{-1}(1 + v_{eff})/2 \\ \varepsilon_a^H = \varepsilon_{-1}(1 - 2v_{eff})/3 \end{cases} \quad (53)$$

For a fully reversed pure torsional fatigue experiment $(\varepsilon_a = 0, \gamma_a = \gamma_{-1})$, the strain components on the characteristic plane are

$$\begin{cases} \varepsilon_{a,c} = 0 \\ \gamma_{a,c} = \gamma_{-1} \\ \varepsilon_a^H = 0 \end{cases} \quad (54)$$

Substituting Eqs. (53) and (54) in Eq. (49) and solving for the material parameters:

$$\begin{cases} \beta = 1 \\ k = [\,1 - \dfrac{1}{4}\left(1 - v_{eff}\right)^2 - \left(1 + v_{eff}\right)^2 \left(\dfrac{\gamma_{-1}}{\varepsilon_{-1}}\right)^2] \dfrac{9}{(1 - 2v_{eff})^2} \end{cases} \quad (55)$$

From Eq. (55), $\gamma_{-1} / \varepsilon_{-1}$ should not be less than $2\sqrt{\dfrac{\left(1 + v_{eff}\right)^2}{4 - \left(1 - v_{eff}\right)^2}}$. The mechanical component is usually kept in elastic condition near the fatigue limit regime, thus v_{eff} can be approximated using 0.3. Under this assumption, $\gamma_{-1} / \varepsilon_{-1}$ should not be less than 1.39. Thus, it is only possible for a certain type of material ($\gamma_{-1} / \varepsilon_{-1} \geq 2\sqrt{\dfrac{\left(1 + v_{eff}\right)^2}{4 - \left(1 - v_{eff}\right)^2}}$) that the characteristic plane could be the maximum shear strain amplitude plane using the present damage parameter (Eq. (49)). Similar to the first case, k equals zero when $\gamma_{-1} / \varepsilon_{-1} = 2\sqrt{\dfrac{\left(1 + v_{eff}\right)^2}{4 - \left(1 - v_{eff}\right)^2}}$, which means (From Eq. (49)) that the hydrostatic strain amplitude ε_a^H has no contribution to the fatigue damage for this material according to the present definition of the damage parameter.

Several conclusions can be drawn based on the derivations of the characteristic plane orientations for the two cases above. The contribution of the hydrostatic strain amplitude is different for different materials if the characteristic plane is fixed for all the materials. There are two special types of material ($\gamma_{-1} / \varepsilon_{-1} = 2$ and $\gamma_{-1} / \varepsilon_{-1} = 2\sqrt{\dfrac{\left(1 + v_{eff}\right)^2}{4 - \left(1 - v_{eff}\right)^2}}$), for which the contribution of the hydrostatic strain amplitude is zero if the characteristic plane is defined as either the maximum normal strain plane or maximum shear strain plane.

Instead of fixing the characteristic plane, the current model searches for the characteristic plane orientations on which the contribution of the hydrostatic strain amplitude is minimized to zero. This is the general approach that can be applied to all materials.

For an arbitrary material, let the angle between the characteristic plane and the maximum normal strain amplitude plane be α. Since the contribution of the hydrostatic strain amplitude is zero, Eq. (49) is rewritten as:

$$\sqrt{(\frac{\varepsilon_{a,c}}{\varepsilon_{-1}})^2+(\frac{\gamma_{a,c}}{\gamma_{-1}})^2}=\beta \tag{56}$$

The objective is to find α and β for an arbitrary material, following the steps described for the first two cases.

For a fully reversed uniaxial fatigue experiment $(\varepsilon_a=\varepsilon_{-1},\gamma_a=0)$, the strain components on the characteristic plane are given as:

$$\begin{cases}\varepsilon_{a,c}=\dfrac{(1-v_{eff})}{2}\varepsilon_{-1}+\dfrac{(1+v_{eff})}{2}\varepsilon_{-1}\cos(2\alpha)\\ \gamma_{a,c}=(1+v_{eff})\varepsilon_{-1}\sin(2\alpha)\end{cases} \tag{57}$$

For a fully reversed pure torsional fatigue experiment $(\varepsilon_a=0,\gamma_a=\gamma_{-1})$, the strain components on the characteristic plane are given as:

$$\begin{cases}\varepsilon_{a,c}=\dfrac{\gamma_{-1}}{2}\cos(2\alpha)\\ \gamma_{a,c}=\gamma_{-1}\sin(2\alpha)\end{cases} \tag{58}$$

Substituting Eqs. (57) and (58) in Eq. (56) and solving for α and β,

$$\begin{cases} \beta = [\frac{1}{4}\cos^2(2\alpha)s^2 + \sin^2(2\alpha)]^{\frac{1}{2}} \\ \cos(2\alpha) = \dfrac{-B + \sqrt{B^2 - 4AC}}{2A} \\ A = [(1+v_{eff})^2 + 4 - s^2 - \dfrac{4(1+v_{eff})^2}{s^2}] \\ B = 2(1-v_{eff}^2) \\ C = [(1-v_{eff})^2 + \dfrac{4(1+v_{eff})^2}{s^2} - 4] \end{cases} \quad (59)$$

where $s = \frac{\gamma_{-1}}{\varepsilon_{-1}}$ is a material constant. Here α takes values from 0 to $\frac{\pi}{2}$. As shown in Eq. (59), both α and β are the functions of the material property s and the effective Poisson's ratio v_{eff}. It is found that α increases as s decreases. α equals 0 when s equals 2, and α equals $\frac{\pi}{4}$ when s equals $2\sqrt{\frac{(1+v_{eff})^2}{4-(1-v_{eff})^2}}$. β does not change monotonically with respect to s, but all the β values are close to 1 for materials with $2\sqrt{\frac{(1+v_{eff})^2}{4-(1-v_{eff})^2}} < s < 2$. The variations of α and β with respect to s are plotted in Fig. 7 with two different Poisson's ratios. One is for pure elastic condition and takes the value of 0.3. The other is for pure plastic condition and takes the value of 0.5. Notice that the physical meaning of α is an indication of material failure mode. When α is close to 0 degree, it indicates the tensile failure mode. When α close to 45 degree, it indicates the shear failure mode. As shown in Fig. 7, the value of α also depends on the effective Poisson's ratio. It appears that, for the material with constant value of s, shear failure mode is likely to occur under low-cycle regime (larger plastic deformation).

From Eq. (59), α has no real solution for $s > 2$. This indicates that for those materials, such as 5% chrome work roll steel (Kim et al, 2005), the contribution of hydrostatic strain amplitude cannot be minimized to zero and must be considered during the fatigue damage evaluation. We use the results of which the characteristic plane is defined on the maximum normal strain plane for the materials of $s > 2$. The summary of material parameters for all types of materials are listed in Table 8.

Table 8. Material parameters for fatigue damage evaluation

Material parameters	$s = \frac{\gamma_{-1}}{\varepsilon_{-1}} \le 2$	$s = \frac{\gamma_{-1}}{\varepsilon_{-1}} > 2$
α	$cos(2\alpha) = \frac{-B + \sqrt{B^2 - 4AC}}{2A}$ $A = [(1+v_{eff})^2 + 4 - s^2 - \frac{4(1+v_{eff})^2}{s^2}]$ $B = 2(1-v_{eff}^2)$ $C = [(1-v_{eff})^2 + \frac{4(1+v_{eff})^2}{s^2} - 4]$	$\alpha = 0$
k	$k = 0$	$k = \left[\frac{1}{4}s^2 - 1\right]\frac{9}{(1-2v_{eff})^2}$
β	$\beta = [\frac{1}{4}cos^2(2\alpha)s^2 + sin^2(2\alpha)]^{\frac{1}{2}}$	$\beta = \frac{1}{2}s$

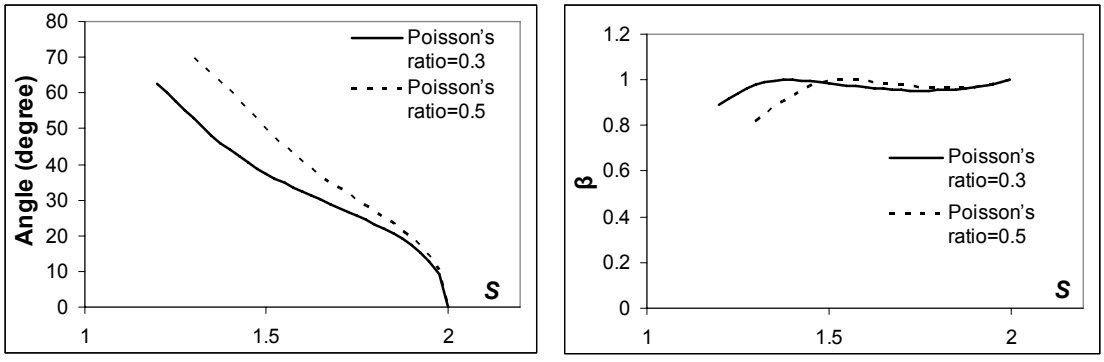

a) α vs. s b) β vs. s

Fig. 7 Variations of α and β at different Poisson's ratios

After developing the fatigue limit criterion as above, the methodology for fatigue life prediction is relatively easy. Notice that the fatigue limit often refers to the fatigue strength at very high cycle (usually 10^6 ~10^7 cycles). For finite fatigue life prediction, the damage parameter should be correlated with the life (number of loading cycles). Eq. (49) can be rewritten as

$$\frac{1}{\beta}\sqrt{(\varepsilon_{a,c})^2+(\frac{\varepsilon_{-1}}{\gamma_{-1}})^2(\gamma_{a,c})^2+k(\varepsilon_a^H)^2}=\varepsilon_{-1} \qquad (60)$$

The left side of Eq. (60) can be treated as the equivalent strain amplitude and can be used to correlate with the fatigue life using the uniaxial e-N curve. Thus the fatigue life model is expressed as:

$$\frac{1}{\beta}\sqrt{(\varepsilon_{a,c})^2+(\frac{\varepsilon_{N_f}}{\gamma_{N_f}})^2(\gamma_{a,c})^2+k(\varepsilon_a^H)^2}=\varepsilon_{N_f}=f\left(N_f\right) \qquad (61)$$

where N_f is the number of cycles to failure and $f\left(N_f\right)$ is the uniaxial strain-life function obtained from experimental results. Notice here ε_{-1} and γ_{-1} in Eq. (61) are replaced by ε_{N_f} and γ_{N_f} respectively, which are fatigue strengths at finite life N_f for uniaxial and torsional loadings. Eq. (61) has no closed form solution. In practical calculation, a trial and error method can be used to find N_f. ε_{N_f} and γ_{N_f} take initial values as ε_{-1} and γ_{-1}. It is found that usually a few iterations are enough to make N_f converge. Eq. (61) together with the parameters in Table 8 are used for fatigue life prediction in this paper. The quantity s in Table 2 is redefined as $s=\frac{\gamma_{N_f}}{\varepsilon_{N_f}}$.

Under out-of phase nonproportional loading, the principal stress and strain direction rotates during one cycle of loading. If plastic deformation occurs, it causes

additional hardening of the material (Socie and Maquis, 2000). Due to the additional hardening, the stress amplitude increases under the same applied strain amplitude for out-of phase loading and thus reduces the fatigue life. A pure strain-based approach does not take into account the additional hardening since there are no stress terms. There are some methodologies to overcome this drawback. Socie (1987) included a stress term on the critical plane to consider the additional hardening caused by out-of phase loading. The energy-based approach (Farahani, 2000) can consider this effect because the stress term is inherent in the energy expression. However, if the stress term is used, plasticity theory is required to predict more accurate elasto-plastic hysteresis loops under nonproportional loading. Although there are some available plasticity models (Mcdowell et al, 1982; Doong and Socie, 1991; Borodii et al, 1996; Shang et al, 2000) for calculating the stress-strain relationship under nonproportional loading, these models usually require extensive numerical computational efforts and many material constants requiring several multi-axial experiments. For the engineering application, a simple correction factor was used to consider the additional hardening (Kanazawa et al, 1979; ASME, 1978; Itoh, 1995; Borodii and Strizhalo, 2000). The general form is given as:

$$\varepsilon_{a,NP} = (1 + \rho F_{NP})\bar{\varepsilon}_a \qquad (62)$$

where $\varepsilon_{a,NP}$ is the equivalent strain quantity considering the nonproportional correction. $\bar{\varepsilon}_a$ is the multiaxial fatigue strain parameter used by different models. F_{NP} is the so called nonproportionality factor and depends on different strain paths. ρ is a material constant which indicates the material sensitivity to the out-of phase loading. Different authors gave different definitions for F_{NP} and ρ. Borodii and Strizhalo (2000) found that, with the same maximum strain amplitude, higher hardening occurs for the strain path

which envelops a larger effective area. This phenomenon is also supported by numerous experimental data (Socie, 1987; Kanazawa, 1979; Kurath et al, 1989; Itoh et al, 1995).

In this paper, a simple definition of F_{NP} is suggested and the value of ρ can be calibrated using one set of out-of phase fatigue tests. First, the strain path is plotted in normalized coordinates, on which the x axis represents the normal strain divided by maximum normal strain amplitude and the y axis represents the shear strain divided by the maximum shear strain amplitude. The nonproportionality factor is defined as the envelope area divided by 4. Several strain paths used in this paper for model validations are plotted in Fig. 8.

In Fig. 8, the uniaxial, torsional and proportional loading paths have no envelope area, thus F_{NP} equals to zero. For box path loading (Fig. 8-(i)), F_{NP} achieves the maximum value of 1. For other strain paths, F_{NP} equals the shaded area divided by the box strain path area (dashed line). In this section, only constant multiaxial loading is considered. For variable multiaxial fatigue loading, suitable modification may be needed. In the comparisons with experimental data, it is shown that the current definition of F_{NP} obtains very good predictions under constant nonproportional multiaxial loading for various metals.

One additional multiaxial data with a specific value of F_{NP} is used to calibrate the material constant ρ using Eq. (62). If the strain amplitude is low and the specimen is under elastic condition, additional hardening does not occur, and thus ρ can take the value of zero. If no experimental data is available, a simple formula is suggested as Eq. (63), which is obtained from the experimental data collected in this work (Table 9). The simplified function and the experimental value are plotted in Fig. 9.

$$\begin{cases} \rho = 0 & \bar{\varepsilon}_a < \dfrac{\sigma_y}{E} \\ \rho = 0.55 + 0.45\cos(\pi(s-1)) & \bar{\varepsilon}_a \geq \dfrac{\sigma_y}{E} \end{cases} \qquad (63)$$

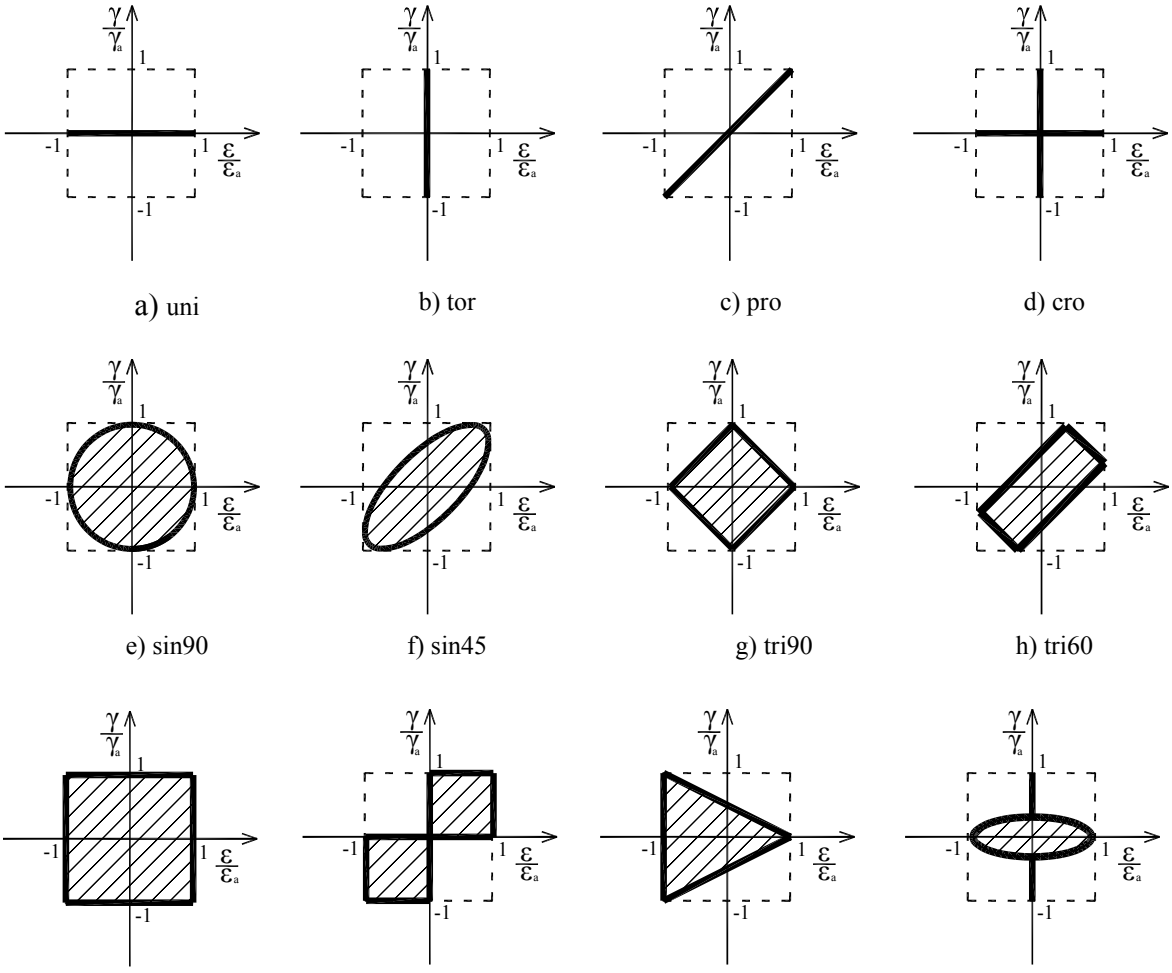

Fig. 8 Different strain paths used in this study

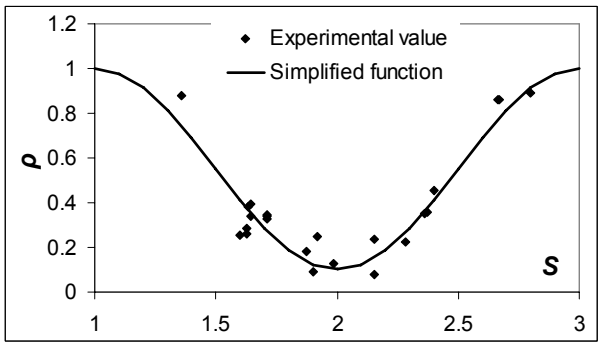

Fig. 9 Variations of ρ vs. s

Practical mechanical components generally experience cyclic fatigue loading together with the mean stress. The mean stress could also be introduced by residual stress, environmental effects, etc. It is well known that the mean normal stress has an important effect on fatigue life. Normally, tensile mean stress reduces the fatigue life, while compressive mean stress increases the fatigue life (Sines, 1961).

There are many models for mean normal stress effect correction. Gerber (1874), Goodman (1899), Soderberg (1939) and Morrow (1968) proposed different correction factors. Kujawski and Ellyin (1995) proposed a unified approach to mean stress correction. For the multiaxial fatigue problem, mean normal stress is included in the model in different ways (Socie and Maquis, 2000) depending on different models. Fatemi and Socie (1988) considered the maximum normal stress acting on the critical plane. Papadopoulos (1997) considered the hydrostatic mean stress. Farahani (2000) used a correction factor based on the mean stress on the critical plane.

Based on the experimental data collected from the literature, the mean stress is introduced to the fatigue model in this paper by a correction factor similar to Soderberg (1939) as $(1-\frac{\sigma_{m,c}}{\sigma_y})$. Thus, Eq. (61) is rewritten as:

$$\frac{\left(1+\rho F_{NP}\right)}{\left(1-\frac{\sigma_{m,c}}{\sigma_y}\right)}\frac{1}{\beta}\sqrt{(\varepsilon_{a,c})^2+(\frac{\varepsilon_{N_f}}{\gamma_{N_f}})^2(\gamma_{a,c})^2+k(\varepsilon_a^H)^2}=f\left(N_f\right) \quad (64)$$

where $\sigma_{m,c}$ is the mean stress on the characteristic plane; σ_y is the yield strength of the material. Comparisons with the available experimental data in the next section show a good correlation using this correction factor. However, for an arbitrary material, the analyst could use different correction factors such as the one suggested by Kujawski and Ellyin (1995) and calibrate the factors using the experimental data.

In proposed model (Eq. (64), k and β are determined from experimental values of ε_{N_f} and γ_{N_f}, which are obtained using uniaxial and torsional e-N curves. F_{NP} is the stain path parameter and not a material parameter, thus does not require calibration using experimental data. ρ is the only fitting constant requiring calibration using one additional non-proportional loading experiment.

As a result of the above derivation, the methodology becomes very simple with the current model. For any arbitrary loading history, the maximum normal strain amplitude plane is identified. This is achieved by enumeration, by changing the angle by 1 degree increment. Then the angle α and material parameters are determined for different materials according to Table 8. The characteristic plane is the plane which has an angle α with the maximum normal strain amplitude plane. Finally the strain components on the characteristic plane are calculated and the fatigue damage is evaluated using Eq. (64). Note that the characteristic plane in the proposed model explicitly depends on both the strain state (maximum normal strain amplitude plane) and on the material properties (angle α).

2.3.3 Comparison with experimental observations

Twelve sets of fatigue experimental data are employed in this section, and are listed in Table 9. It is noted that the purpose of these comparisons is to validate the model's generality to different materials and conditions. The collected data cover materials used in a lot of different industries, such as construction engineering, automotive engineering, and aerospace engineering. They differ in several ways, such failure mechanism (3 shear, 3 tensile, 2 mixed, and 4 unknown), loading path and other unique characteristics (temperature, surface treatments, etc.). Table 9 includes a detailed description of the experimental data collected in this paper, such as material name, reference, multiaxial strain path, failure mode, s range, stain range and other information unique to the experimental data used.

As mentioned in the derivation, the proposed method shows a positive correlation between the ratio s and material failure mechanism. Shear dominated failure is likely to occur for a low value of s and tensile dominated failure is likely to occur for a high value of s. Experimental observations are also found to support this statement. Table 9 includes the failure patterns observed in the experiments and also the s values defined in the proposed model. It shows a positive correlation between the failure mechanisms and the s value. For shear dominated failure (A533B pressure vessel steel, Waspaloy, Al-6061-T6), lower values of s are observed and range from 1.52 to 1.7. For tensile dominated failure (5% chrome work roll steel, 304 stainless steel, 45 steel), higher values of s are observed and range from 2.3 to 3.1. For mixed failure (1Cr-18Ni-9Ti stainless steel, Hastelloy-X at different temperatures), moderate values of s are observed and range

from 1.4 to 2.7. This type of observations indicates the material failure patterns can be related or explained by the s values as suggested by the proposed method.

Table 9. Experimental data used for model validation

Material	Ref	Multiaxial loading path*	Failure mechanism	s range	Strain range (%)	Other
Waspaloy	[48,49]	Sin90	Shear	1.3~1.7	0.5~1.74	Different surface treatments
Al-6061-T6	[50]	Pro	Shear	1.52~1.55	0.5~0.9	
A533B pressure vessel steel	[51]	Pro, sin90	Mixed and shear dominated	1.52~1.57	0.19~1.68	
Hastelloy-X	[52]	Pro, sin90, cro, ball	23°C: shear; 649°C: tensile	23°C: 1.4~1.7;649 °C: 1.7~2.5	0.52~1.15	Different temperatures
1Cr-18Ni-9Ti stainless steel	[53]	Sin90	Mixed and depends on loadings	1.8~2.7	0.2~1.0	Weld and base metal
AISI Type 304 stainless steel	[8]	Pro, sin90, box, box2	Tensile	2.3~2.8	0.2~1.0	
45 steel	[25]	Sin90, pro, box, cro, tri90	Tensile	2.8	0.33~0.6	
5% chrome work roll steel	[23]	Tri-XX	tensile	2.95~3.1	0.28~0.45	
SAE-1045 steel	[39]	Pro, sin90, box	N/A	1.56~1.79	0.15~2	
SM45C steel	[7]	Pro, sin22, sin45, sin90, box	Not performed	1.65~2.5	0.3~2.5	
Ti-6Al-4V alloy	[28]	Pro, sin90, ttr	Not performed	1.7~2.1	0.01~0.3	Mean stress included
Hayness 188	[54,55]	Pro, sin90, tri60, tri90	N/A	2.2~3.1	0.1~1.4	At the temperature of 760°C

*Note: The abbreviations in column 3 are defined and illustrated in Fig. 8.

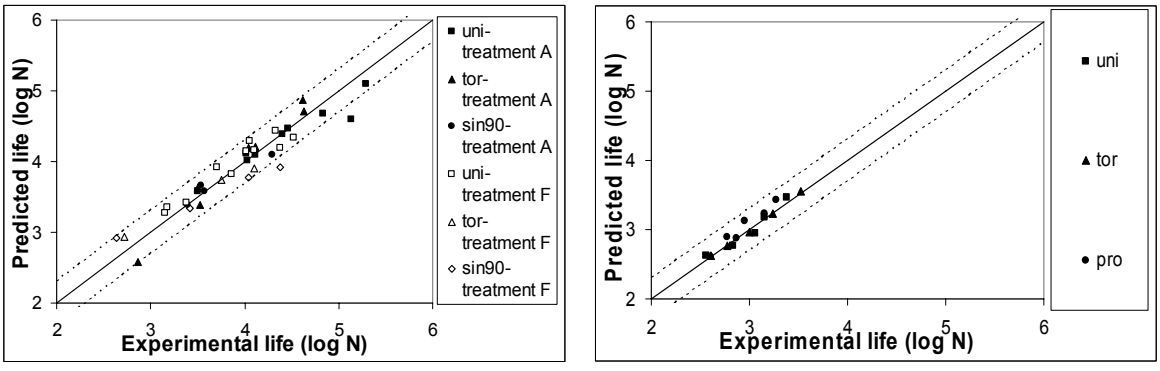

a) Waspalloy b) Al6061

Fig. 10 Comparisons of predicted and experimental fatigue lives

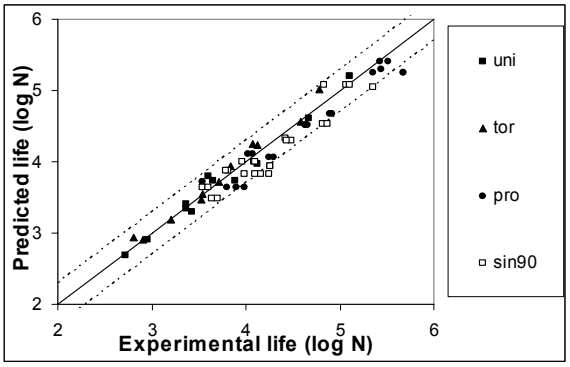

c) A533b steel

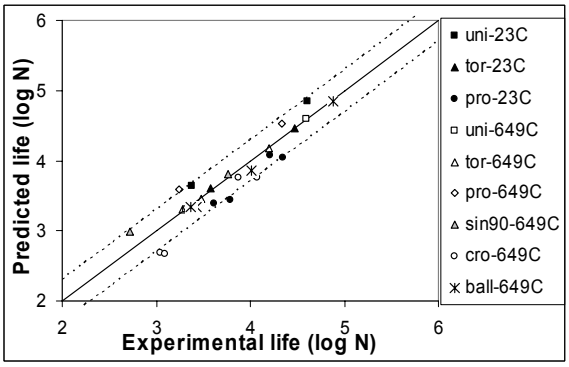

d) Hastelloy-X

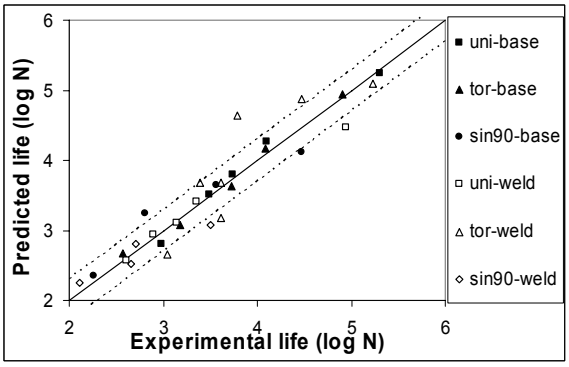

e) 1Cr-18Ni-9Ti steel

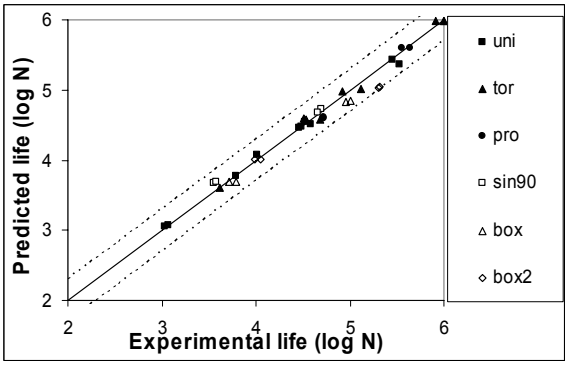

f) 304 stainless steel

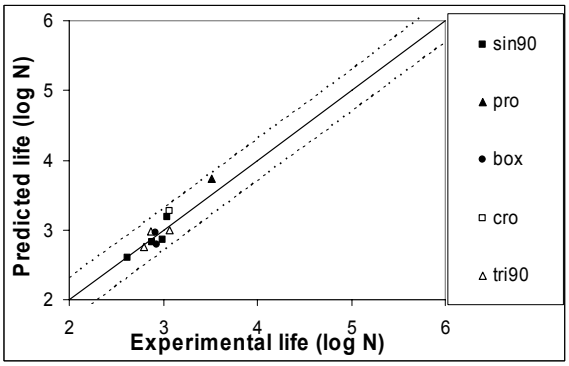

g) 45 steel

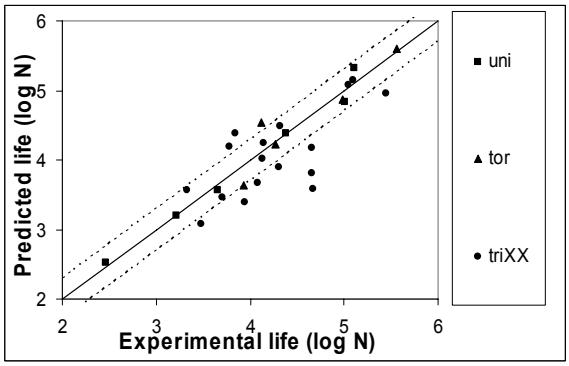

h) 5% chrome work

Fig. 10 Cont.

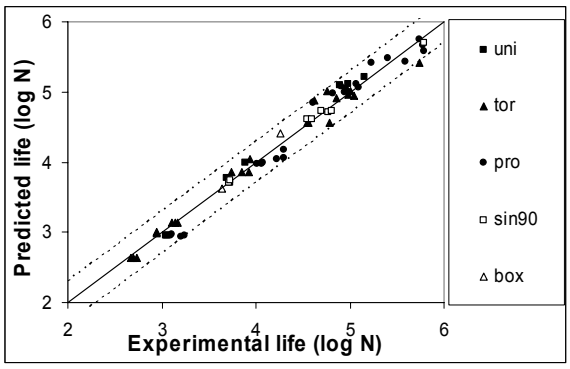

i) SAE 1045 steel

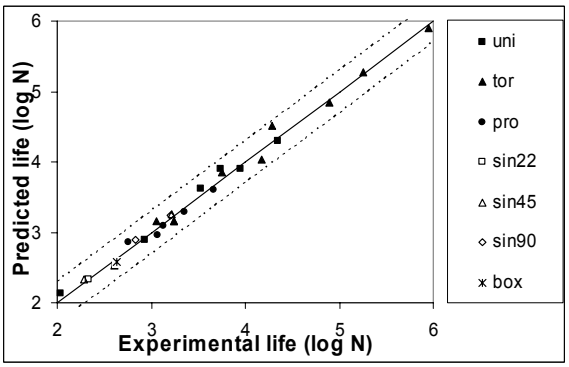

j) S45C steel

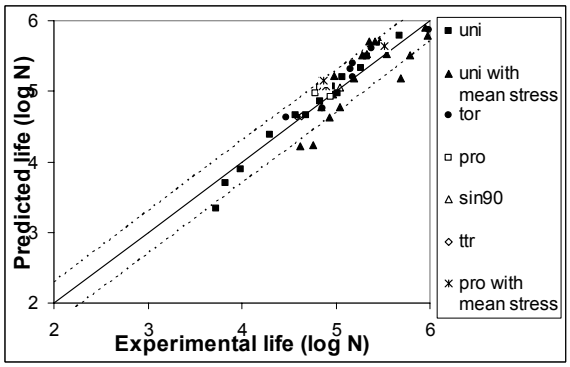

k) Ti-6Al-4V

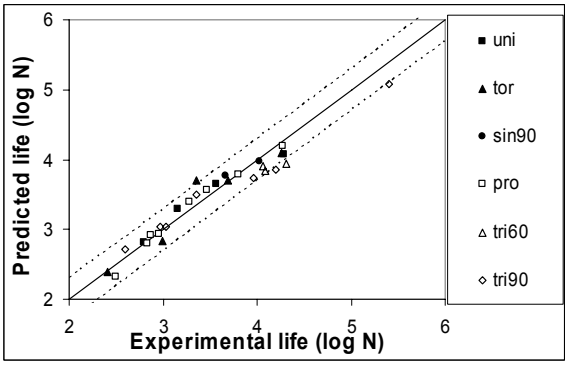

l) Hayness188

Fig. 10 Cont.

The predicted fatigue lives and the experimental lives are plotted together in Fig. 10. In Fig. 10, the x-axis is the experimental life and the y-axis is the predicted life. Both lives are in log scale. The solid line indicates that the predicted results are identical with experimental results. The dashed lines are the life factor of 2. The different strain paths shown in the legend are also shown in Fig. 8.

As shown in the Fig. 10, the predicted results agree with the experimental results very well. Most of the points fall within the life factor of 2. The worst case of the proposed model's life prediction is for 5% chrome work roll steel. As mentioned by Kim

et al (2004), there is more scatter in life data than usually observed in the laboratory for ductile metals. This is believed to be an inherent characteristic of materials whose life is controlled by defects (Hanlon et al, 1997; Nadot et al, 1999). Despite the larger scatter, the proposed model predicts the trend very well.

A statistical comparison is also performed to evaluate the model's performance under different conditions. An error index is defined as:

$$Error = log(\frac{N_{exp}}{N_{pre}}) \qquad (65)$$

where N_{exp} is the experimental life and N_{pre} is the predicted life. When the absolute value of the error index is log(2), it is the inner bounds shown in Fig. 10 and known as the life factor of 2. Four different types of comparisons are used as shown in Fig. 11. The dashed lines in Fig.11 are the life factor of 2. The number of total data points is 429.

The histogram of the error index is shown in Fig. 11(a). From Fig. 11(a), it appears that error is centered near zero, which indicates that the proposed model has no systematic error. Also, 90% of the total data points fall within the life factor of 2 and 98% of the total data points fall within the life factor of 3. The mean absolute error of the predictions for different fatigue life regions is shown in Fig. 11(b). It appears the proposed model has no systematic errors for different fatigue life regions (from low-cycle fatigue to high-cycle fatigue). The mean absolute errors for different loadings are plotted in Fig. 2.11(c). It is shown that the proposed model has no systematic errors to different loadings, such as uniaxial loading, pure torsional loading, multiaxial proportional loading, and multiaxial non-proportional loading. The mean absolute error of the predictions for different values of s is plotted in Fig. 2.11(d). $s = \frac{\gamma_{N_f}}{\varepsilon_{N_f}}$ is an important material property

in the proposed fatigue model and controls the material failure modes. Tensile dominated failure is likely to occur for a large value of s and shear dominated failure are likely to occur for a small value of s. It is shown that the proposed model has no systematic error to different material failure modes. Thus the proposed model has no systematic error due to fatigue regime, loading or failure mode.

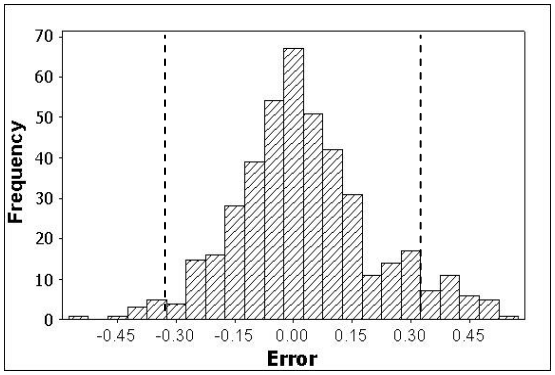

a) Histogram of the prediction errors

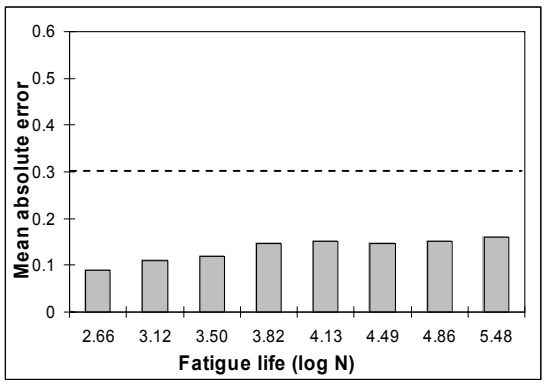

b) Mean absolute error for different life regions

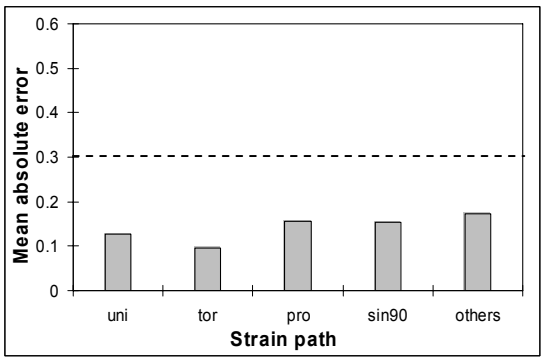

c) Mean absolute error for different strain paths

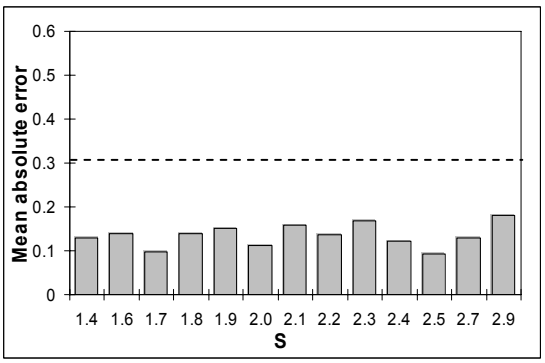

d) Mean absolute error for different s values

Fig. 11 Statistical error evaluation of the proposed method

2.4 Fatigue crack initiation of anisotropic materials

The multiaxial fatigue problem of engineering materials is mainly caused by two reasons. In isotropic materials, the multiaxial stress within the material is due to the complex applied loading history. In anisotropic materials, a multiaxial stress state is obtained even if the applied loading is uniaxial.

Many engineering materials exhibit some degree of anisotropy in mechanical properties, such as rolled metals. Moreover, strongly anisotropic materials such as composite laminates are being used in the industry more popularly in the recent decades. Unlike the extensive progress in multiaxial fatigue analysis of isotropic materials, much further effort is needed to include the anisotropy of the material (Fround 1985; Lin et al 1993; Shokrieh and Lessard, 1997; Diao et al 1999).

In this section, a unified multiaxial fatigue damage model is proposed for both isotropic and anisotropic materials. The proposed model is a characteristic plane-based model, which is developed based on the model in Section 2.2. The derivation for isotropic materials is already described earlier. The model is extended for anisotropic materials. A simple case for orthotropic materials is derived and used for illustration. A wide range of experimental observations available in the literature, including metals, and unidirectional and multidirectional composite laminates, are used to validate the proposed model.

2.4.1 Existing fatigue models for anisotropic materials

Several investigations have been reported for anisotropic composite laminates. Fatigue analysis of composite materials is difficult due to several basic characteristics of the composite material (Fong 1982). However, many attempts have been made for fatigue

modeling and life prediction of fiber-reinforce polymers. Degrieck and Van Paepegem (2001) classify existing fatigue models into three categories: fatigue life model (S-N curves), residual strength or residual stiffness model, and progressive damage model.

The fatigue life model is established based on S-N curves or Goodman diagrams. This approach does not consider the details of the damage mechanism. It is entirely empirical and needs a lot of experimental data. For every variation in laminates (different stacking sequence and ply orientation), a new set of specimens are needed to develop the S-N curves, thus making this approach expensive and time-consuming. But this methodology is easy to apply and a lot of commercial software packages are available for use. The failure criteria mimic the form of static strength criteria, based on two major failure modes, i.e. fiber failure and matrix failure (Hasin and Rotem, 1973; Reifsnider and Gao, 1991).

$$\begin{aligned} &\sigma_1 = \sigma_1^u \\ &\left(\frac{\sigma_2}{\sigma_2^u}\right)^2 + \left(\frac{\tau}{\tau^u}\right)^2 = 1 \end{aligned} \qquad (66)$$

where σ_1 and σ_2 are the stresses along the fiber direction and transverse to the fiber direction respectively, and τ is the shear stress. σ_1^u, σ_2^u, and τ^u are the ultimate strengths of the three stress components. They are functions of the stress level, stress ratio and the number of stress cycles. The relationship is expressed in S-N curves from previous experimental data.

Wu (1993), Jen and Lee (1998) proposed different failure criteria based on the Tsai-Hill criterion. Philippidis and Vassilopoulos (1999) proposed a failure criterion based on the Tsai-Wu criterion. All these methods use the fatigue strength (corresponding

to a given N, from the S-N curves) instead of the ultimate strength in the Tsai-Hill or Tsai-Wu criteria.

Other researchers directly use the family of S-N curves to calculate the fatigue life (Fawaz Z and Ellyin, 1994; Haris 1985; Bond, 1999). The family of S-N curves includes stress ratio, load frequency and other factors affecting the shape of the S-N curves. The main objective is to use the same computing methodology to account for different loading conditions.

The residual strength or residual stiffness model is based on damage mechanics, which relates fatigue failure to the damage evolution process. The degradation of stiffness or strength is correlated with a damage variable (damage index). Different damage evolution functions (Hwang and Han, 1986(a); Hwang and Han, 1986(b); Sidoroff and Subagio, 1987; Van Paepegem and Degrieck, 2000, Caprino et al, 1999; Whitworth, 2000; Yao and Himmel, 2000; Mao and Mahadevan, 2002) have been suggested based on some assumptions or experimental results. The failure is assumed to occur when the cumulative damage reaches a critical value (usually unity). The general form of the damage accumulation rule is:

$$\frac{dD}{dN} = f(D, \sigma_i, \varepsilon_i, N...) \qquad (67)$$

where D is the damage index, σ_i, ε_i are the stress and strain components, and N is the number of load cycles. The parameters in the damage model are calibrated through experimental observations or through reasonable assumptions.

Unlike the above two approaches in fatigue analysis, which are at the macroscopic level, the progressive failure model considers local damage mechanisms, such as delamination, local ply buckling, fiber breakage, etc. All these local damage

mechanisms lead to damage accumulation to the macroscopic material. Global failure occurs once the damage introduced by the local failure exceeds the global allowable level. This method is computationally complicated because it accounts for many failure mechanisms and is also related to damage accumulation. Tserpes et al. (2004) gives a progressive damage model which includes seven local failure modes, including material stiffness degradation.

The fatigue life model is easy to use and has an experimental data base. Also the commercial software and methodology are available to calculate the fatigue life. However, this model requires a lot of experimental work, which is sometime cost prohibitive. Most of the fatigue life models do not consider damage accumulation and are difficult to extend to complicated loading condition.

The residual strength and the stiffness model consider damage accumulation. The idea of the residual strength model is simple and easy to apply. But the damage evolution function is assumed and calibrated through constant amplitude tests. For composite materials, the damage mechanism is different under different stress levels and also depends on the load sequence. It is hard to use a simple damage accumulation rule to describe the damage evolution under complicated loading conditions.

The progressive model seems to be more accurate because it accounts for the detailed failure mechanism of the composite material. But for accurate analysis, this model requires that the damage introduced by local failure be correlated with the material properties degradation. A quantitative relationship in this regard is difficult to find and needs extensive experimental data. Also this model is computationally expensive and complicated, and thus is difficult to apply directly to engineering design.

Most of the fatigue models for anisotropic composite laminates are for single applied off-axis loading, which causes proportional multiaxial stress state within the laminates. Very few theoretical and experimental studies are found in the literature for the non-proportional multiaxial fatigue analysis of general anisotropic materials.

2.4.2 Proposed new multiaxial fatigue model

For anisotropic materials, the uniaxial and torsional fatigue strengths also depend on the orientations of the axes at the critical point within the material. In the proposed multiaxial fatigue criterion (Eq. (23) in Section 2.2.2), fatigue limits f_{-1} and t_{-1} become functions of the orientation θ, say, $f_{-1}(\theta)$ and $t_{-1}(\theta)$. In order to extend the fatigue model (Eq. (23)) to anisotropic materials, we need to specify a reference plane, on which the uniaxial and torsional strength of the anisotropic material can be evaluated. In the current model, the key point is to calculate the angle between the maximum normal stress amplitude plane and the characteristic plane. We define the reference plane for the anisotropic material as the plane that experiences the maximum normal stress amplitude. Thus, Eq (23) is rewritten as a unified multiaxial fatigue criterion:

$$\sqrt{\left(\frac{\sigma_{a,\alpha}}{f_{-1}(\theta_{max})}\right)^2+\left(\frac{\tau_{a,\alpha}}{t_{-1}(\theta_{max})}\right)^2+k\left(\frac{\sigma^H_{a,\alpha}}{f_{-1}(\theta_{max})}\right)^2}=\beta \qquad (68)$$

where θ_{max} indicates the direction of maximum stress amplitude. For isotropic materials, Eq. (68) reduces to Eq. (23) since the functions $f_{-1}(\theta)$ and $t_{-1}(\theta)$ become constants. Similarly, the fatigue life model for anisotropic materials can be expressed as:

$$\frac{1}{\beta}\sqrt{(\sigma_{a,c})^2+\left(\frac{f_{N_f}(\theta_{max})}{t_{N_f}(\theta_{max})}\right)^2(\tau_{a,c})^2+k(\sigma^H_{a,c})^2}=f_{N_f}(\theta_{max}) \qquad (69)$$

Eq. (69) can be rewritten as:

$$\frac{1}{p_{N_f}(\theta_{max})}\frac{1}{\beta}\sqrt{(\sigma_{a,c})^2+(\frac{1}{s_{N_f}(\theta_{max})})^2(\tau_{a,c})^2+k(\sigma_{a,c}^H)^2}=f_{N_f}(0) \qquad (70)$$

If the mean stress is also included into the model, Eq. (70) could be used.

$$\frac{1}{(1-\frac{\sigma_{m,max}}{f_{ref}})}\frac{1}{p_{N_f}(\theta_{max})}\frac{1}{\beta}\sqrt{(\sigma_{a,c})^2+(\frac{1}{s_{N_f}(\theta_{max})})^2(\tau_{a,c})^2+k(\sigma_{a,c}^H)^2}=f_{N_f}(0) \qquad (71)$$

where $s_{N_f}(\theta_{max})=\frac{t_{N_f}(\theta_{max})}{f_{N_f}(\theta_{max})}$ is the strength ratio of the torsional loading and the uniaxial loading along the direction of θ_{max}. $p_{N_f}(\theta_{max})=\frac{f_{N_f}(\theta_{max})}{f_{N_f}(0)}$ is the ratio of uniaxial strength along the directions of $\theta=\theta_{max}$ and $\theta=0$. The left side of Eq. (71) can be treated as an equivalent stress amplitude. It can be used to correlate with the fatigue life using the uniaxial S-N curve along the direction of zero degree.

The procedure for the fatigue analysis of anisotropic materials is almost identical with that of isotropic material. For any arbitrary loading history, the maximum stress amplitude plane is identified first. The uniaxial and torsional fatigue strength along this direction is also evaluated, usually from experimental data. Then the angle α and the material parameters are determined for different materials according to Table 2. Notice that, the quantity s in Table 2 is now redefined as $s=s_{N_f}(\theta_{max})=\frac{t_{N_f}(\theta_{max})}{f_{N_f}(\theta_{max})}$. Finally the equivalent stress amplitude and the fatigue life are calculated using Eq. (70) (or Eq. (71)) if mean stress is included).

For an arbitrary anisotropic material, the variation of the uniaxial and torsional fatigue strengths corresponding to the orientation of the axes is quite complex and requires extensive experimental work to quantify. However, for some special anisotropic materials, this can be simplified using one of strength theories available in the literature. In this paper, an example of orthotropic composite laminate is used for illustration.

Consider a fiber reinforced composite laminate. Several static strength theories have been proposed for orthotropic laminates, such as Tsai-Hill and Tsai-Wu theory (Daniel and Ishai, 1994). In this study, the Tsai-Wu theory is used. For the case of plane stress, the Tsai-Wu theory is expressed as:

$$F_{11}\sigma_1^2 + F_{22}\sigma_2^2 + F_{66}\sigma_6^2 + F_1\sigma_1 + F_2\sigma_2 + 2F_{12}\sigma_1\sigma_2 = 1 \qquad (72)$$

where σ_1 and σ_2 are the stresses along the fiber direction and transverse to the fiber direction, respectively, and σ_6 is the in-plane shear stress. F_{11}, F_{22}, F_{66}, F_{12}, F_1, and F_2 are strength parameters and can be calibrated using experiments.

$$\begin{cases} F_{11} = \dfrac{1}{s_L^+ s_L^-}, \quad F_1 = \dfrac{1}{s_L^+} - \dfrac{1}{s_L^-}, \quad F_{22} = \dfrac{1}{s_T^+ s_T^-} \quad , \quad F_2 = \dfrac{1}{s_T^+} - \dfrac{1}{s_T^-} \\ F_{66} = \dfrac{1}{s_{LT}^2}, \quad F_{12} = -\dfrac{(F_{11}F_{22})^2}{2} \end{cases} \qquad (73)$$

where $s_L^{(\pm)}$, $s_T^{(\pm)}$ are the strengths along the fiber direction and transverse to the fiber direction, respectively. The plus symbol indicates tension strength and the minus symbol indicates compression strength. s_{LT} is the in-plane shear strength. For the fatigue problem, the stress terms in Eq. (73) refer to the stress amplitudes along different directions. If the strengths are defined using stress amplitude values, the plus and minus

symbols in the above strength notation disappear since the stress amplitude is always positively defined. Thus, Eq. (72) and Eq. (73) are rewritten for the fatigue problem as:

$$F_{11}\sigma_1^2 + F_{22}\sigma_2^2 + F_{66}\sigma_6^2 + 2F_{12}\sigma_1\sigma_2 = 1 \tag{74}$$

$$\begin{cases} F_{11} = \dfrac{1}{s_L^2}, \quad F_{22} = \dfrac{1}{s_T^2}, \quad F_{66} = \dfrac{1}{s_{LT}^2} \quad , \quad F_{12} = -\dfrac{(F_{11}F_{22})^2}{2} \end{cases} \tag{75}$$

Using the Tsai-Wu strength theory, the uniaxial strength and shear strength along an arbitrary direction θ can be easily obtained as

$$\begin{cases} f(\theta) = 1/\sqrt{F_{11}\cos^4\theta + F_{22}\sin^4\theta + (F_{66} + 2F_{12})\sin^2\theta\cos^2\theta} \\ t(\theta) = 1/\sqrt{(F_{11} + F_{12} - 8F_{12})\sin^2\theta\cos^2\theta + F_{66}(\cos^2\theta - \sin^2\theta)^2} \end{cases} \tag{76}$$

For the fatigue life model, the fatigue strength parameters are also functions of the fatigue life (N_f), which can be evaluated from the experimental S-N curves. Eq. (76) is rewritten as:

$$\begin{cases} f_{N_f}(\theta) = 1/\sqrt{F_{11,N_f}\cos^4\theta + F_{22,N_f}\sin^4\theta + (F_{66,N_f} + 2F_{12,N_f})\sin^2\theta\cos^2\theta} \\ t_{N_f}(\theta) = 1/\sqrt{(F_{11,N_f} + F_{12,N_f} - 8F_{12,N_f})\sin^2\theta\cos^2\theta + F_{66,N_f}(\cos^2\theta - \sin^2\theta)^2} \end{cases} \tag{77}$$

Substituting Eq. (77) into Eq. (70), we can solve for the fatigue life (N_f). Similar to isotropic materials, Eq. (70) usually has no closed form solution. In practical calculation, a trial and error method can be used to find N_f. For an orthotropic composite laminate, the experimental S-N curves along the fiber direction, transverse to the fiber direction, and in-plane shear stress are required in the proposed model. Then the fatigue life under arbitrary multiaxial loading can be predicted.

The fatigue model for the isotropic material in Section 2.2 is consistent with the fatigue model for the anisotropic material in derived here. If $F_{11} = F_{22} = \frac{1}{3} F_{66}$, the fatigue model for the orthotropic material is identical with the fatigue model for the isotropic material with $s = \sqrt{3}$, in which the Tsai-Wu criterion reduces to be the Von-Mises criterion.

2.4.3 Comparison with experimental observations

The proposed multiaxial fatigue life prediction model is validated using experimental observations found in the literature. Three categories of data are explored: metals for isotropic material, unidirectional composite laminates for orthotropic material and multidirectional composite laminates for anisotropic material.

Twelve sets of fatigue experimental data are employed in this section, and are listed in Table 10. The collected materials cover several different industries, such as construction engineering, automotive engineering, and aerospace engineering and range from brittle to ductile.

The predicted fatigue lives and the experimental lives are plotted together in Fig. 12. In Fig. 12, the x-axis is the fatigue life and the y-axis is the equivalent stress amplitude which is calculated from Eq. (70). Both axes are in log scale. The dashed lines are the prediction results and the points are the experimental observations. In the legends, “uni” represents uniaxial loading, “tor” represents pure torsional loading, “pro” represents proportional multiaxial loading and “non-pro” represents non-proportional multiaxial loading. For data sets where mean stress data is available, mean stress effect is also included in the results.

As shown in Fig. 12, the predicted results agree very well with the experimental results despite different amounts of scatter for different materials. For different materials and loading conditions, the proposed model correlates the experimental observations together using the uniaxial fatigue S-N curve.

Table 10.Experimental data for isotropic metals

Material	References
SAE-1045 steel	Kurath et al (1989)
S45C steel	Kim et al (1999)
5% chrome work roll steel	Kim et al (2004)
SM45C	Lee (1989)
7010 aluminum alloy	Chaudonneret (1993)
Waspaloy	Jayaraman and Ditmars (1989) Learch et al (1984)
Hastelloy-X	Jordan (1985)
Hayness 188	Bonacuse et al (1992) Kalluri et al (1991)
1Cr-18Ni-9Ti stainless steel	Chen et al (2004)
Ti-6Al-4V alloy	Kallmeyer et al (2002)
AISI Type 304 stainless steel	Socie (1987)
Z12CNDV12-2 steel	Chaudonneret (1993)

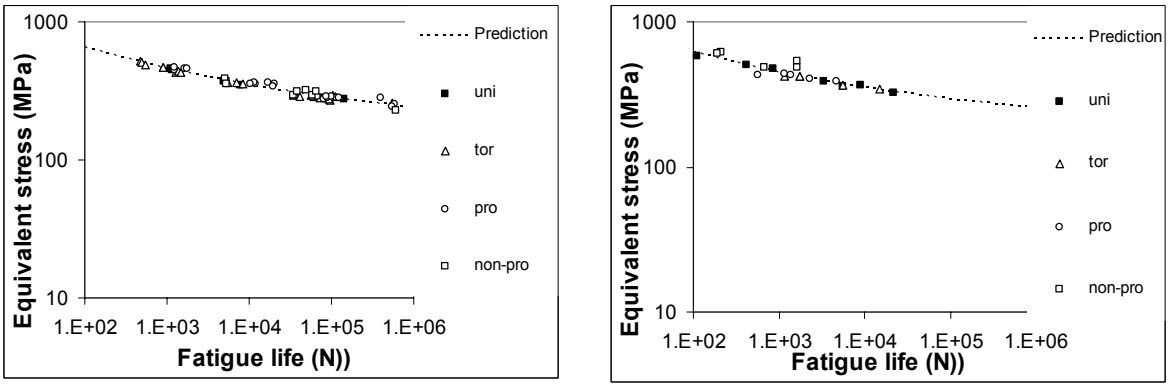

a) SAE-1045 steel b) S45C steel

Fig. 12 Comparisons of predicted and experimental fatigue lives for metals

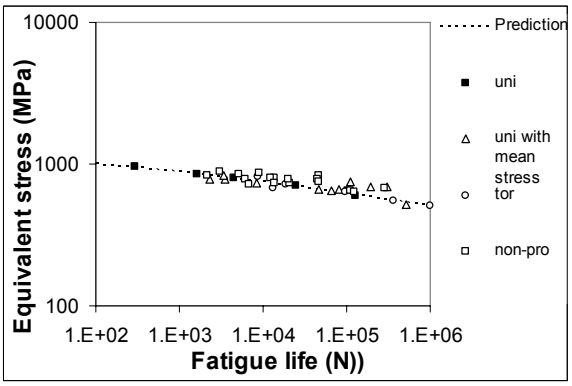

c) 5% chrome work roll steel

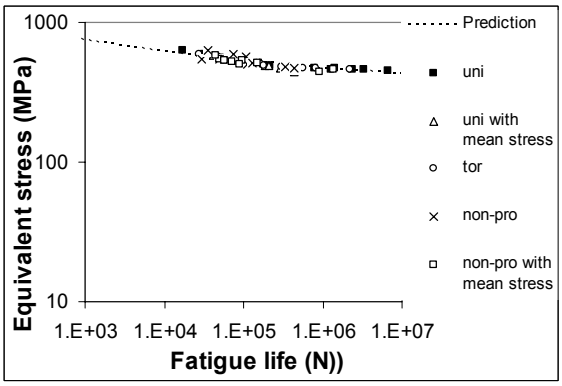

d) SM45C steel

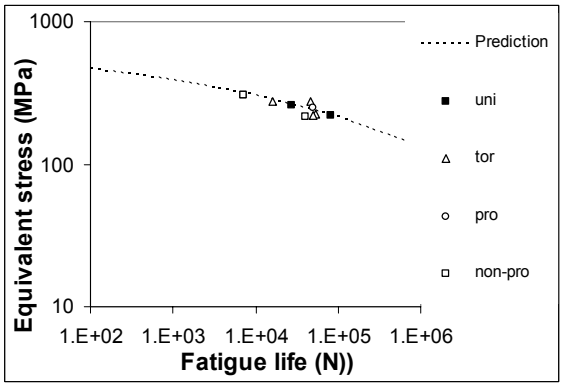

e) 7010 aluminum alloy

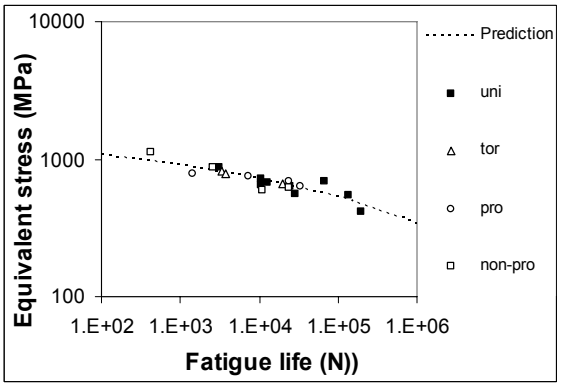

f) Waspaloy with treatment A

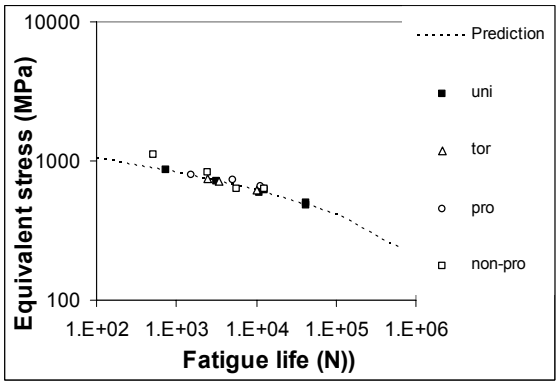

g) Waspaloy with treatment F

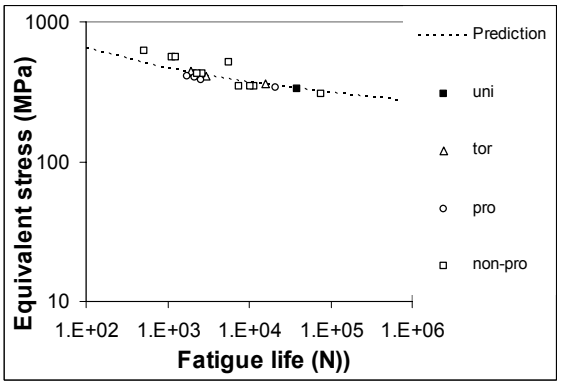

h) Hastelloy-X

Fig. 12 Cont.

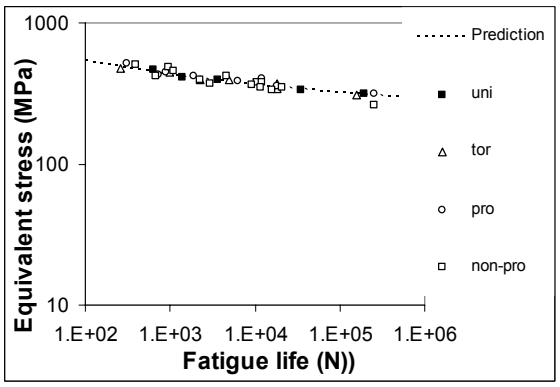

i) Hayness 188

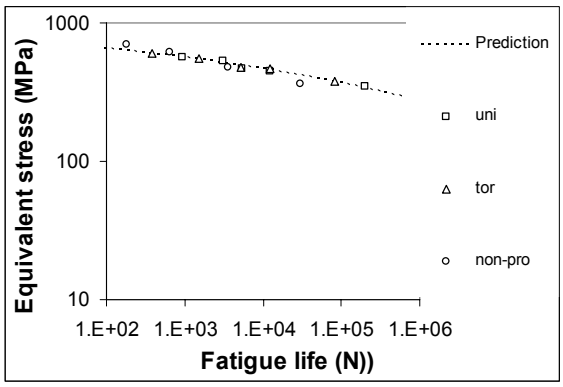

j) 1Cr-18Ni-9Ti steel--base metal

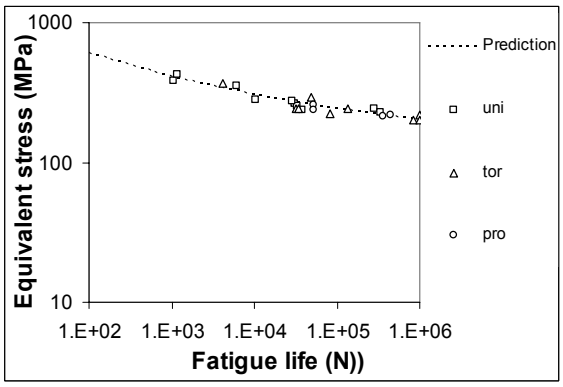

m) AISI Type 304 stainless steel

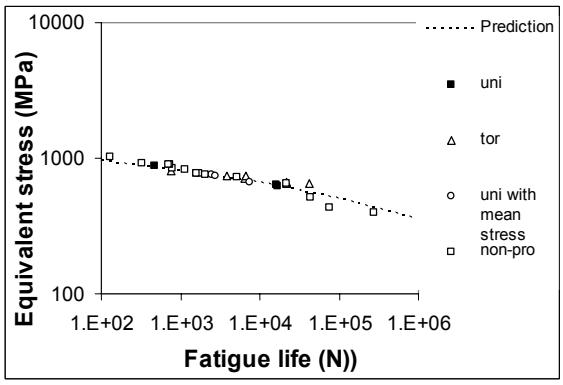

n) Z12CNDV12-2 steel

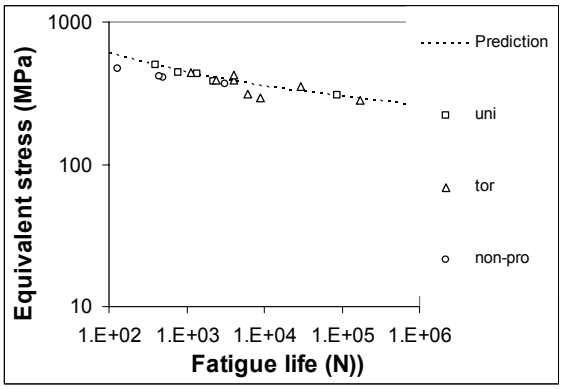

k) 1Cr-18Ni-9Ti steel--weld metal

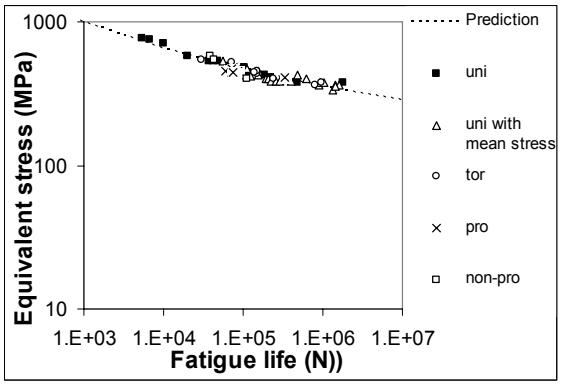

l) Ti-6Al-4V alloy

Fig. 12 Cont.

Eight sets of fatigue experimental data for unidirectional composite laminate under off-axis loading are employed in this section, and are listed in Table 11.

Table 11. Experimental data for unidirectional composite laminates

Material	References
E-glass/polyester	Philippidis and Vassilopoulos (1999)
E-glass fibre/epoxy-1	Kadi and Ellyin (1994)
T800H/epoxy	Kawai et al (2001(a))
T800H/polyimide	Kawai et al (2001(a))
AS4/PEEK	Kawai et al (2001(a))
GLARE 2(fibre–metal laminates)	Kawai et al (2001(b))
T800H/2500 carbon/epoxy	Kawai and Suda (2004)
E-glass fibre/epoxy-2	Hashin and Rotem (1973) Reported by Petermanna and Plumtreeb (2001)

In the proposed fatigue life model for orthotropic materials, experimental S-N curves for the fiber direction, transverse to the fiber direction, and pure in-plane shear stress are required. However, most of the fatigue experimental data do not include the pure shear test results. It is possibly due to the difficulty of applying the pure shear loading to the composite laminate. The S-N curve under pure shear loading is calibrated using one additional off-axis fatigue test data set and then used for fatigue life prediction for the other off-axis fatigue loadings.

The predicted fatigue lives and the experimental lives are plotted together in Fig. 13. In Fig. 13, the x-axis is the fatigue life and the y-axis is the equivalent stress amplitude which is calculated from Eq. (70). Both axes are in log scale. The dashed lines are the prediction results and the points are the experimental observations. The angles of the off-axis loading are shown in the legends. Only some of the references in Table 11, namely, Kadi and Ellyin (1994) and Kawai and Suda (2004) include the mean stress

effect on the fatigue life. Figs. 13(b) to 13(d) include this stress ratio, which is defined as the minimum stress divided by the maximum stress.

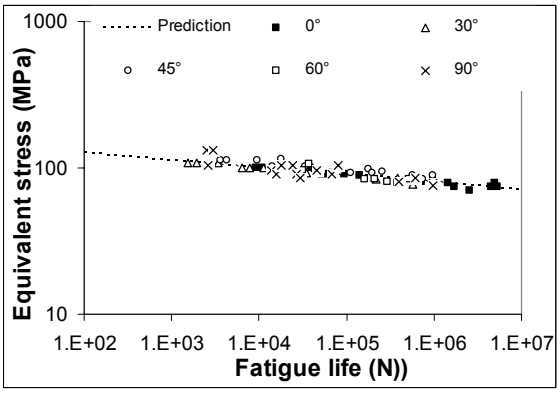

a) E-glass/polyester

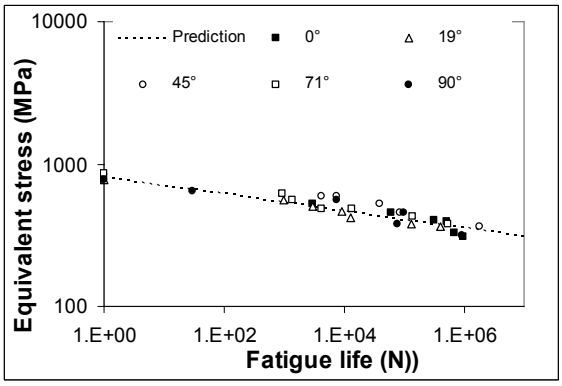

b) E-glass fibre/epoxy-1 with *R=-1*

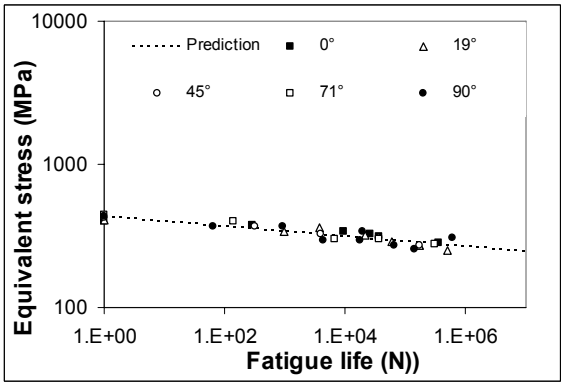

c) E-glass fibre/epoxy-1 with *R=0*

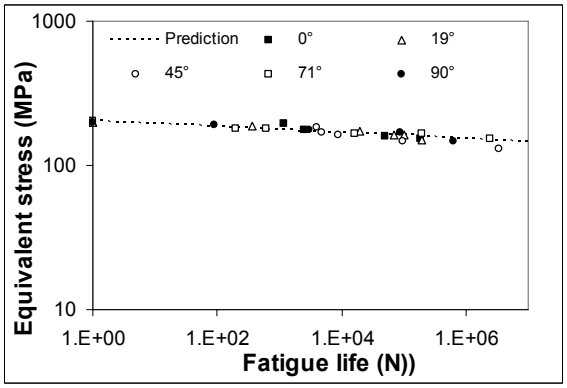

d) E-glass fibre/epoxy-1 with *R=0.5*

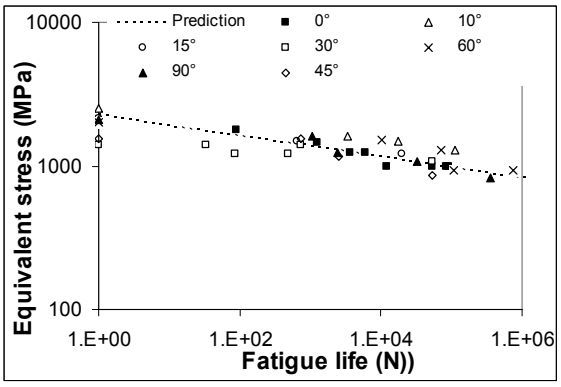

e) T800H/epoxy

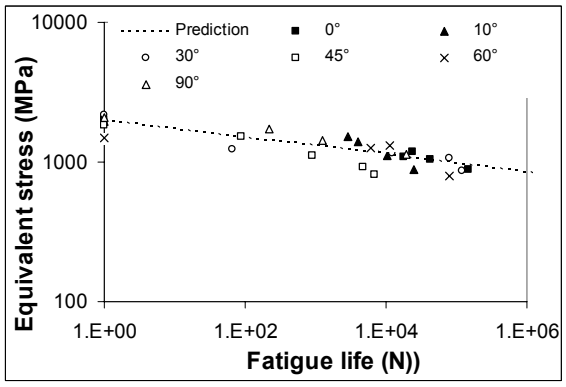

f) T800H/polyimide

Fig. 13. Comparisons of predicted and experimental fatigue lives for composites

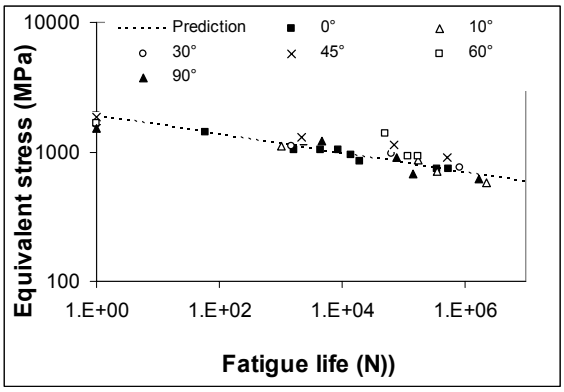

g) AS4/PEEK

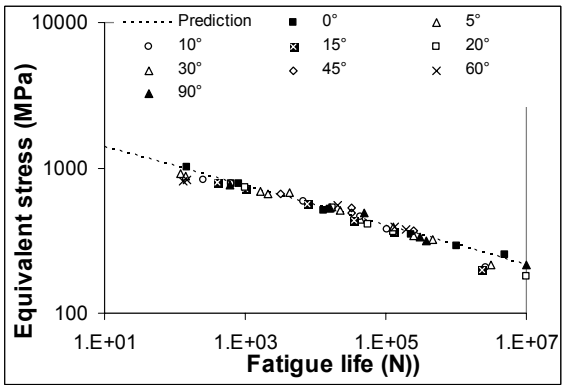

h) GLARE 2

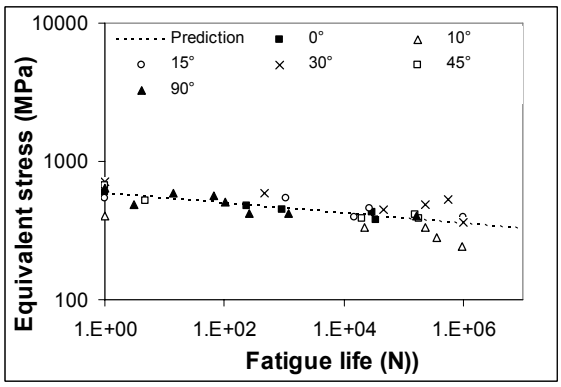

i) T800H/2500 carbon/epoxy with

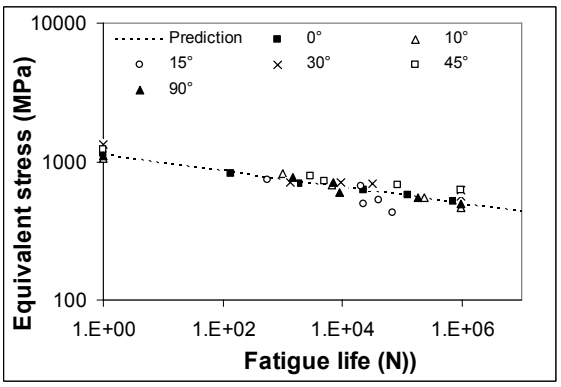

j) T800H/2500 carbon/epoxy with

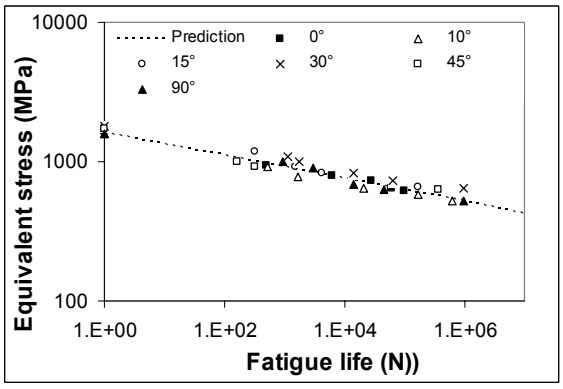

k) T800H/2500 carbon/epoxy with

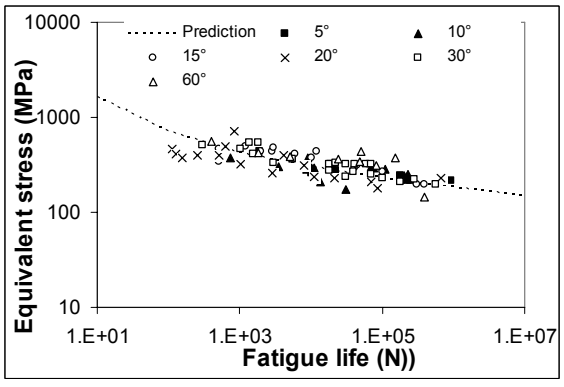

l) E-glass fibre/epoxy-2

Fig. 13 Cont

As shown in Fig. 13, the predicted results agree very well with the experimental results despite different amounts of scatter for different materials. Generally speaking, the scatter for composite laminates is larger than that for metals. The worst case is for E-glass fibre/epoxy-2 (Fig. 13(l)). In the original data, very large scatter was observed. A probabilistic approach may be more appropriate to describe the fatigue behavior of composite materials.

Composite structures are more likely to be in the form of multidirectional laminates consisting of multiple laminate or plies, which may have different ply orientations and stacking sequences. Due to the arbitrary combinations of the plies, the marco-mechanical properties of the multidirectional composite laminates are anisotropic. The fatigue analysis is more complicated than that for unidirectional composite laminates and requires extensive experimental work to quantify the effect of anisotropy. However, multidirectional composite laminates are built up with many orthotropic plies. For this type of material, the authors (Liu and Mahadevan, 2005(b)) developed a two-stage methodology for the fatigue analysis. First, divide the total loading history into several blocks. In each block, check the failure of each ply using the fatigue model. If no failure occurs, accumulate the fatigue damage for each ply caused in this block and progress to the next step. If failure occurs, assume that the ply strength and stiffness decrease to zero. Then update the global stiffness matrix and progress to the next step. The computation is continued till the entire laminate fails. This section uses this methodology. In each ply, the fatigue model derived for unidirectional composite laminate is used to check the failure.

Fatigue test data of glass-fiber-based multidirectional composite laminates (Mandell and Samborsky, 2003) are used to validate the proposed fatigue model. The material chosen, D155, is a balanced laminate which consists of pairs of layers with identical thicknesses and elastic properties but with $+\theta$ and $-\theta$ orientations. Again, the fatigue S-N curve for pure shear test is not available and the balanced laminate ($[\pm 45]_3$) is used to calibrate the shear S-N curve.

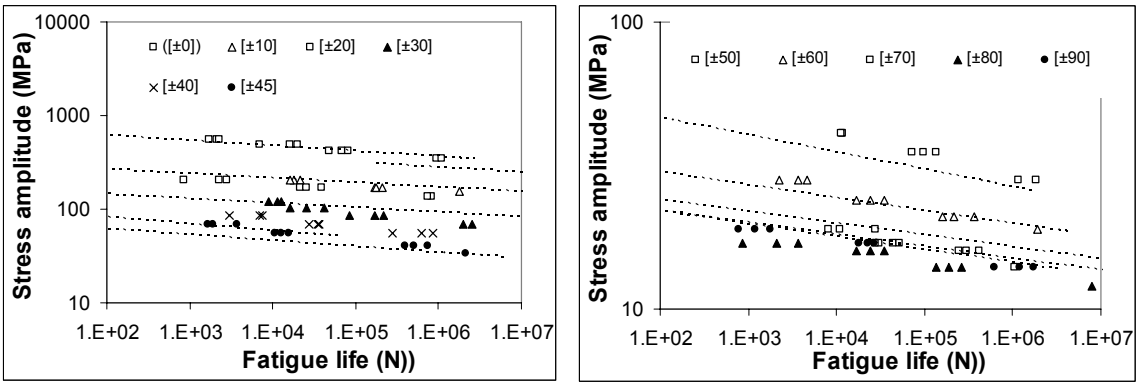

a) b)

Fig. 14. Comparisons of predicted and experimental fatigue lives for D155 with *R=0.1*

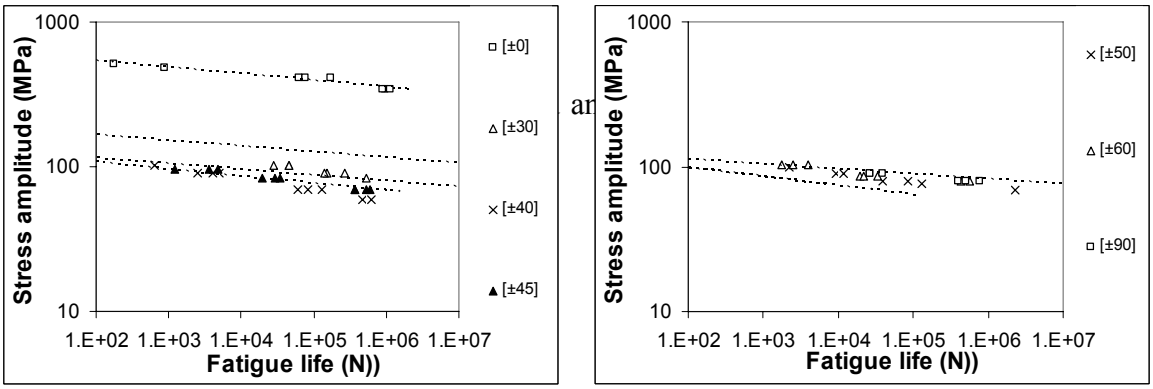

a) b)

Fig. 15 Comparisons of predicted and experimental fatigue lives for D155 with *R=10*

The prediction results and the experimental observations are plotted in Figs. 14-15. The x-axis is the fatigue life and the y-axis is the applied stress amplitude. The dashed lines are the prediction results and the points are experimental results.

From Figs. 14-15, the agreement is seen to be generally very good, with a few exceptions. In all cases, the predictions capture the major trends in the experimental observations. Very few multiaxial fatigue life prediction models are available in the literature for multidirectional composite laminates. Therefore, quantitatively comparison of the proposed model's performance with the others is difficult. However, if graphically compared with the prediction results for unidirectional composite laminates (e.g. Figs. 8-9 in Kawai (2004)), Figs. 14-15 show similar accuracy in the prediction results. Considering the large scatter inherent in the fatigue behavior of multidirectional composite laminates, a probabilistic fatigue model appears more appropriate to describe the fatigue behavior.

2.5 Mixed-mode fatigue crack propagation

The investigation of fatigue crack behavior using fracture mechanics has been largely focused on mode I loading (Plank and Kuhn, 1999). However, engineering components or structures are often subjected to both normal and shear loading (mode II and III). This type of fatigue problem is usually referred to either as the multiaxial fatigue problem for classical fatigue analysis (*S*-*N* or *e*-*N* curve approach) or the mixed-mode fatigue crack problem within the context of fracture mechanics. Several reviews of existing multiaxial fatigue models (You and Lee, 1996; Papadopoulos, 1997) and mixed-mode fatigue crack growth models (Bold et al, 1992; Qian and Fatemi, 1996) are

available in the literature. A comprehensive review and comparison of different models is not the objective of the current study and thus only a few of them are briefly described below.

2.5.1 Existing mixed-mode fatigue crack propagation models

For the mixed-mode fatigue crack analysis, two types of models can be found in the literature. A number of available models assume that the tensile crack growth dominates during the fatigue crack propagation. The Maximum Tangential Stress (MTS) criterion proposed by Erdogan and Sih (1963) and the Maximum Tangential Strain (MTSN) criterion proposed by Chambers et al (1991) are two typical models using the tensile failure mode assumption. Yan et al (1992) used an equivalent stress intensity factor defined on the maximum tangential stress plane, which also assumed the tensile failure mode. Many other models based on energy concepts, such as the energy release rate model (Forth et al. 2003), the strain energy density model (Sih and Barthelemy, 1980) and the dilatational strain energy density model (Theocaris and Andrianopoulos, 1982), can be also deemed as variations of a tensile failure-based model similar to the MTS criterion (Chao and Liu, 1997). Compared with a large number of models based on the tensile failure mode, relatively few models based on the shear failure mode are available in the literature. Otsuka et al (1975) observed Mode II crack growth in ductile steels and stated that fatigue cracks can either grow along the maximum tangential stress plane (mode I) or along the maximum shear stress plane (mode II). A similar approach for the crack growth under static loading has been proposed by Chao and Liu (1997), in which the MTS criterion and the MSS (maximum shear stress) criterion are combined together to predict the crack growth. Socie et al (1987) proposed an equivalent strain intensity

factor for the near threshold small crack growth, which is defined on the maximum shear strain plane. A similar approach was also proposed by Reddy and Fatemi (1992).

It is well known that models based on the tensile failure mode work well for brittle materials. For ductile materials, both mode I and mode II cracks could occur and the models based on a single failure mechanism cannot give a satisfactory prediction (Bold et al, 1992; Chao and Liu, 1997). For mixed-mode fatigue crack growth, it has been reported that the crack could change the growth mode depending on the applied loading amplitude (Gao et al, 1982). Gao et al (1982) observed that the near threshold crack growth is shear-mode and the crack branches to tensile-mode when the applied mixed-mode loading is gradually increased. This type of observation indicates that no single model based on a specific failure mechanism can be applied to the whole regime of the fatigue crack growth, i.e. from near-threshold crack growth to long crack growth, since the underlying failure mechanisms could be different.

For the fatigue problem under multiaxial loading, the non-proportionality of the applied loading is another important factor affecting the fatigue life. The effects of different loading paths on the fatigue crack initiation life have been studied by previous researchers (Itoh, 1995; Borodii and Strizhalo, 2000; Socie and Maquis, 2000, Liu and Mahadevan, 2005(b)). For mixed-mode fatigue crack propagation, several studies have focused on the non-proportionality effect (Bold et al, 1992; Plank and Kuhn, 1999; Feng et al, 2006). Feng et al (2006) observed different crack growth behavior under different loading paths with identical loading magnitude in the axial and the torsional directions and stated that many models using applied stress intensity range or *J-integral* range are not capable under this situation as they produce identical predictions under different

loading paths. A reasonable model for mixed-mode fatigue crack growth should consider the loading path effects.

2.5.2 Proposed mixed-mode fatigue crack model

In this section, a new model for mixed-mode fatigue crack threshold and growth rate prediction is proposed. The method is a non-local approach since it is developed using remote stresses rather than stresses near the crack tip. Two major advantages of the proposed model are that it can automatically adapt for different failure mechanisms and it considers the loading path effects. The multiaxial fatigue limit criterion proposed earlier (Section 2.2.2) is extended to develop a fatigue crack threshold criterion using the Kitagawa diagram (Kitagawa and Takahashi, 1976). Following this, an equivalent stress intensity factor is proposed for the crack growth rate prediction.

The concept of fatigue limit is traditionally used within the fatigue resistance design approach, which defines a loading criterion under which no marcroscopic crack will form. The concept of fatigue crack threshold is often used within the damage tolerant design approach, which defines a loading criterion under which the cracks will not grow significantly (Lawson et al, 1999). A link between the fatigue limit and the fatigue crack threshold was proposed by Kitagawa and Takahashi (1976). The fatigue limit against the crack size using the Kitagawa diagram is shown in Fig. 2. According to the well-known El Haddad model (El Haddad et al, 1979), the fatigue limit can be expressed using the fatigue threshold and a fictional crack length a. The crack length a represents the intersection of the smooth specimen fatigue limit and the LEFM (linear elastic fracture mechanics) fatigue threshold, i.e.

$$f_{-1} = \frac{K_{I,th}}{\sqrt{\pi a}} \qquad (78)$$

where $K_{I,th}$ is the fatigue crack threshold for mode I loading. A similar formula can be also expressed for mode II (or III) loading.

$$t_{-1} = \frac{K_{II,th}}{\sqrt{\pi a}} \text{ or } (t_{-1} = \frac{K_{III,th}}{\sqrt{\pi a}}) \quad (79)$$

where $K_{II,th}$ and $K_{III,th}$ are the fatigue crack thresholds for mode II and mode III loading, respectively.

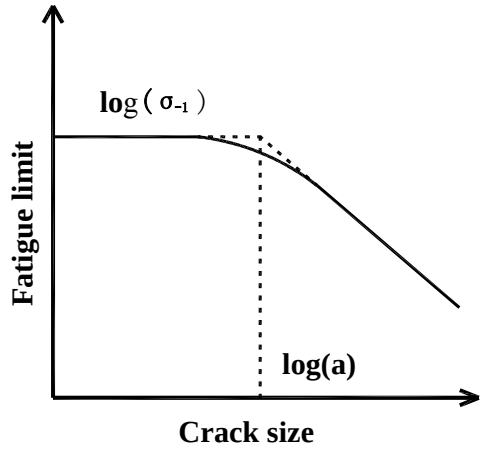

Fig. 16 Schematic representation of Kitagawa diagram for fatigue limits and fatigue threshold

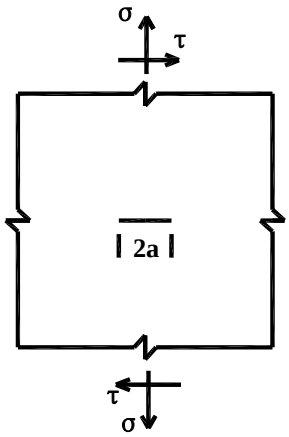

Fig. 17 Centered crack in a infinite plate under remote multiaxial stress

As discussed above, the Kitagawa diagram links the fatigue behavior of cracked and non-cracked material together. Using this concept, it is easy to extend the multiaxial fatigue limit criterion in Section 2.2.2 to a mixed-mode fatigue crack threshold criterion, as derived below.

For ease of discussion, first consider a simple problem as shown in Fig. 3. An infinite plate is under remote tensile stress and shear stress, which has a centered crack of length *2a*. This results in a mixed-mode I and II condition near the crack tip. Suppose the

remote tensile stress has a range of σ with zero stress ratio and the remote shear stress has a range of τ with zero stress ratio.

The range of the mode I stress intensity factor is

$$K_I = \sigma\sqrt{\pi a} \tag{80}$$

The range of the mode II stress intensity factor is

$$K_{II} = \tau\sqrt{\pi a} \tag{81}$$

Substituting Eqs. (80)-(81) into Eq. (23) and Table 2, we obtain

$$\sqrt{(\frac{k_1}{K_{I,th}})^2 + (\frac{k_2}{K_{II,th}})^2 + A(\frac{k^H}{K_{I,th}})^2} = B \tag{82}$$

where k_1, k_2 and k^H are loading-related parameters with the same units as stress intensity factor. For proportional multiaxial loading, they can be expressed as

$$\begin{cases} k_1 = \dfrac{K_I}{2}(1+\cos 2\alpha) + K_{II}\sin 2\alpha \\ k_2 = -\dfrac{K_I}{2}\sin 2\alpha + K_{II}\cos 2a \\ k^H = \dfrac{K_I}{3} \end{cases} \tag{83}$$

where α is the characteristic plane orientation. It can be expressed as

$$\alpha = \beta + \gamma \tag{84}$$

where β is the maximum normal stress amplitude plane orientation at the far field. For proportional loading, $\beta = \frac{1}{2}\tan^{-1}(\frac{2K_{II}}{K_I})$. A schematic representation of the characteristic plane orientation is shown in Fig. 18.

For general nonproportional loading, the axial loading and the torsional loading may not reach the maxima simultaneously. Numerical search is required to find the value

of β, k_1 and k_2 (Liu and Mahadevan, 2005(a)). γ has been defined in Table 1 earlier. Notice that s in Table 1 is redefined using the fatigue crack threshold under mode I and mode II loading as $s = \frac{K_{II,th}}{K_{I,th}}$. Eqs. (82) to (84) together with the material parameters defined in Table 2 are used for fatigue crack threshold prediction under general mixed-mode loading.

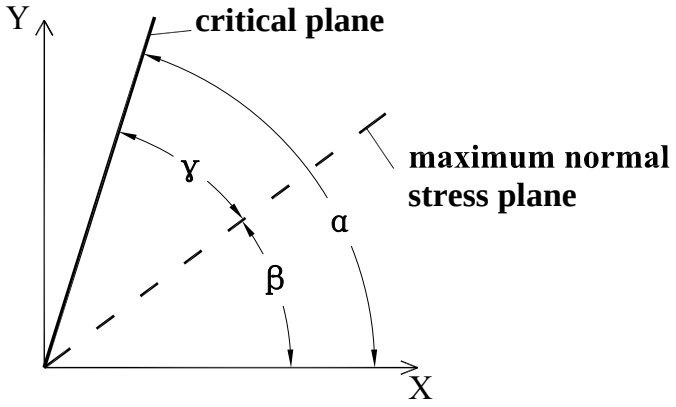

Fig. 18 Orientation of characteristic plane and maximum normal stress plane

In Eq. (82), k_1 and k_2 are loading-related parameters with the same units as the stress intensity factor. However, they are not the same as those defined in the fracture mechanics for kinked cracks (Cotterell and Rice, 1980). The equivalent stress intensities of kinked crack are obtained using the stress field near the crack tip. The proposed parameters are obtained using the remote stress transformation and thus we name the proposed model as a non-local approach.

Similar to Liu and Mahadevan (2005(a)), the ratio of mode II and mode I fatigue crack threshold $s = \frac{K_{II,th}}{K_{I,th}}$ is related two different material failure mechanisms. A larger

value of s ($s \geq 1$) indicates tension-dominated failure and smaller s ($s \leq \frac{1}{\sqrt{3}}$) indicates shear-dominated failure. If the value of s is known (based on uniaxial and pure torsional fatigue tests), the proposed model can automatically adapt for different failure mechanisms.

After developing the fatigue crack threshold criterion as above, the methodology for fatigue crack growth rate prediction is relatively easy. Notice that the fatigue crack threshold is often related to the stress intensity at a very low crack growth rate ($\frac{da}{dN} < 10^{-8} \sim 10^{-7}\, mm/cycle$). Eq. (82) can be rewritten as

$$\frac{1}{B}\sqrt{(k_1)^2 + (\frac{k_2}{s})^2 + A(\frac{k^H}{s})^2} = K_{I,th} \qquad (85)$$

The left side of Eq. (85) can be treated as the equivalent stress intensity. It can be used to correlate with the crack growth rate using the mode I crack growth curve. For prediction corresponding to a general crack growth rate *da/dN*, the fatigue thresholds ($K_{I,th}$ and $K_{II,th}$) may be replaced by the stress intensity coefficients at the specific crack growth rate ($K_{I,da/dn}$ and $K_{II,da/dn}$). Then the mixed-mode crack growth model is expressed as

$$K_{mixed,eq} = \frac{1}{B}\sqrt{(k_1)^2 + (\frac{k_2}{s})^2 + A(\frac{k^H}{s})^2} = K_{I,da/dn} = f(\frac{da}{dN}) \qquad (86)$$

where $f(\frac{da}{dN})$ is the crack growth curve obtained under mode I loading. The quantity s in Table 1 is redefined as $s = \frac{K_{II,da/dN}}{K_{I,da/dN}}$. Eq. (86) has no closed-form solution. In practical

calculation, a trial and error method can be used to find $\frac{da}{dN}$. For high cycle fatigue problem, $K_{II,da/dN}$ and $K_{I,da/dN}$ take initial values as $K_{II,th}$ and $K_{I,th}$, respectively. It is found that usually a few iterations are enough to make N_f converge. Eq. (86) together with the parameters in Table 2 may be used for fatigue crack growth rate prediction under mixed-mode loading.

The above derivation is for mixed mode I+II loading. Similar results can be obtained for mixed mode I+III loading. For isotropic materials, no difference is obtained for fatigue limit for in-plane shear stress or out-of-plane shear stress. These two different loadings result in mode II and mode III stress intensity factors if the frictional crack is included. Similar to Eq. (80), the mode III stress intensity factor can be expressed as

$$K_{III} = \tau\sqrt{\pi a} \tag{87}$$

Following the same procedure as described for mixed-mode I+II, the mixed mode I+III fatigue crack threshold and growth rate model can be also developed. They are almost same with those for mode I+II except all the mode II components are replaced by mode III components, i.e. K_{II}, $K_{II,th}$ and $K_{II,da/dN}$ are replaced by K_{III}, $K_{III,th}$ and $K_{III,da/dN}$, respectively.

$$\sqrt{(\frac{k_1}{K_{I,th}})^2 + (\frac{k_3}{K_{III,th}})^2 + A(\frac{k^H}{K_{I,th}})^2} = B \tag{88}$$

$$K_{mixed,eq} = \frac{1}{B}\sqrt{(k_1)^2 + (\frac{k_3}{s})^2 + A(\frac{k^H}{s})^2} = K_{I,da/dn} = f(\frac{da}{dN}) \tag{89}$$

If the material is under remote tensile stress, in-plane and out-plane shear stress, it results in mixed mode I+II+III loading on the crack. Compared with mode I+II and mode

I+III loading, the problem is more difficult, especially when none of these stress components is proportional. Eqs. (90) and (91) is used for general mixed mode loading. Following the same procedure for the mixed-mode I+II case, the formulas for general mixed mode I+II+III loading can be expressed as

$$\sqrt{(\frac{k_1}{K_{I,th}})^2+(\frac{k_2}{K_{II,th}})^2+(\frac{k_3}{K_{III,th}})^2+A(\frac{k^H}{K_{I,th}})^2}=B \qquad (90)$$

$$K_{mixed,eq}=\frac{1}{B}\sqrt{(k_1)^2+(\frac{k_2}{s})^2+(\frac{k_3}{s})^2+A(\frac{k^H}{s})^2}=K_{I,da/dn}=f(\frac{da}{dN}) \qquad (91)$$

2.5.3 Comparison with experimental observations

Table 12. Experimental threshold data used for model validation

Material name	References	Loading case	K_I,th(MPam$^{1/2}$)	s=$K_{II,th}/K_{I,th}$
6061Al	Wang et al(1995)	I+II	3.9	0.55
7075-T6 aluminum alloy	Otsuka et al (1987)	I+II	1.6	0.64
316 stainless steel	Gao et al (1982)	I+II	5.81	0.7
Aluminum alloy	Soh and Bian (2001)	I+II	2.75	0.83
2017-T3 aluminum alloy	Otsuka et al (1987)	I+II	1.6	0.9
Mild steel	Pook (1985)	I+III	6.6	1.1
2024Al	Liu and Wang (1996)	I+II	3.9	1.46
SiCp/2024Al composite	Liu and Wang (1996)	I+II	4.8	1.79

Eight sets of fatigue experimental data available in the literature are employed in this section, and are listed in Table 12. The predicted thresholds and the experimental observations are plotted in Fig. 19. In Fig. 19, the x-axis and the y-axis are the applied stress intensity ranges for mode I and mode II (or mode III), respectively. All values are

normalized using the mode I fatigue threshold. For comparisons, the predictions using the MTS, the maximum strain energy release rate and the minimum strain energy density are also plotted.

Two different formats of experimental data are collected. Several materials (6061Al, 316 stainless steel, mild steel, 2024Al, SiCp/2024Al composite) used the fatigue threshold values directly. Other materials (7075-T6 aluminum alloy, aluminum alloy, 2017-T3 aluminum alloy) used the values for initial growth crack and non-growth crack. For the later ones, predictions going through between the two sets of data points indicate good approximation, since the actual fatigue threshold values fall between the values of initial growth crack and non-growth crack. As shown in Fig. 19, the predicted values agree with experimental observations very well.

Theoretical *s* values for the MTS, the minimum strain energy density and the maximum strain energy release rate methods are 0.87, 0.96(plane strain) and 1, respectively, regardless of the material. When the material has a *s* value near one of the above numbers, the corresponding model gives a reasonable predictions (See Fig. 19(d) for aluminum alloy and Fig. 19(e) for 2017-T3 aluminum alloy. The actually observed *s* values for the material are shown in the figures). For materials with other *s* values, it is seen the above three models give poor predictions (See Figs. 19(a-c,f-h)). The proposed method generally gives better predictions than the available three models.

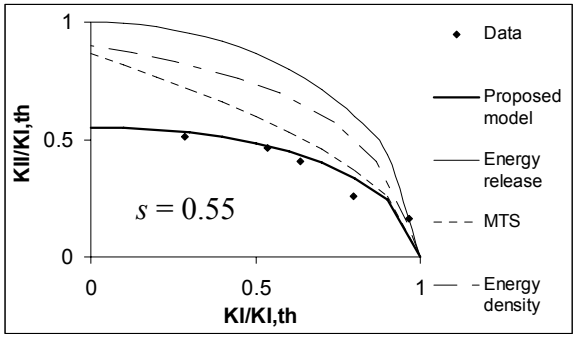

a) 6061Al

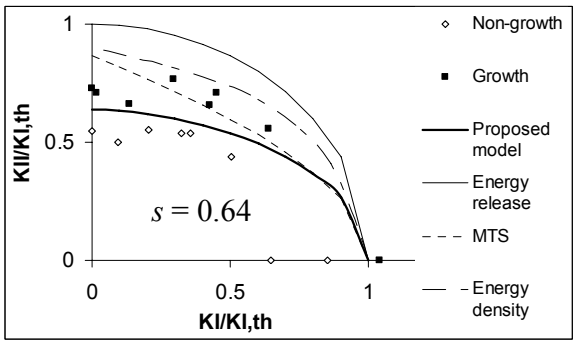

b) 7075-T6 aluminum

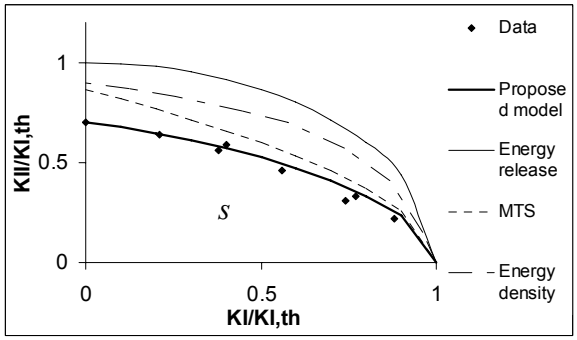

c) 316 stainless steel

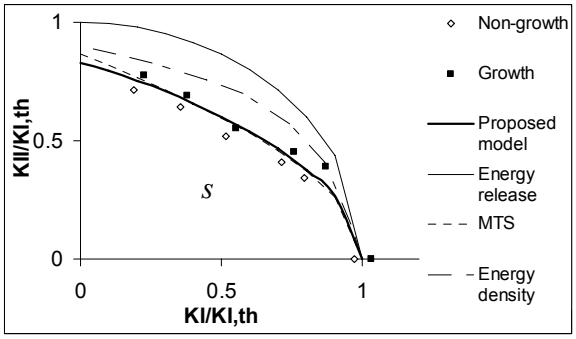

d) Aluminum alloy

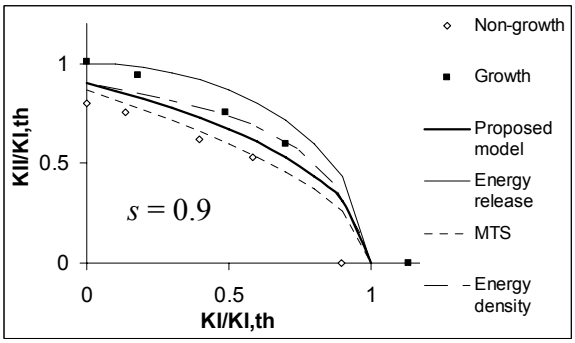

e) 2017-T3 aluminum

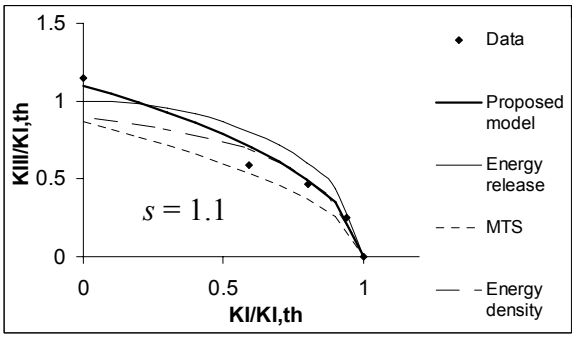

f) Mild steel

Fig. 19 Comparisons of predicted and experimental fatigue thresholds

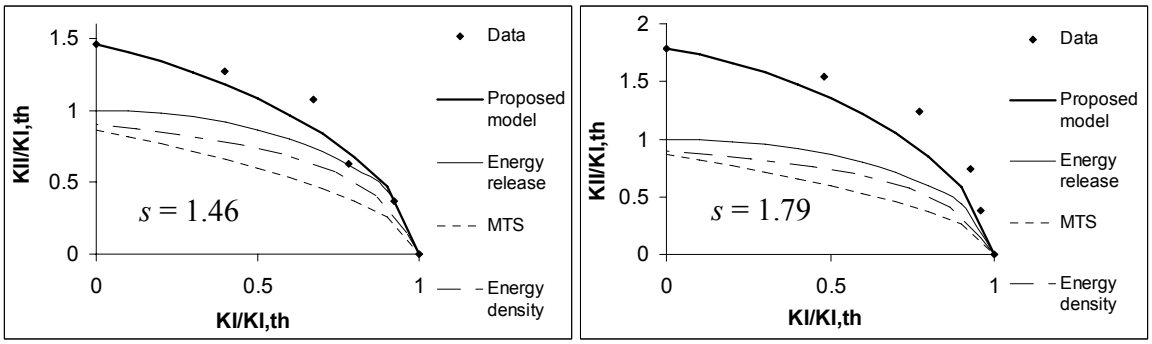

g) 2024 Al h) SiCp/2024Al composite

Fig. 19 Cont.

Table 13. Experimental crack growth rate data used for model validation

Material name	References	Loading case
3.5NiCrMoV forging steel	Yates and Mohammed (1996)	I+III
Rail steel	Kim and Kim (2002)	I+II
Metal X	Yokobori et al (1985)	I+II
304 stainless steel	Biner (2001)	I+II

Four sets of fatigue experimental data are employed to validate the fatigue crack growth model, and are listed in Table 13. The predicted crack growth rates and experimental observations are plotted in Fig. 20. In Fig. 20, the x-axis is the equivalent applied stress intensity range (Eq. (89)) under mixed-mode loading. The y-axis is the fatigue crack growth rate. Different types of mixed mode loading are represented using an angle φ, which is listed in the legend. The angle φ is defined as

$$\varphi = tan(\frac{K_I}{K_{II}}) \qquad (92)$$

As shown in Fig. 20, the proposed model correlates different types of mixed mode crack growth rates using the mode I crack growth function. It needs to be pointed out that

the proposed model is not tied to a specific function format to represent the experimental data. Instead of using the commonly used Paris law or other model forms, the best regression model form is used to represent the experimental mode I data and to predict the crack growth rate under mixed mode loading.

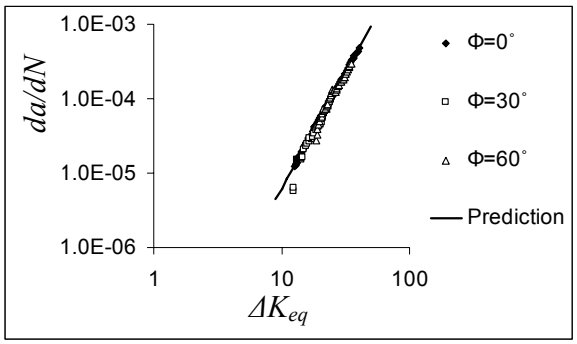

a) Rail steel, *R=0.1*

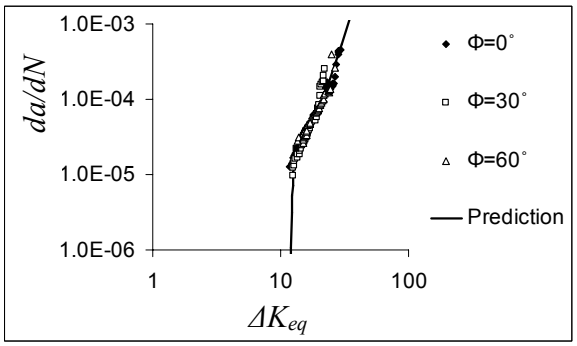

b) Rail steel, *R=0.5*

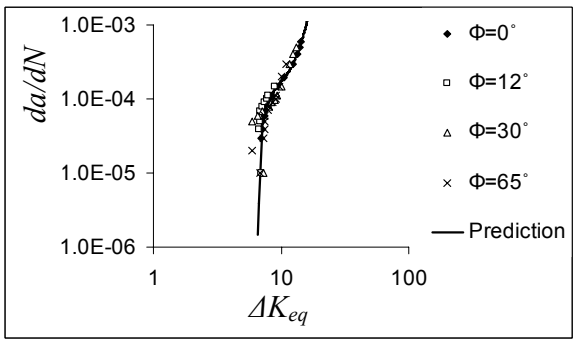

c) Metal X

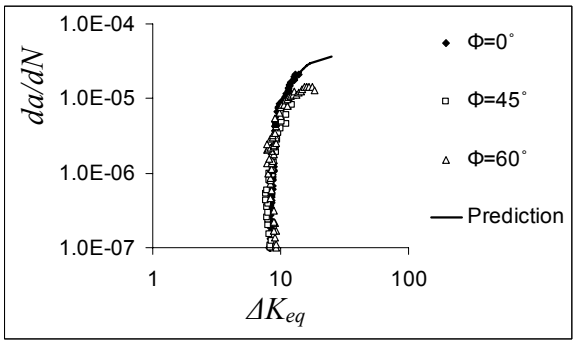

d) 3.5NiCrMoV forging

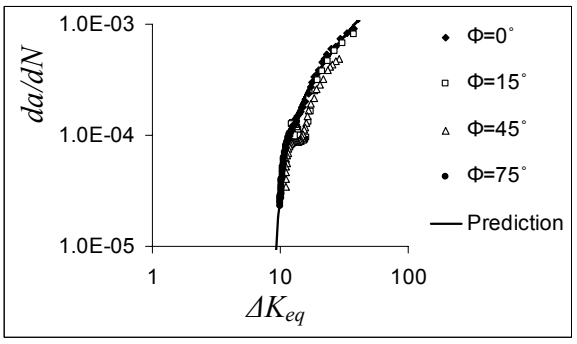

e) 304 stainless

Fig. 20 Comparisons of predicted and experimental fatigue crack growth rates

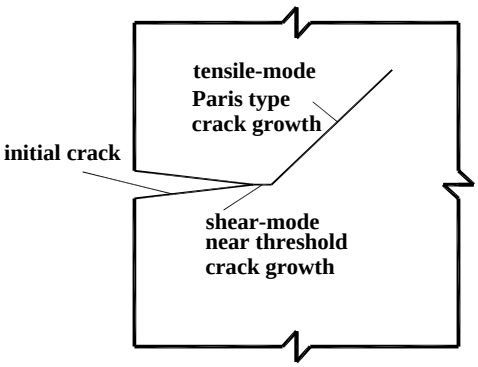

a) Schematic representation of crack growth from shear-mode to tensile-mode

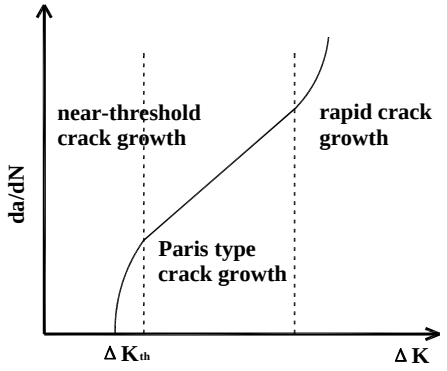

b) Schematic representation of crack growth of different regimes

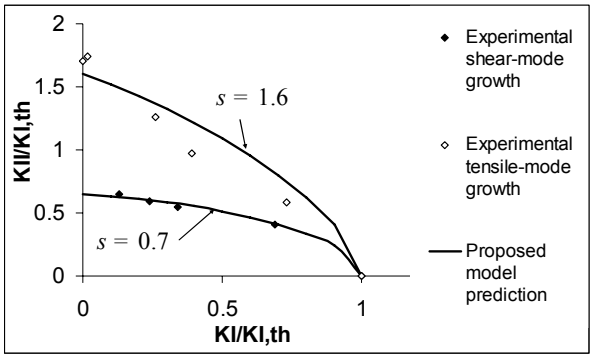

c) Shear-mode and tensile-mode fatigue crack threshold of 316 stainless steel

Fig. 21 Comparisons of predicted and experimental fatigue crack growth rates

One typical observation of mixed mode crack growth is that the underlying failure mechanism might change at different stages. Gao et al (1982) observed that fatigue crack initially propagates in a shear-mode. After growing a few grain diameters, a tensile-mode growth was observed and continued until failure. A schematic plot of the fatigue crack growth is shown in Fig. 21(a). It is well known that the total fatigue crack growth regime

can be divided into three sub-regimes: near-threshold crack growth, Paris law-type crack growth and rapid crack growth, as shown schematically in Fig. 21(b) (Suresh, 1998). Gao's observations (Gao et al, 1982) indicate that both the fatigue crack growth rates and the underlying mechanisms are quite different for near-threshold crack growth and Paris law-type type crack growth. It can be expected that any single failure mechanism-based model can not be applied to such conditions since their physical basis is violated.

However, the proposed model can easily adapt for different failure modes, and thus is capable of representing both near-threshold crack growth and Paris law-type crack growth. Gao's (Gao et al, 1982) experimental observations for shear-mode and tensile-mode crack growth thresholds are plotted in Fig. 21(c). The predictions using the proposed model are also plotted. It is observed that the proposed model works well for both failure modes, i.e., $s = 0.7$ (shear dominated) and $s = 1.6$ (tension dominated).

For multiaxial fatigue or mixed-mode fatigue crack problem, the non-proportionality of the applied loading affects the final fatigue damage. Models purely based on the applied loading amplitude cannot capture the loading path effect. The proposed model is developed from a characteristic plane-based model, which considers the loading path effect. In the proposed model, the characteristic plane depends on the maximum normal stress amplitude plane during the cyclic loading. For loadings with identical amplitudes but different loading paths, the maximum stress amplitude planes are different. Thus the fatigue damage prediction is also different.

Most fatigue tests for cracked specimens are performed by applying uniaxial fatigue loading on a plate with an inclined crack. This causes proportional loading ahead of the crack tip. Fatigue tests for cracked specimens under general nonproportional

loading are seldom found in the open literature. Liu and Mahadevan (2005(a;b)) have shown that the proposed concept accurately predicts the loading path effect for the fatigue limit prediction, which is the same as fatigue threshold predictions following the assumption of the Kitagawa diagram. For the fatigue crack growth under general nonproportional loading, experimental data is needed to validate the proposed model.

2.6 Summary

Multiaxial fatigue models for several situations are developed in this chapter, based on a characteristic plane approach. The predictions based on the proposed criterion show good agreement with the fatigue experimental data in the open literature. Most of the existing characteristic plane-based models can only be applied to certain types of failure modes, i.e. shear dominated failure or tensile dominated failure. Their applicability generally depends on the material's properties and loading conditions. In the proposed model, the characteristic plane changes corresponding to different material failure modes, thus making the proposed model have almost no applicability limitation with respect to different metals. The characteristic plane is theoretically determined by minimizing the damage introduced by the hydrostatic strain amplitude. The mean stress effect is also included in the proposed model through a mean stress effect correction factor.

One of the advantages of the proposed approach is that it can automatically adapt for different failure mechanisms, namely shear-dominated failure and tension-dominated failure. From Table 2, it can be seen that the characteristic plane in the proposed model depends on the material property s. It has been shown that s, the ratio of shear strength

coefficient and tensile strength coefficient, is related to the material ductility (Liu and Mahadevan, 2005(a)) and to the material failure modes (Liu and Mahadevan, 2005(b)). Once the *s* value is known, the proposed model can be used to predict the crack growth for any failure mechanism.

A useful mechanical parameter is found during the development of the proposed approach. The ratio of torsional fatigue strength and uniaxial fatigue strength *s* appears to be very important for the multiaxial fatigue problem. According to the proposed multiaxial fatigue theory and the experimental data collected in this study, different material failure modes may be related to this parameter. Also, from the experimental results collected from the literature, this parameter shows a good correlation to the extra hardening of the material caused under nonproportional loading. It is shown that there are no systematic errors in the model, for various material properties and loading conditions.

There are some other advantages of the proposed approach. The fatigue fracture plane is also determined and directly related to the characteristic plane. The calculation is relatively simple. In the fatigue life prediction model, no special requirements are needed for the form of the S-N curve function. The users can choose any S-N curve function form for the best regression results. The mean stress effect is also included in the model through a general mean stress effect correction factor. The factor can be calibrated using experimental fatigue test data with mean stress, or the empirical formula suggested by the author, may be used instead.

The proposed fatigue crack growth model is a non-local approach, which is developed using the remote stress components and the characteristic plane concept. Most of the existing fatigue crack growth models can only be applied to individual failure

modes, i.e. shear dominated failure or tension dominated failure. Their applicability generally depends on the material's properties and loading conditions. In the proposed model, the characteristic plane changes corresponding to different material failure modes, thus helping the proposed model to have a wide range of applicability.

The proposed model is also capable of handling nonproportional mixed-mode loading. Compared with many of the existing fatigue crack growth models, which give identical predictions for the experiments with same amplitudes but different loading paths, the proposed model gives different predictions as should be expected. However, further experimental work is required to validate the proposed methodology.

CHAPTER III

APPLICATION TO RAILROAD WHEELS

3.1 Overview

Several multiaxial fatigue life prediction models have been developed in the previous chapter. In this chapter, those models are applied to the wheel/rail rolling contact problem. The models described in the last chapter are improved and combined with new numerical techniques to achieve both computational accuracy and efficiency.

The multiaxial fatigue crack initiation model is extended for general three-dimensional components under multiaxial non-proportional loading. A numerical search technique using Euler angle transformation is adopted into the multiaxial fatigue theory to reduce the computational effort for fatigue fracture plane and characteristic plane identification.

A three-dimensional elasto-plastic finite element model for the wheel/rail contact problem is used for stress analysis. A submodeling technique is used to achieve both computational efficiency and accuracy. Then the fatigue damage in the wheel is evaluated numerically using the stress history during one revolution of the wheel rotation. Several important factors that affect the wheel failure are explored. These include axle loading, wheel geometry and material properties. Parametric study is performed to evaluate the importance of these factors.

The initial crack location and geometry from the crack initiation analysis is used for fatigue crack propagation analysis. The previous developed mixed-mode crack

propagation model is combined with finite element model to simulation the crack propagation within railroad wheels. A frictional crack is built into the sub-model and the stress intensity histories along the crack tip are used to evaluate the crack propagation rate. Several important factors affecting the crack propagation life are explored, such as wheel diameter, applied loading, crack profile and material properties.

The crack initiation life and the crack propagation life are combined together to give the total life to failure of railroad wheels. The results of this chapter will be used for stochastic fatigue modeling and reliability analysis in Chapters 4.

3.2 Crack initiation in railroad wheels

Damage accumulation due to fatigue, plastic deformation and wear significantly reduces the service life of the railway track. In recent years, higher train speeds and increased axle loads have led to larger wheel/rail contact forces. Also, efforts have been made to optimize wheel and rail design. This evolution tends to change the major wheel rim damage from wear to fatigue (Tournay and Mulder, 1996). Unlike the slow deterioration process of wear, fatigue causes abrupt fractures in wheels or the tread surface material loss. These failures may cause damage to rails, damage to train suspensions and, in rare cases, serious derailment of the train.

The fatigue problem of railroad wheels is often referred to as rolling contact fatigue (Johnson, 1990), and is caused by repeated contact stress during the rolling motion. The proper understanding of the underlying mechanism of rolling contact fatigue requires detailed knowledge of the interaction between wheel and rail. A proper multiaxial fatigue damage accumulation model under complex rolling contact stress state

is also required. An overview of rolling contact problem of railroad wheels was given by Ekberg and Kabo (2005).

In this section, first the previously developed multiaxial high-cycle fatigue damage model of Chapter 2 is extended to general 3D stress states. Both the initiation crack plane orientation and fatigue initiation life can be predicted based on the proposed model. Then a three-dimensional finite element model for wheel/rail rolling contact analysis is developed. Submodeling technique is used to achieve both computation efficiency and accuracy. The stress response of numerical simulation of the wheel rolling motion is used for fatigue life prediction. The influences of several parameters are evaluated and several conclusions are drawn based on the present results. The method developed in the current study is very valuable for fatigue resistance design and inspection planning of railroad wheels.

3.2.1 Previous work

Railroad wheels may fail in different ways corresponding to different failure mechanisms (Stone and Moyar, 1989; Marais, 1998; Mutton et al, 1991). Ekberg and Marais (1999) divide the wheel fatigue failure modes into three different failure types corresponding to different initiation locations: surface initiated, subsurface initiated and deep surface initiated fatigue failures. On the tread surface, there are usually two types of cracks. One is caused by the repeated mechanical contact stress. The other is initiated by thermal stresses arising from on-tread friction braking. The thermal cracks appear as short cracks oriented axially on the wheel tread (Gordon and Perlman, 1998).

According to the Union Pacific Railroad wheel fracture database (Snyder, 2003), 65 percent of railroad wheel failures are caused by shattered rims, 5 percent by thermal

cracking, and the other 30 percent by vertical split rim. Thermal cracking usually breaks off a piece of the wheel tread, while shattered rim can destroy the wheel's integrity and thus is more dangerous. Subsurface-initiated failures (shattered rim) are the types of failures we focused on in this dissertation. Studies on surface-initiated fatigue have been developed elsewhere (Moyar and Stone, 1991; Giménez and Sobejano, 1995; Marais and Pistorius, 1994).

Shattered rim failures are the result of large fatigue cracks that propagate roughly parallel to the wheel tread surface (Stone et al, 2002; Giammarise and Gilmore, 2001). Berge (2000) and Stone and Geoffrey (2000) suggest that the large stress, perhaps due to wheel/rail impact or material discontinuity, is responsible for the initiation of shattered rims. It is no doubt that voids and inclusions in a sufficient size in a stress field will lead to failure of wheels. Significant improvements have been made in recent years to prevent shattered rim failure, such as tight regulations in wheel manufacturing inspection, etc. However, these only help to reduce the occurrence of some shattered rims, but will not prevent the formation of all of them (Stone et al, 2002). Ekberg et al (2002) reported that the shattered rim can initiate from both inclusions and non-inclusion locations. More importantly, the "new" wheels may have a better resistance to the shattered rim failure, but this is not necessarily true for millions of "old" wheels that are still in use. The final objective of this project is to find an optimized inspection and maintenance plan for the "old" wheels in order to reduce shattered rim failures.

There are two major difficulties in rolling contact fatigue analysis. One is that the mechanical component is usually under non-proportional multiaxial stress state. Multiaxial fatigue theory is needed to handle this type of fatigue problem for initiation

life prediction. There is no universally accepted multiaxial fatigue model (Papadopoulos et al, 1997). The other difficulty is how to accurately describe the stress state under contact condition. Analytical solutions, such as the Hertz contact theory (Johnson, 1985), are easy to use if the problems satisfy the assumptions in Hertz contact theory. However, some practical problems cannot meet the required assumptions in the Hertz contact theory. For example, this theory assumes that the contact area is small compared to body dimension and surface curvature. For the wheel/rail contact problem, when the contact area is near the wheel flange, the surface curvature is comparable with the contact area and thus the Hertz contact theory is not applicable. In order to overcome the limitations inherent in the analytical solution, numerical methods for contact analysis, such as finite element method and boundary element method, are widely used.

Guo and Barkey (2004) use a 2D finite element model and a multiaxial fatigue model developed by Fatemi and Socie (1988) for bearing rolling contact fatigue analysis. Sraml et al (2003) use the Hertz contact theory to calculate the stress response and treat the multiaxial fatigue problem as a uniaxial fatigue problem. The principle stress/strain component in one direction is used for fatigue analysis. Ringsberg (2001) developed a semi-analytical approach for stress calculation, which used 3D finite element analysis but applied the contact pressure based on Hertz theory. The multiaxial fatigue model is a critical-plane based model which uses the damage parameter proposed by Jiang and Sehitoglu (1999). Ekberg et al (1995) developed a fatigue life prediction methodology for the wheel/rail contact fatigue problem, which uses the Hertz contact theory for stress calculation and multiaxial fatigue model proposed by Dang Van et al (1989).

Most of the existing rolling contact fatigue models use a simplified stress calculation technique, such as Hertz analytical solution or simplified finite element analysis. Due to the complex geometry of the wheel/rail contact area, it is more appropriate to use a 3D finite element method to calculate stress response in the mechanical components. It is also better to include the some factors which cannot be included into the simplified method, such material nonlinearity, irregular surface condition and hunting movement of the wheel.

Most of the available multiaxial fatigue models are limited in applicability to narrow range of material properties. More important, some of them cannot predict the initial crack plane orientation, which is another distinct characteristic of multiaxial fatigue problem and very important for crack propagation analysis later. Liu and Mahadevan (2005(a)) have proposed a new multiaxial fatigue theory, which is applicable to a wide variety of ductile and brittle metals and also directly correlates the characteristic plane orientation and initial crack plane orientation. This paper extends the new multiaxial fatigue theory to general three dimensional stress state and applies it to the wheel/rail rolling contact fatigue problem.

3.2.2 Improvement of previous multiaxial fatigue theory

The multiaxial fatigue model developed in Section 2.2.2 and validated using bending-torsional experiments, is suitable only usually for 2-D state of stress and includes one normal stress and one shear stress (in-plane) on the characteristic plane. For the general 3D state of stress, one normal stress and two shear stresses (one is in-plane and the other is out-of-plane) on the characteristic plane need to be included. In that case, the computation is more complex, partly due to the definition of stress amplitude. On an

arbitrary material plane across the point in consideration, the normal stress amplitude acting on the plane can be fully described by its algebraic value, since its direction will not change during one stress cycle. However, for the shear stress acting on the plane, its amplitude and direction will generally change during one stress cycle (Papadopoulos et al, 1997).

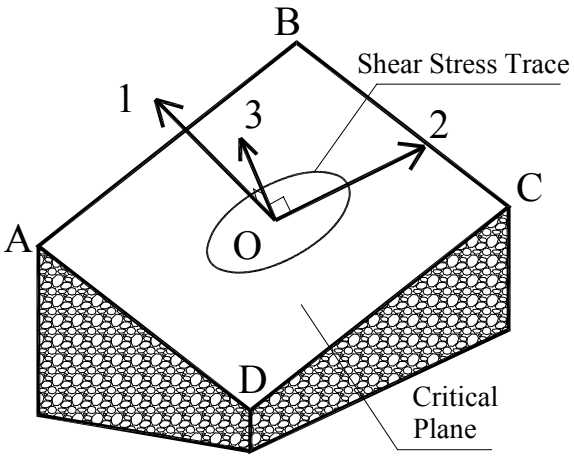

Fig. 22 Characteristic plane definition

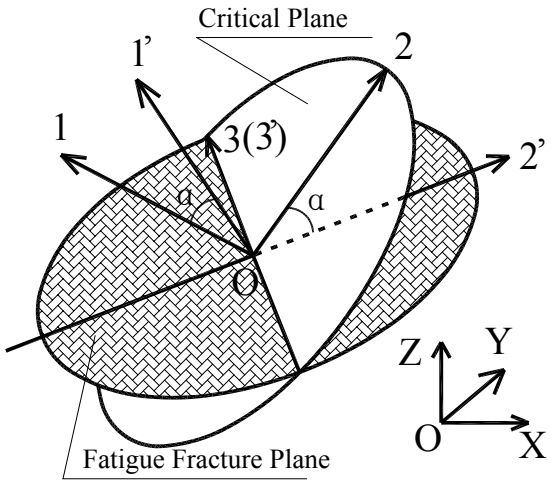

Fig. 23 Relationship of characteristic plane and fatigue fracture plane

As shown in Fig. 22, ABCD is the material plane across the point O. 1 is the normal vector of the plane ABCD. The normal stress amplitude acting on the plane ABCD is defined along the 1 direction. In this paper, shear stress amplitude on the plane ABCD is defined on an orthogonal coordinate system O23, which makes the shear stress amplitude value achieves maxima along the 2 direction. The shear stress amplitude along the 3 direction is included into the fatigue analysis. Eq. (23) is then rewritten as

$$\frac{1}{\beta}\sqrt{[\sigma_{a,c(1)}(1+\eta_{N_f}\frac{\sigma_{m,c(1)}}{f_{N_f}})]^2+(\frac{f_{N_f}}{t_{N_f}})^2(\tau_{a,c(2)})^2+(\frac{f_{N_f}}{t_{N_f}})^2(\tau_{a,c(3)})^2+k(\sigma_{a,c}^H)^2}=f_{N_f} \quad (93)$$

where the subscripts (1), (2), (3) of $\sigma_{a,c}$, $t_{a,c}$ and $\sigma_{m,c}$ indicate the directions of the stress amplitude. For the bending-torsion problem, one component of shear stress amplitude reduces to zero, and Eq. (93) reduces to Eq. (23).

For an arbitrary stress history of the point concerned, the initial fatigue crack plane and the characteristic plane are not known a priori. All possible planes through the point concerned are explored. For a biaxial fatigue problem, such as bending and torsion fatigue, it is relatively easy to identity the fatigue fracture plane and characteristic plane. For general 3D stress problem, an efficient simple procedure is proposed as shown below.

Consider the stress transformation equation

$$[\sigma]_{x'y'z'} = [T][\sigma]_{xyz}[T]^T \qquad (94)$$

where $[\sigma]$ is the stress matrix, subscripts xyz and x'y'z' refers to the two coordinate systems. $[T]$ is the transformation matrix from the corordinate system xyz to x'y'z'. $[T]$ consists of nine direction cosines, in which only three of them are independent because of the orthogonality conditions. For convenience in numerical calculation, $[T]$ matrix is described using Euler angles (ϕ,θ,ψ) which represent three counterclockwise rotations following the so-called x-convention definition (Landau and Lifschitz, 1976). If the Euler angles are given, the transformation matrix $[T]$ can be written as

$$[T] = \begin{bmatrix} c_\psi c_\phi - c_\theta s_\phi s_\psi & c_\psi s_\phi + c_\theta c_\phi c_\psi & s_\psi s_\theta \\ -s_\psi c_\phi - c_\theta s_\phi c_\psi & -s_\psi s_\phi + c_\theta c_\phi c_\psi & c_\psi s_\theta \\ s_\theta s_\phi & -s_\theta c_\phi & c_\theta \end{bmatrix} \qquad (95)$$

where c and s correspond to cosine and sine function, subscripts represent the arguments of such functions. The general ranges for Euler angles (ϕ,θ,ψ) are $[0,2\pi]$, $[0,\pi]$ and

$[0,2\pi]$, respectively. However, because we only calculate the stress amplitude along one direction, no difference is made if the direction is reversed. The Euler angle ranges can be reduced to $[0,\pi]$ for all three angle parameters (ϕ,θ,ψ). Furthermore, if we rotate the coordinate system along any original axis by $\pi/2$, the stress matrix components are same except in a different arrangement. During the calculation, we reduce the Euler angle ranges to $[0,\pi/2]$ for all three angle parameters (ϕ,θ,ψ) and search for all three direction stress amplitudes by angle increments of 2 degrees. The normal vector of maximum principal stress amplitude plane is named as 1'. On the plane perpendicular to 1', we search for the maximum shear stress amplitude by rotating the coordinate system about 1' axis by angle increments of 2 degrees. The vector of the maximum shear stress amplitude direction on the plane is named as 2'. 1', 2' and 3' (perpendicular to both 1', 2') can be treated as a new orthogonal coordinate system. (Fig. 23)

After obtaining the new O1'2'3' coordinate system, we can calculate the characteristic plane based on Table 2. For different materials, check the α value from Table 2. Rotate O1'2'3' about 3' axis by an angle of α degrees to be the new coordinate system O123 (Fig. 22). The plane O2'3' is the fatigue fracture plane and plane O23 is the characteristic plane.

Next we transform the stress history in the original OXYZ coordinate system to the new O123 coordinate system using Eqs. (94) and (95). Accounting for the stress on the characteristic plane and substituting into Eq. (93), we solve for the fatigue life N_f.

3.2.3 Finite element modeling and failure simulation

A railroad wheel is usually rigidly mounted on a steel shaft. Due to the high axle load and small contact area of the wheel/rail interface, the stresses at contact region are very high. To overcome the limitations of the traditional approaches for the wheel/rail contact problem, a 3D elasto-plastic finite element model is needed. After comparing several possible approaches, a simulation methodology for wheel/rail contact analysis is proposed in this paper. It has several advantages compared with previous analytical and numerical approaches. First, it is a realistic 3D finite element model and can accurately calculate the 3D stress response in the contact region. Next, it includes both material and geometric nonlinearity. It can be used to simulate large and complex wheel motions, such as rotation, sliding, hunting movement and even dynamic impact response. Finally, through sub-modeling techniques, the proposed model is made very efficient in computing and hardware requirements. Based the authors' experience, it can save up to 100 times the computational time for the current analysis compared with the 3D finite element model without using submodeling techniques, for the same level of accuracy.

For accurate contact analysis, geometry profiles of the rail head and the wheel tread are very important. Due to wear, the rail head profile and wheel tread profile will change overtime. For a relatively new wheel/rail, profiles from manufacturing can be used instead of field measurements. In order to show the methodology, wheel and rail sets are assumed to have the manufacturing profiles in the current study. All the finite element models are built using the commercial software ANSYS 7.0. The general procedure is described below.

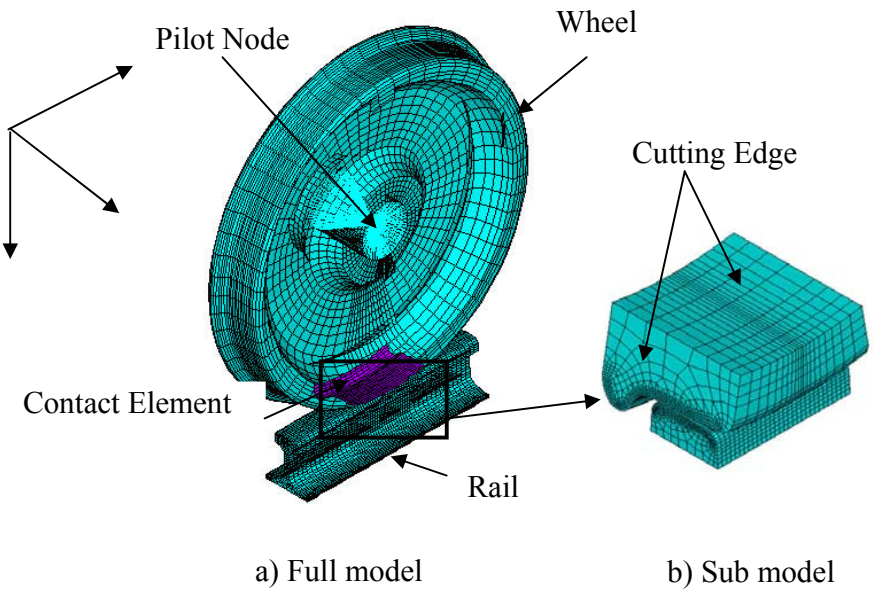

Fig. 24 Finite element modeling of wheel/rail contact

First, use the available profiles to build the geometry model of one wheel and a piece of rail. This model is called the full model. The rail length equals the length between two sleepers. Fixed boundary conditions are applied to the two ends of the rail. Different meshing is applied to the full model using 3D element (SOLID 45 in ANSYS). In the contact region, relatively finer mesh is used. At the wheel center, a pilot point is connected to the wheel using some rigid link elements. All the external loading and boundary conditions of the wheel are applied on the pilot point. These loading and boundary conditions can be obtained through field measurements or from numerical simulation of the track system motion analysis. On the possible contact areas of the railhead and the wheel tread, area contact elements (CONTACT 174 and TARGET 170 in ANSYS) are used corresponding to the geometry mesh of the wheel. The contact algorithm is augmented Lagrangian method (Ansys, 2003). Friction effect is included

into the material properties of the contact element. A Coulomb friction model is used in ANSYS. Friction coefficients can be calibrated using field measurement data. The material properties of the wheel and rail as described using a bilinear kinematic hardening model in ANSYS. No isotropic hardening is included in the current model. The finite element model is shown in Fig. 24.

Next, quasi-static analysis is performed for the full model and the results for each step are stored. Then the geometry model of the contact region is cut out to be a sub-model. The size of the sub-model depends on the analysis objective and also on the wheel motion simulated. The same types of elements as those in the full-model analysis are used to mesh the sub-model. Very fine mesh is applied to the contact area and to some depth under the contact surface. The results of the full-model are interpolated on the cutting edge of the sub-model corresponding to different calculation steps, and the interpolation results are applied as boundary conditions to the sub-model. In sub-modeling, the results from the sub-model need to be verified to make sure the cut boundaries are far enough from the stress concentration (contact region in this problem). The results in the sub-model are obtained using a fine mesh. They need not agree with the results from coarse-mesh global model. The disagreement can be caused not only by mesh refinement differences, but also due to geometric and material nonlinearities around the contact region. A detailed explanation can be found in ANSYS (2003). The cutting edge results from sub-model analysis are compared with those results in the full-model. If the difference is small enough, output the results in sub-model for future fatigue analysis. Otherwise, change the sub-model and repeat the previous steps. The flowchart of the finite element modeling is shown in Fig. 25.

The wheel profile is chosen according to the AAR standard (1998) wide flange contour. The wheel diameter is 0.838 meter (33 inches). The details of wheel tread surface geometry are shown in AAR standard M107/208. The vertical load is assumed to be the maximum design load, which is 146.2 KN (32,875 lb.). The material properties of the rail and wheel are assumed to be same (yielding strength = 500 MPa; Young's Modulus= 205 MPa; Friction coefficient = 0.25). The rail length is 600mm, which is normally the length between two sleepers (Telliskivi et al, 2000). In the current study, the initial contact point is assumed to occur at the railhead center and wheel tread center.

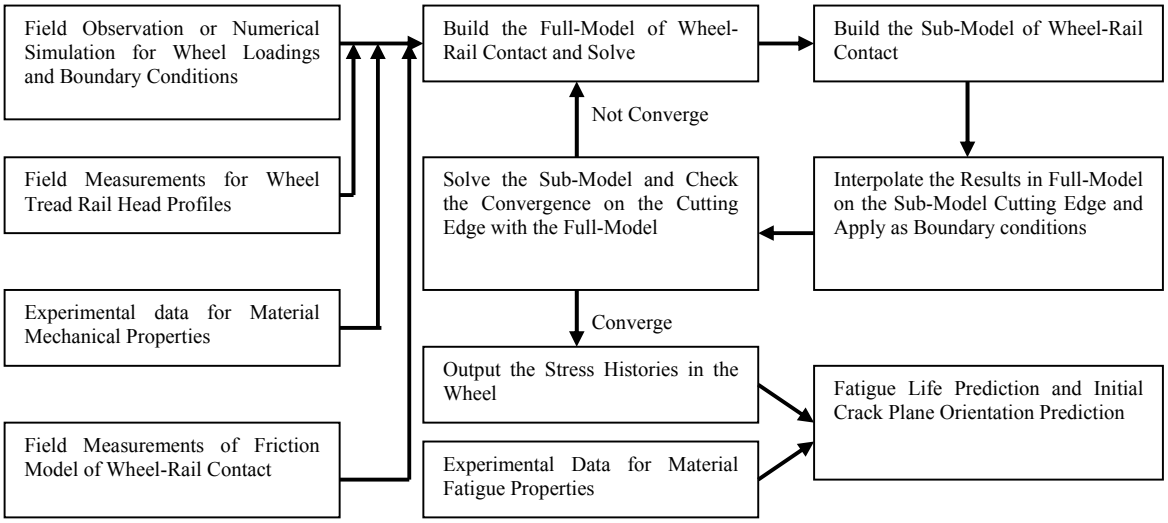

Fig. 25 Finite element modeling methodology

For 3D elasto-plastic contact analysis, it is usually very time-consuming, even using the submodeling techniques. It is shown that different constitutive relations will cause different stress response in the contact components (Bhargava et al, 1985; Hahn et al, 1987; Gupta et al, 1993; Howell et al, 1995), especially for ratcheting problem

(Ekberg and Kabo, 2004). Different constitutive models were used for rolling contact stress analysis, such as linear kinematic hardening model (Guo and Barkey, 2004; Gupta et al, 1993) or nonlinear kinematic hardening model (Ringsberg, 2001; Jiang and Sehitoglu, 1999). In the current study, linear kinematic hardening model is used. If only material nonlinearity is considered, the component reaches the steady state after the first cycle. However, since the geometry nonlinearity is also involved in the rolling contact problem, the component probably reaches the steady state after first several load cycles. Under fatigue cyclic loading, it is important to use the steady-state stress response within the mechanical components. It only requires a few rolling cycles to achieve the steady-state by moving the roller backward and forward in one cycle. Guo and Barkey (2004) assume that the stress states after six cycles represent the stabilized values for a 2D finite element model. In order to balance the computational effort and analysis accuracy for the current 3D finite element model, the stress responses after two cycles are assumed to be stabilized values and used for fatigue life prediction.

The static load analysis of the wheel/rail contact is performed first. The results of the sub-model are plotted in Fig. 26 and Fig. 27. Fig. 26 shows the Von Mises stresses from two different section views. Fig. 27 shows two in-plane shear stresses (τ_{xy} and τ_{yz}) from two different section-views. From the Fig. 26, it is found that the maximum Von Mises stress occurs at some depth below the tread surface. The stress decreases quickly as the depth increases. The high stress only occurs within a small region of the contact location. The stress in the other parts of the model is almost zero. This indicates that only a small portion of the motion simulation is needed because the stress far away from the contact location is zero.

From Fig. 27, a butterfly pattern of the shear stress τ_{yz} is observed. The maximum value also occurs at a depth of about 5 mm below the tread surface. Unlike the maximum Von Mises stress that occurs just above the contact location, the maximum τ_{xy} and τ_{yz} occur at the location some distance away from the contact location. From Fig. 26(a) and Fig. 27(a), the stress pattern indicates multiple contact points between the wheel/rail interfaces. The contact pressure and contact area on the wheel tread surface are plotted in Fig. 28. Two contact points are observed: one is near the center of the flat surface of the tread, and the other near the flange corner. This clearly shows that, the contact area near the flange corner is different from that predicted by the traditional Hertz theory, which is usually assumed to be an eclipse. Due to the non-Hertzian contact conditions, very high contact stress amplitude is obtained at this location. This conclusion is consistent with Telliskivi et al (2000).

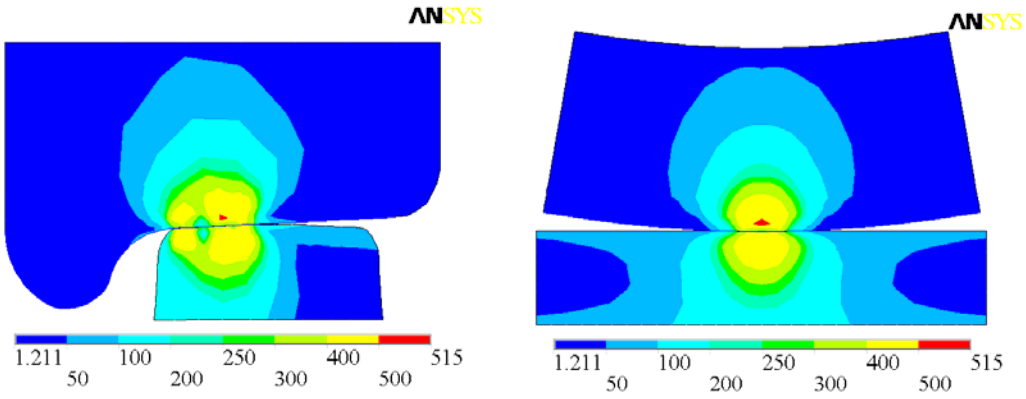

(a) Front Section View (a) Left Section View

Fig. 26 Von-Mises stress distribution of wheel/rail contact

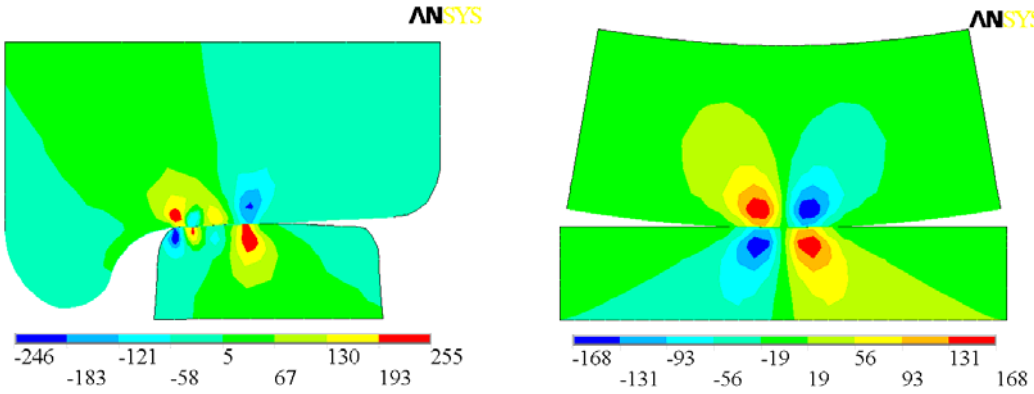

(a) Distribution of τ_{xy} (b) Distribution of τ_{yz}

Fig. 27 In-plane shear stress distribution of wheel/rail contact

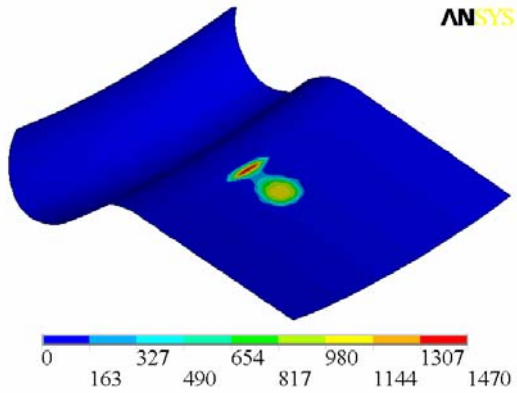

Fig. 28 Contact pressure distribution on the tread surface

After performing the static analysis, we simulate the wheel rotation on the rail, which is the normal motion mode of the wheel. This is done by applying the proper boundary conditions on the pilot node in the full model. Details about controlling the motion in contact analysis can be found in ANSYS (2003). The stress histories of two points (one is 3 mm below the tread surface, the other is 10 mm below the tread surface) during half a revolution of the wheel rotation are plotted in Fig. 29. The x-axis does not

indicate the real time and is the time step in FE analysis during the simulation of wheel rotating. Fig. 29 shows that the stress history in the wheel under rolling contact condition is not proportional, which indicates that the maximum normal stress and maximum shear stress do not occur simultaneously. The normal stress amplitude decreases from the depth of 3 mm to 10 mm. The FEA results only show very small residual stresses at these two locations. They can be barely seen in Fig. 29 and their effects are negligible in the current analysis.

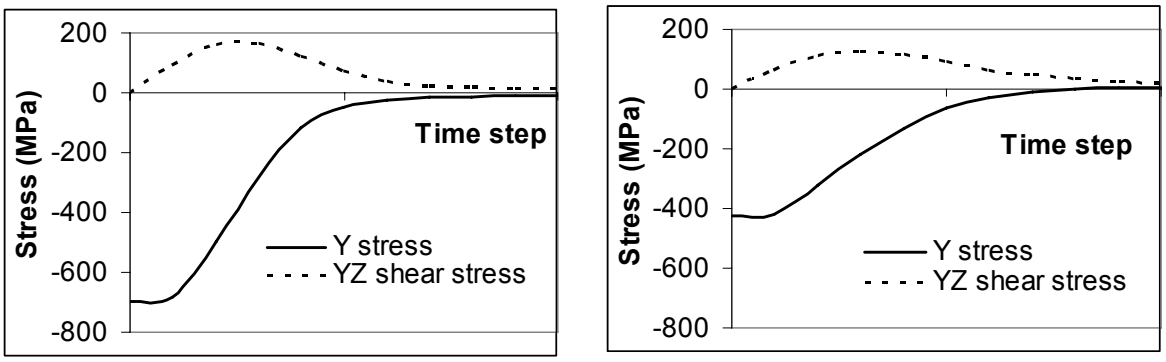

(a) Point 3mm below tread surface (b) Point 10 mm below tread surface

Fig. 29 Stress history at two locations in the wheel

After obtaining the stress history of the wheel, the proposed multiaxial fatigue criterion is used to calculate the fatigue initiation life and initial crack plane orientation. Because the critical location is not available, all the possible nodes on the radial section of the wheel are explored. The fatigue S-N curve for uniaxial and torsional loading are plotted in Fig. 30. In this, the S-N curve is used only to demonstrate the methodology. In the next chapter, material properties that represent the service conditions will be used for

reliability calculation. The fatigue damage distribution, initial crack plane orientation and field observation of one wheel failure are plotted together in Fig. 31. It needs to be pointed out that the current comparison is qualitative. Quantitative comparison will be shown in the next chapter.

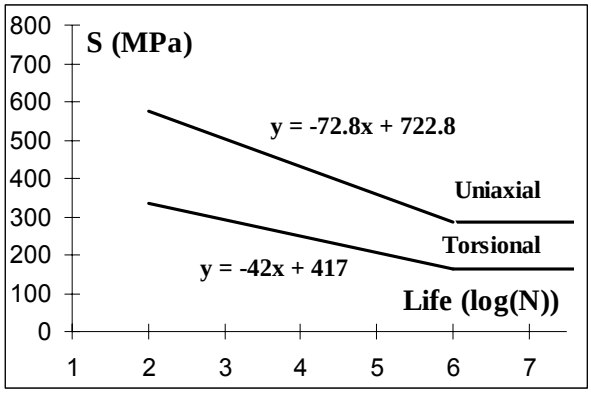

Fig. 30 S-N curve for uniaxial and torsional loading

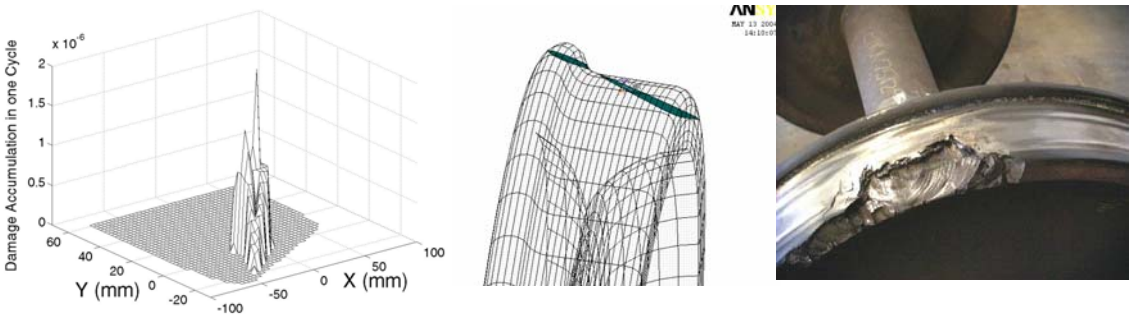

(a) Numerical prediction of damage distribution on the wheel section

(b) Numerical prediction of initial crack plane orientation

(c) Field observation of one wheel failure of shattered rim

Fig. 31 Numerical simulation and field observation of shattered rim failure of railroad wheels

Several conclusions can be drawn from both the numerical predictions and experimental observations. From the field observations, fatigue cracks usually initiate at a depth 5 mm~20 mm below the tread surface. The numerical crack initiation locations are obtained by checking each material point for the maximum damage. In the current analysis, it is the point 5 mm below the contact region. One possible reason that the current analysis predicts the lower value of the range is because no inclusions are considered. Ekberg (2002) observed that no inclusions were found in shattered rim failures upto 10 mm depth, and macroscopic inclusions were found in failures between 10 mm and 20 mm depth. The initial fatigue crack plane has a shallow angle with the wheel tread surface. In the current numerical example, it is about 20 degrees. Notice that the current analysis uses the constant loading for normal working conditions (maximum design loading for wheels) and does not include the effects of initial defects. Further study needs to include the variable loading and initial defects in the service condition.

3.2.4 Parametric study

In this section, the influence of several factors on the fatigue damage of the wheels is studied, using the finite element and multiaxial fatigue models developed in the previous section.

The diameter of the wheel will affect the fatigue damage. One simple explanation is that the radius of the wheel will affect the internal stress in the wheel according to the Hertz theory. However, for non-linear contact analysis and multiaxial fatigue analysis, the relationship between fatigue life and wheel diameter needs to be studied more carefully. A set of numerical simulations of wheels with different diameters, from 0.711 meter (28”) to 1.168 meter (46”) (AAR, 1998), are used. The vertical loading uses the

maximum design load for 0.838 meter (33") wheel (AAR, 1998). The damage accumulation rates (damage per cycle for constant amplitude loading) for different wheel size are plotted in Fig. 32.

From Fig. 32, it is seen that the damage accumulation rate and decreases as the wheel diameter increases. The effect is more significant for small size wheels (wheel diameter smaller than 0.838 meter). It is interesting to notice that for 0.914 meter (36") wheel, the damage accumulation rate exhibits a local increase. This phenomenon is also observed by Ekberg (2000) numerically.

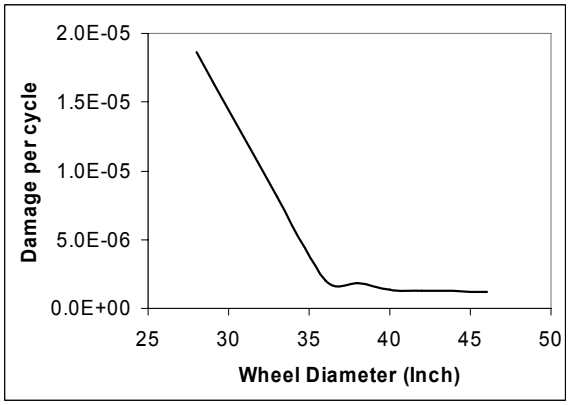

Fig. 32 Relationship between damage accumulation rate and wheel diameter

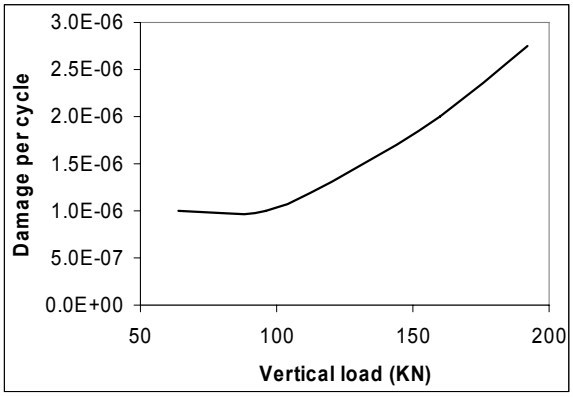

Fig. 33 Relationship between damage accumulation rate and vertical load

The damage accumulation rate on the wheel section for the 0.914 meter (36") wheel under different vertical loads (64 KN, 96 KN, 128 KN, 160 KN and 192 KN) are calculated and plotted in Fig. 3.33. As expected, the damage accumulation rate increases as the vertical load increases. In this case, the equivalent stress amplitude is lower than the endurance limit for the vertical load below 105 KN.

For the rolling contact problem, such as wheel/rail pair and gears, hardness is a very important material parameter; it directly affects the contact stiffness and thus the stress response in the wheel. AAR (1998) specifies the Brinell hardness requirements for wheel rims.

Hardness and strength are correlated to each other: strength increases as hardness increases. Isakov (2000) gives the empirical formulas for the relationship between hardness and ultimate strength for a variety of metals. Generally speaking, the relationship of hardness and strength also depends on different materials. Two sets of experimental data (Lovelace, 1971; Devine and Alber, 1982) for railroad wheels are collected and used to correlate the hardness with yield strength. The experimental data and linear regression are plotted in Fig. 34.

From Fig. 34, a positive linear relationship between hardness and yield strength is found. In the current study, different yield strengths are used in the finite element model for different hardness using the linear regression function shown in Fig. 34. Following the same procedure as in the previous section, the damage accumulation rate for different hardness materials are calculated and plotted in Fig. 35.

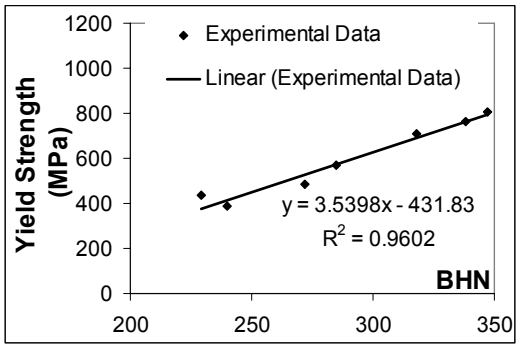

Fig. 34 Relationship between hardness and yield strength for wheel materials

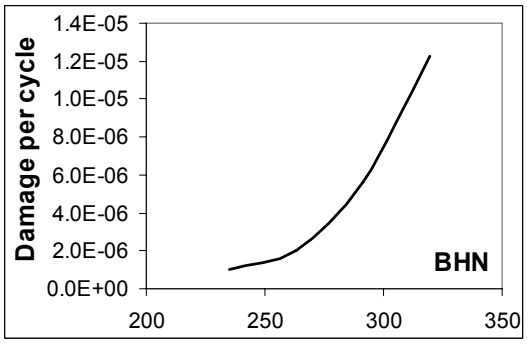

Fig. 35 Relationship between hardness and damage accumulation rate in wheels

From Fig. 35, it is seen that the damage accumulation rate increases as the hardness increases. This is because, for the material with higher hardness, the local plastic flow at the contact surface is not likely to occur and a smaller contact area between wheel and rail is obtained. A higher contact pressure is obtained for higher hardness material under the same vertical force. This leads to higher stress response in the railroad wheel. It should perhaps be noted that the same effect as for increased material hardness will occur if the material is subjected to isotropic hardening.

The effects of material endurance limit on the damage in railroad wheels are studied next. In the proposed multiaxial fatigue model, two material fatigue properties are used: the uniaxial fatigue strength and the ratio of torsional fatigue strength and uniaxial fatigue strength. The uniaxial fatigue strength effect is studied in this section first, followed by the ratio effect.

A 0.914 meter (36") railroad wheel under 160 KN vertical loading is used for the calculation. The fatigue S-N curve takes the same format as shown in Fig. 30. Five different numerical experiments using different fatigue endurance limits are explored. The damage accumulation rates for different fatigue endurance limits are plotted in Fig. 36.

From Fig. 36, the fatigue damage accumulation rate decreases as the material fatigue endurance increases as expected. In this case, no crack will be initiated if the fatigue endurance limit is higher than 340 MPa. The fatigue limits in the laboratory test data indicate the fatigue life around 10^7 cycles (about 20,000 service miles), which is below the usually fatigue life observed for railroad wheels. This is mainly due to two reasons. One is that the total life of the railroad wheel is the sum of the crack initiation

life and the crack propagation life. In this section, we only discuss fatigue crack "initiation life" and do not include fatigue crack "propagation life". A wheel reaching its initiation life does not always mean it fails. The other reason is that the laboratory test data are obtained under constant loading conditions. The railroad wheels are under spectrum loading. According to Union Pacific data, a large number of the loading cycles for the railroad wheels cause stresses are well below fatigue strength, which indicates that those loading cycles cause no damage to the wheels.

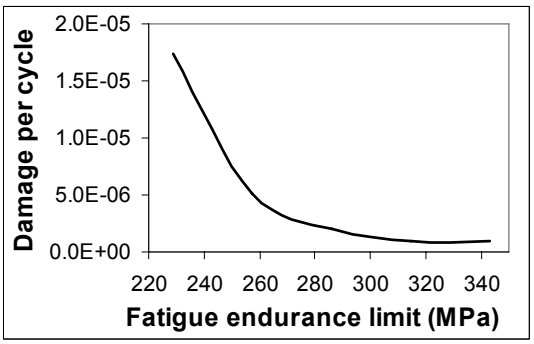

Fig. 36 Relationship between damage accumulation rate and fatigue endurance limit

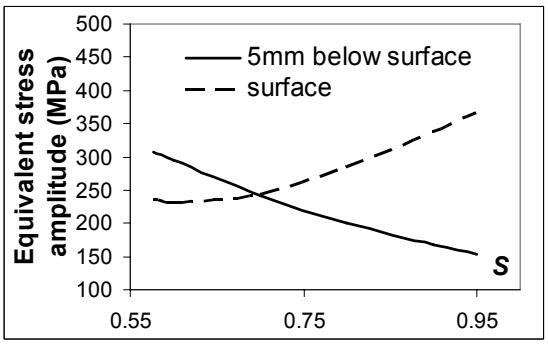

Fig. 37 Maximum equivalent stress amplitude for materials vs. strength ratio

In the proposed multiaxial fatigue model, the material parameter $s = t_{N_f} / f_{N_f}$ is important, and is the ratio between torsional fatigue strength and uniaxial fatigue strength. Several authors (Carpinteri A., Spagnoli, 2001; Papadopoulos, 1997) correlate this parameter with the material ductility. s increases as the material gets brittle. For the commonly used cast iron for railroad wheels, it falls into the range $1/\sqrt{3} \le s \le 1$.

A 0.914 meter (36") railroad wheel under 160 KN vertical loading is again used for the calculation. The maximum equivalent stress amplitudes for different values of s are computed and plotted in Fig. 37. It is interesting to find that not only the maximum

equivalent stress amplitude but also the critical location changes as s increases. The equivalent stress amplitudes at two different locations are plotted together. One location is 5mm below the tread surface, the other one is on the tread surface.

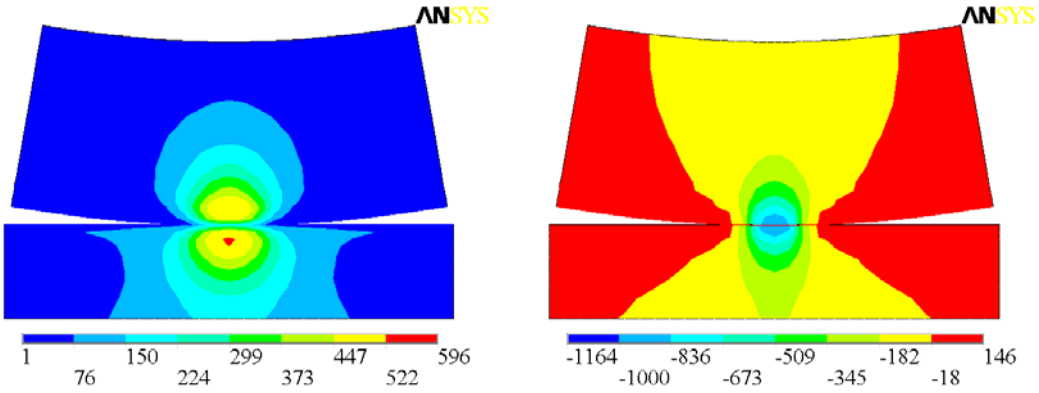

a) Maximum shear stress (Tresca stress) distribution

b) Normal stress distribution

Fig. 38 Tresca stress and normal stress distribution of wheel/rail contact

From Fig. 37, it shows different trend for the maximum equivalent stress amplitude corresponding to s. For smaller s, the crack is likely to initiate at subsurface. For larger s (more brittle material), the crack is likely to initiate from surface. A possible explanation is described below. The maximum shear stress (Tresca stress) and normal stress distribution are plotted in Fig. 38. Fig. 38 shows that the maximum normal stress and a smaller shear stress occur on the tread surface, and the maximum Tresca stress and a smaller normal stress occur at some depth below the tread surface. According to the proposed multiaxial fatigue model, the final fatigue damage is sum of the contributions by both normal stress and shear stress. For a ductile material, the characteristic plane is close to the maximum shear stress plane and is more likely to initiate at a location with

larger shear stress (some depth below the tread surface). For a brittle material, the characteristic plane is close to the maximum principal stress plane and is more likely to initiate at a location with larger normal stress (on the tread surface).

3.3 Crack propagation in railroad wheels

There are two major groups of models for the subsurface fatigue crack analysis under rolling contact loading. One is the group of fatigue crack initiation prediction models based on the S-N or e-N curve approach. This type of models has been discussed in the last section. The other is the group of fatigue crack propagation prediction models based on the fracture mechanics and is discussed below.

3.3.1 Previous work

Guagliano and Vergani (2005) proposed a semi-analytical approach for the analysis of internal cracks in wheels, in which the finite element method with the applied Hertz contact loading is used to calculate the stress intensity factors. Lansler and Kabo (2005) used a simplified 2D finite element model for the analysis of subsurface crack face displacements in railway wheels. Bogdański and Trajer (2005) used a simplified plane strain finite element model and the applied Hertz contact pressure for the analysis of stress intensity range in rolling contact fatigue. Glodež and Ren (1998) combined a simplified finite element analysis with applied Hertz contact pressure and a mixed-mode crack growth model based on strain energy release rate for the fatigue crack propagation analysis. Cho and Komvopoulos (1997) and Komvopoulos (1996) used a simplified finite element analysis with applied Hertz contact pressure and a mixed-mode crack propagation model based on the maximum shear stress intensity factor (mode II).

The proposed finite element computational methodology for the wheel/rail contact described in the last section is used to calculate the stress intensity factors. The crack propagation prediction of railroad wheels is predicted using the obtained stress intensity factors and the fundamental mixed-mode fatigue crack propagation model described in chapter 2..

Most of the available subsurface crack analyses are focused on the stress intensity calculations. Some of them use a simplified mixed-mode crack propagation model, such as the strain energy release rate model of Glode and Ren (1998). Feng et al (2006) observed different crack growth behavior under proportional and nonproportional loading paths with identical loading magnitude and stated that the models based on the strain energy release rate cannot represent this trend. Traditionally, the models for mixed-mode crack propagation are developed and validated using proportional loading, i.e. a plate with inclined crack under remote uniaxial loading. In the later part of this section, it is shown that the subsurface crack stress intensity factor histories are nonproportional under rolling contact condition. A mixed-mode crack propagation model, which can consider the effect of loading non-proportionality, is required for the crack propagation and fatigue life prediction for railroad wheels.

A general methodology for subsurface fatigue crack propagation analysis for railroad wheels is proposed in this section. It combines a 3D finite element model for the wheel/rail contact and a mixed-mode crack propagation model developed in Chapter 2. Parametric studies are performed using the proposed methodology for different vertical loadings, wheel diameters, crack geometries and crack surface friction coefficients.

3.3.2 Finite element modeling and crack propagation simulation

Following the description of the finite element modeling for crack initiation simulation, the same full model for wheel/rail contact analysis is used. A sub-model with an embedded crack is built. The results of the full-model are interpolated on the cutting edge of the sub-model corresponding to different calculation steps, and the interpolation results are applied as boundary conditions to the sub-model.

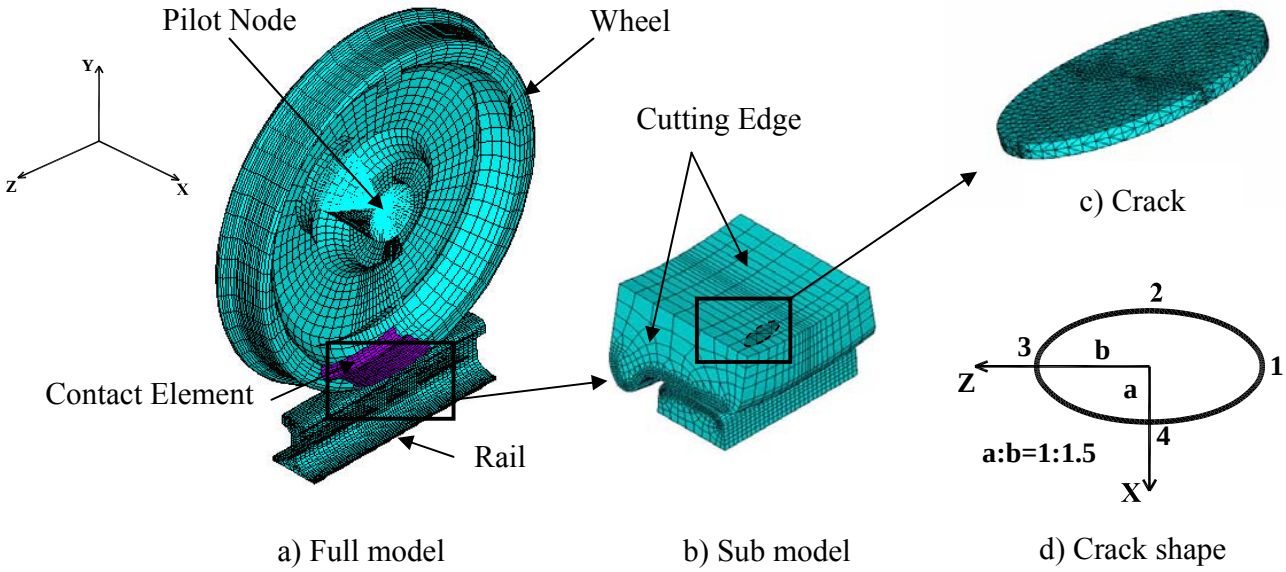

Fig. 39 Finite element modeling of wheel/rail contact with subsurface crack

An elliptical crack is built into the sub-model. The crack location and orientation are determined from the previous numerical prediction of the initial fatigue crack profile (Section 3.2.3), which is consistent with the field observation of subsurface crack in railroad wheels. The major axis is along the track direction and the minor axis is perpendicular to the track direction. Based on the field observations of the initial fatigue

crack profile, the aspect ratio of the elliptical crack is assumed to be 1.5. The subsurface crack is modeled as two contact surfaces to make sure that the two crack surfaces do not penetrate each other. On the crack surfaces, area contact elements (CONTACT 174 and TARGET 170 in ANSYS) are used. Friction effect is also included between the two crack surfaces. A very fine mesh (the average element length is about 0.1 mm) is applied near the crack region. The finite element models of the full model, sub-model and crack are shown in Fig. 39.

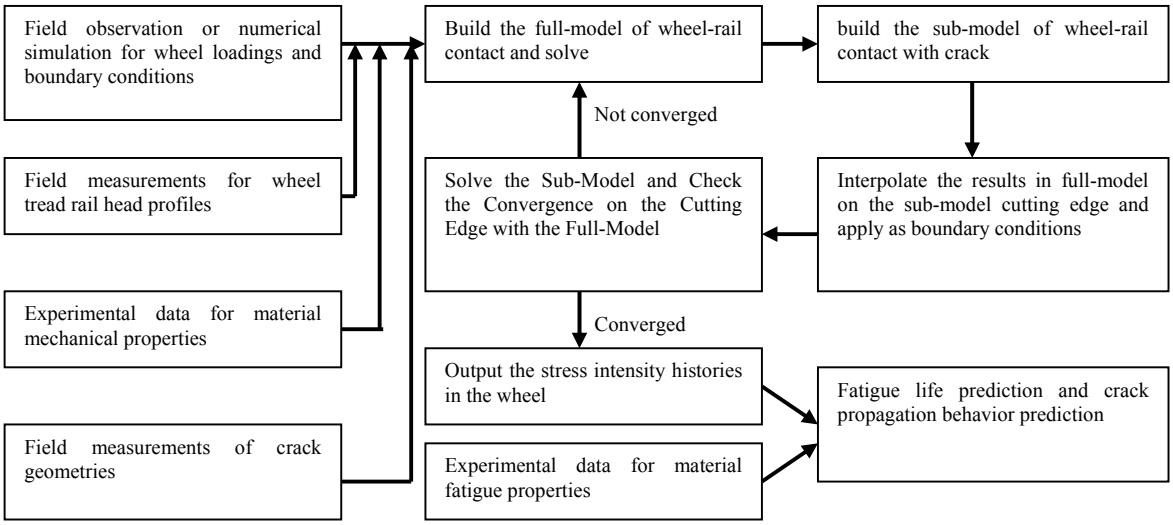

Fig. 40 Finite element modeling methodology with subsurface crack

In sub-modeling, the results from the sub-model need to be verified to make sure the cut boundaries are far enough from the stress concentrations (contact region and crack tip in this problem). The results in the sub-model are obtained using a fine mesh. They need not agree with the results from the coarse-mesh global model. The disagreement can be caused not only by mesh refinement differences, but also due to geometric and

material nonlinearities around the contact region. A detailed explanation can be found in ANSYS (2003). The cutting edge results from sub-model analysis are compared with the results of the full-model. If the difference is small enough, output the results in sub-model for future fatigue analysis. Otherwise, change the sub-model and repeat the previous steps. The flowchart of the finite element modeling is shown in Fig. 40.

The wheel profile is chosen according to the AAR standard (1998) wide flange contour. The wheel diameter is 0.914 meter (36 inches). The subsurface crack is assumed to be located locate 6 mm below the tread surface, with an inclined angle of 20 degrees with respect to the tread surface. The semi-minor axis is 5 mm. In the current study, the initial contact point is assumed to occur at the railhead center and wheel tread center.

The static load analysis of the wheel/rail contact is performed first. The results of the sub-model are plotted in Fig. 41 and Fig. 42. Fig. 41 shows the Von Mises stresses from two different section views. Fig. 42 shows two in-plane shear stresses (τ_{xy} and τ_{yz}) from two different section-views. From the Fig. 41, it is found that the maximum Von Mises stress occurs at some depth below the tread surface. The stress decreases quickly as the depth increases. The maximum Von Mises stress also occurs around the crack tip, which is caused by the stress singularity near the crack tip. The high stress only occurs within a small region of the contact location. The stress in the other parts of the model is almost zero. This indicates that only a small portion of the motion simulation is needed because the stress far away from the contact location is zero.

From Fig. 42, a butterfly pattern of the shear stress τ_{yz} is observed. The maximum value also occurs at the crack tip. From Fig. 41(a) and Fig. 42(a), the stress pattern indicates multiple contact points between the wheel/rail interfaces. The contact

pressure and contact area on the wheel tread surface are plotted in Fig. 43. Two contact points are observed: one is near the center of the flat surface of the tread, and the other near the flange corner. This clearly shows that, the contact area near the flange corner is different from that predicted by the traditional Hertz theory, which is usually assumed to be an ellipse.

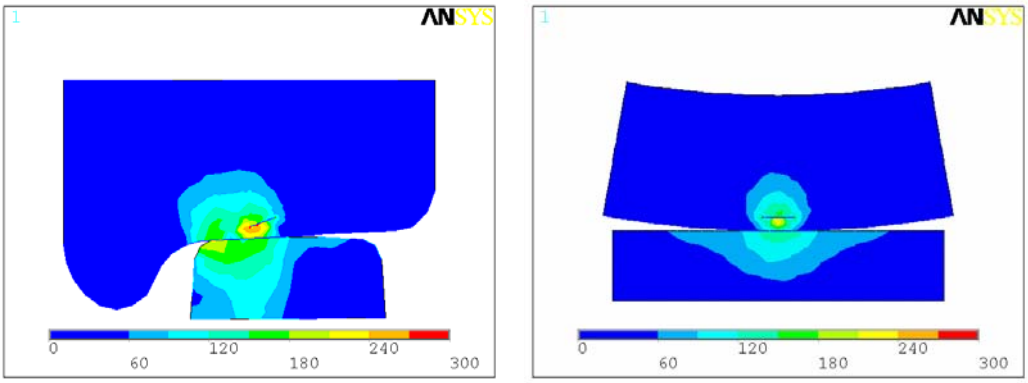

(a) Front Section View (a) Left Section View

Fig. 41 Von-Mises stress distribution of wheel/rail contact with subsurface crack

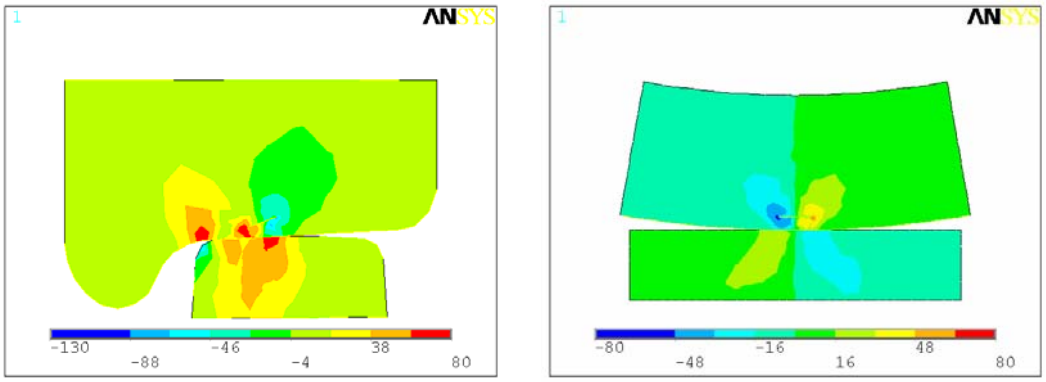

(a) Distribution of τ_{xy} (b) Distribution of τ_{yz}

Fig. 42 In-plane shear stress distribution of wheel/rail contact with subsurface crack

After performing the static analysis, we simulate the wheel rotation on the rail, which is the normal motion mode of the wheel. This is done by applying the proper boundary conditions on the pilot node in the full model. Details about controlling the motion in contact analysis can be found in section 3.2.3.

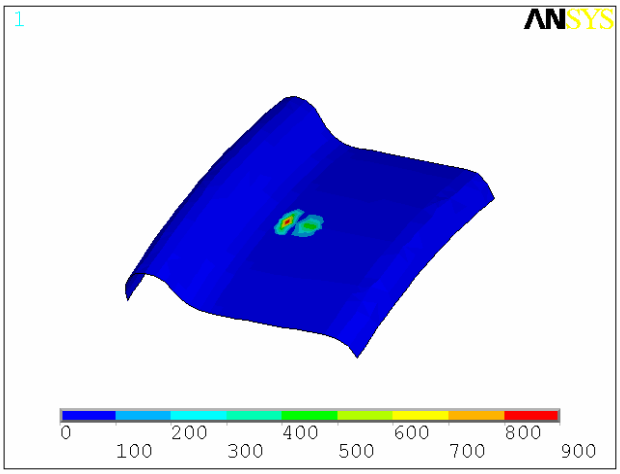

Fig. 43 Stress distribution of contact area

After performing the static analysis, we simulate the wheel rotation on the rail, which is the normal motion mode of the wheel. This is done by applying the proper boundary conditions on the pilot node in the full model. Details about controlling the motion in contact analysis can be found in Liu et al (2006).

The current study focuses on the subsurface crack behavior under rolling contact loading. The crack deformation behavior is studied first. A relative displacement between is defined same as Lansler and Kabo (2005).

$$u_{rel}(I,II,III) = u_{upper}(I,II,III) - u_{lower}(I,II,III) \qquad (96)$$

where u_{rel} is the relative displacement between the upper crack surface and the lower crack surface. u_{upper} and u_{lower} are the absolute displacement of the upper and lower crack surface, respectively. (I, II, III) indicates the three modes of crack deformation, i.e. Mode I, Mode II and Mode III, respectively.

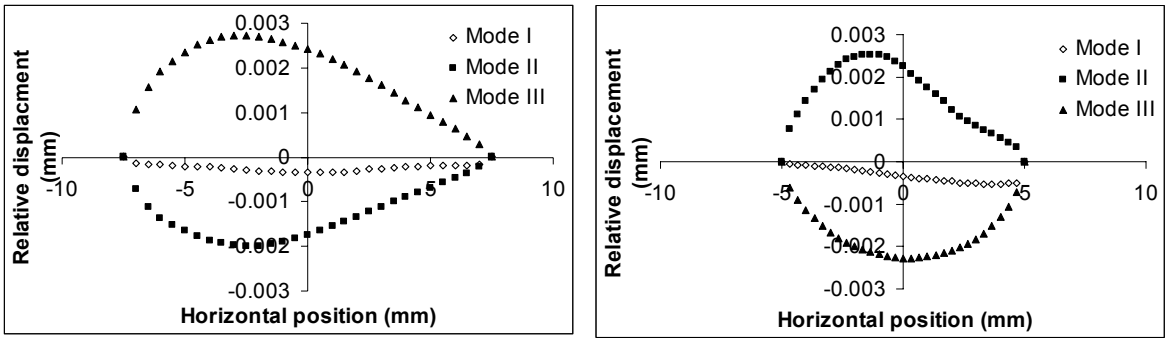

(a) Major axis (b) Minor axis

Fig. 44 Relative crack surface displacement

The maximum relative displacements along the major and minor axis are plotted in Fig. 44. Due to the possible non-proportionality of the stress intensity histories in the three modes, those maximum values may not occur simultaneously. Fig. 44 shows that both mode II and III components are significant and must be included into the fatigue crack propagation analysis. During the rolling contact, the crack surfaces are closed and no opening displacement for the mode I component exists. The negative sign of mode I displacement in Fig. 44 is due the small penetration of the contact element in the numerical calculation and cannot occur in realistic situation. Compared with the larger mode II and mode III displacements, mode I displacement is small and its effect is ignored in the current study.

The mode II and III stress intensity histories (SIF) of two crack tips at the major axis and the minor axis (points 1 and 2 in Fig. 39(d)) during half a revolution of the wheel rotation are plotted in Fig. 45. The *x*-axis does not indicate the real time and is the time step in FE analysis during the simulation of wheel rotating. Fig. 45 shows that the SIF in the wheel under rolling contact condition is not proportional, which indicates that the maximum mode II and mode III SIF do not occur simultaneously. The FEA results only show very small residual stresses at these two locations (nonzero SIF values at the end of the calculation). The residual stresses are small and their effects are negligible in the current analysis.

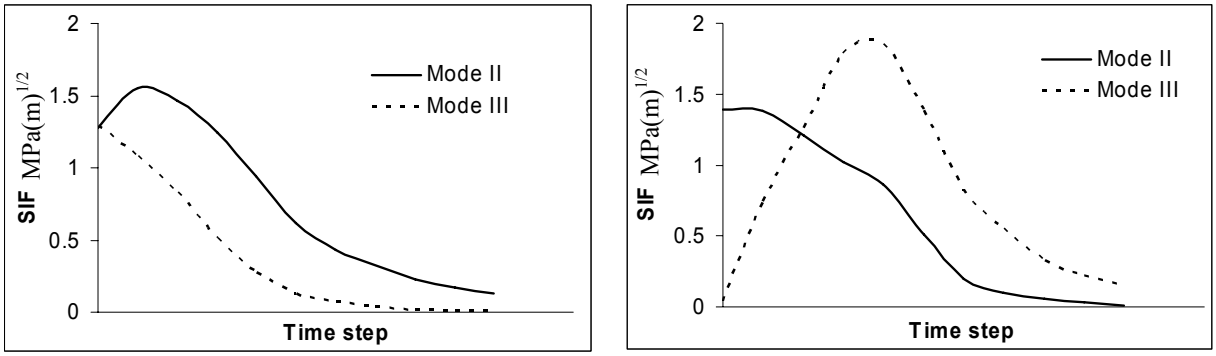

(a) Crack tip at the major axis (b) Crack tip and the minor axis

Fig. 45 Stress intensity factor history under rolling contact

After obtaining the stress intensity factor histories of the wheel, the proposed multiaxial fatigue crack propagation model is used to calculate the fatigue crack propagation life and crack propagation profile. Several different models with different crack size are analyzed (as shown in the next section of parametric study) and the

relationship between the crack size and the stress intensity factor are used for fatigue life prediction. The uniaxial fatigue crack propagation curve is reported by Kuna et al (2005) for a ductile wheel iron and is plotted in Fig. 46. The pure torsional fatigue crack propagation curve is not reported. We assume the ratio of s as 0.6, which is typically for ductile metals (Liu and Mahadevan, 2005(a)).The stress ratio effect is included in the crack propagation using the well-known Walker (1970) model. The general crack propagation function is expressed as

$$\frac{da}{dN} = C\left(\frac{\Delta K_{eff}}{(1-R)^{\gamma}}\right)^{m} \qquad (97)$$

where $\frac{da}{dN}$ is the crack growth rate. ΔK_{eff} is the effective stress intensity range for mixed-mode loading. For uniaxial fatigue loading, it equals mode I stress intensity factor. R is the stress ratio. C, m and γ are material parameters. Eq. (97) and experimental results are plotted together in Fig. 46.

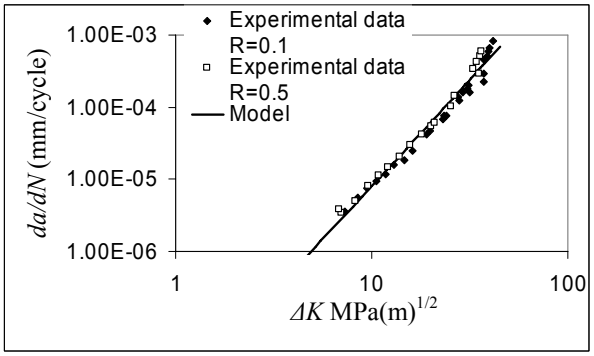

Fig. 46 Fatigue crack growth rate curve and experimental data

The effective mixed-mode stress intensity factor can be expressed as a function of applied loading and crack length as

$$\Delta K_{eff} = \Delta F \sqrt{\pi a} Y(a) \quad (98)$$

where ΔF is the applied vertical loading range. $Y(a)$ is a geometry function considering the effect of crack configuration and boundary conditions, which is calibrated using the finite element results. Substituting Eq. (98) into Eq. (97) and solve for fatigue life

$$N(a) = \frac{1}{C(\Delta F)^m} \int_{a_0}^{a} \frac{(1-R)^m da}{(\sqrt{\pi a} Y(a))^m} \quad (99)$$

where $N(a)$ is the number of cycle to growth a crack from the initial length a_0 to the length of a.

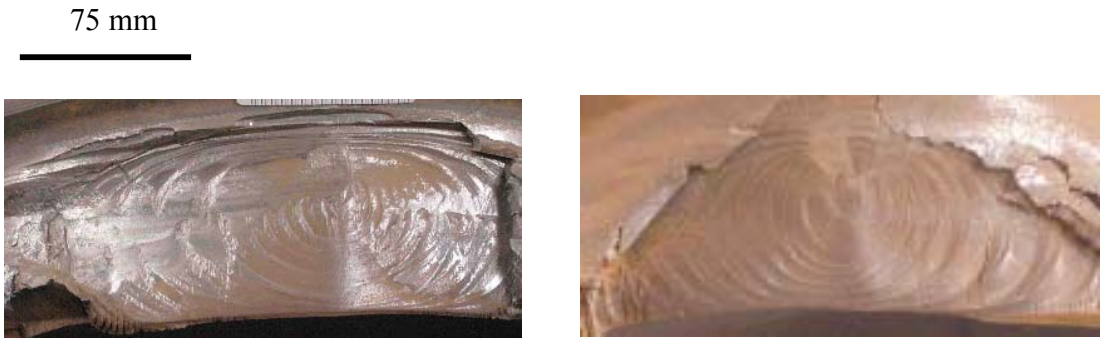

a) Field observations of crack shape

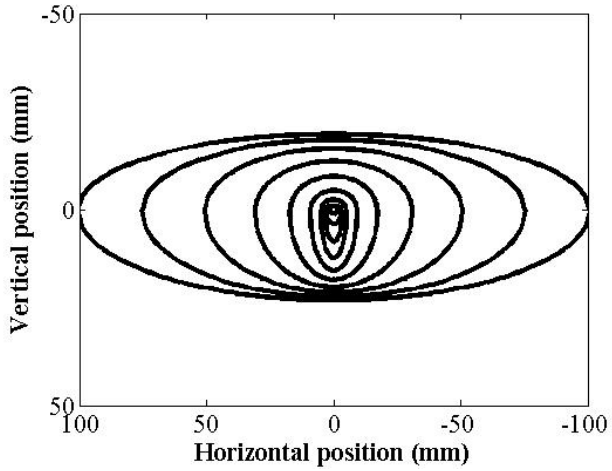

b) Numerical prediction of crack shape

Fig. 47 Crack shape comparison between numerical prediction and field observation

In the current study, the crack shape is assumed to be controlled by the four points on the crack front (points 1-4 in Fig. 39(d)). The crack front profile is approximated using an elliptical curve. The crack growths along the major and the minor axis are calculated using the proposed method. The crack front contours at the different number of cycle are plotted in Fig. 47. The increment of the number of cycles between each contour is $1.5x10^6$. A couple of field observations of the crack are also plotted for comparison. Notice that the current analysis uses the constant maximum design loading for wheels and the current comparison is only qualitative. Quantitative comparison of fatigue lives needs extensive experimental and site data, such as loading spectra and failure crack lengths.

It is seen that the numerical prediction of the crack shape agrees very well with the field observation. The early stage crack propagation is in a circular configuration, which shows almost equal crack propagation rate in both the minor and major axis direction. Then the crack propagates in an elliptical manner, which is mainly along the major axis direction (track direction). Both numerical prediction and field observations show a compressed contour in the minor axis direction and extruded contour in the major axis direction.

3.3.3 Parametric study

In this section, the influence of several factors on the fatigue damage of the wheels is studied, using the finite element and multiaxial fatigue models developed in the previous sections.

The diameter of the wheel will affect the fatigue damage. One simple explanation is that the radius of the wheel will affect the internal stress in the wheel according to the

Hertz theory. However, for non-linear contact analysis and multiaxial fatigue analysis, the relationship between fatigue life and wheel diameter needs to be studied more carefully. A set of numerical simulations of wheels with different diameters, from 0.711 meter (28") to 0.965 meter (38") (AAR, 1998), are used. The vertical loading uses the maximum design load for 0.914 meter (36") wheel (AAR, 1998). The equivalent mixed-mode stress intensity factors for different wheel size are plotted in Fig. 48. From Fig. 48, it is seen that the equivalent mixed-mode stress intensity factor decreases as the wheel diameter increases. It is interesting to notice that for 0.914 meter (36") wheel, the mixed-mode SIF exhibits local maxima, which indicates larger fatigue damage for this type of wheel. This phenomenon is also observed in section 3.2.3 and Ekberg (2000) using the classical S-N curve fatigue analysis.

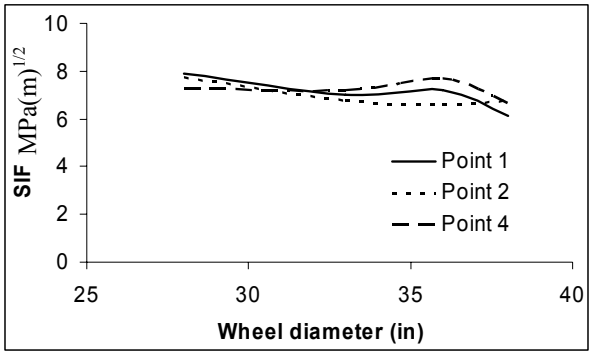

Fig. 48 Wheel diameter effect on the SIF

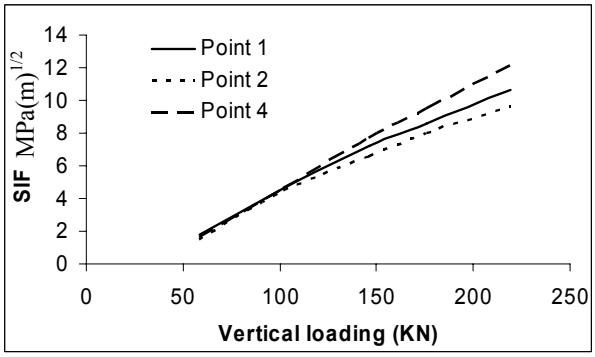

Fig. 49 Loading effect on the SIF

The equivalent SIF for the 0.914 meter (36") wheel under different vertical loads (58.5 KN, 102.3 KN, 146.2 KN, 175.4 KN and 219.3 KN) are calculated and plotted in

Fig. 49. The equivalent increases as the vertical load increases almost linearly. For different points at the crack front, the slopes change slightly.

The effects of different crack lengths are plotted in Fig. 50. A 0.914 meter (36") railroad wheel under 146.2 KN vertical loading with different semi-minor axis length (1 mm, 3 mm, 5mm, 10 mm and 15 mm) are calculated. Different behaviors are observed for the SIF at the major axis and at the minor axis.

For the point at the major axis (point 1 in Fig. 39(d)), the SIF increases as the crack length increases. For relative short cracks, the increase is significant. For long cracks, the increase is small. The reason is that the high stress only occurs within a small region near the contact location. The stress in the other parts of the wheel is almost zero at a certain time instant. When the crack is long enough to exceed the stressed region, the crack beyond the stressed region has little effect on the stress field around the crack tip and the SIF. The long crack experience almost same SIF range during one evolution of the wheel.

For the point at the minor axis (point 2 and 4 in Fig. 39(d)), the SIF does not change monotonically as the crack length increases. For short cracks, the SIF increases as the crack length increase. For long cracks, the SIF decreases as the crack length increases. The reason is that long cracks exceed the stressed region near contact location and the crack tip experiences less stress compared with the case that the crack tip is within the stressed region. This is the reason the crack contour is compressed along the minor axis in Fig. 3.47.

A 0.914 meter (36") railroad wheel under 146.2 KN vertical loading with different crack orientations (0 degree, 10 degree, 20 degree and 30 degree) is used for the

calculation. The SIF of different crack orientations are plotted in Fig. 51. From Fig. 51, the SIF changes slightly with respect to the crack orientation. For points 1 and 4, the SIF experience a local maxima between 20~30 degree. This possibly explains why the crack observed in field shows a similar orientation about 20 degree to the tread surface.

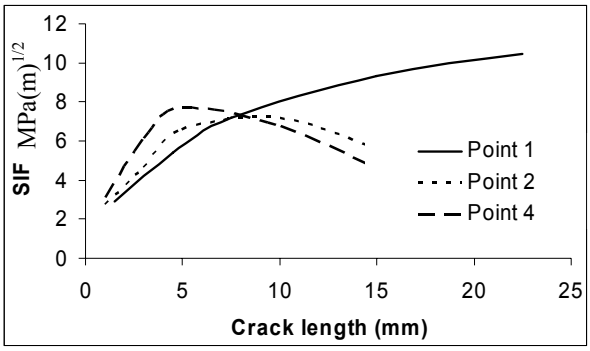

Fig. 50 Crack length effect on the stress intensity factor

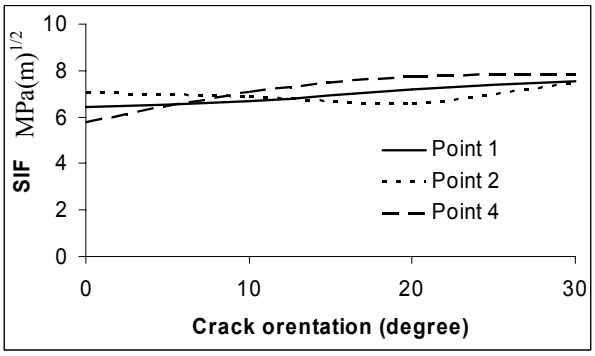

Fig. 51 Crack orientation effect on the stress intensity factor

A 0.914 meter (36") railroad wheel under 146.2 KN vertical loading with different crack depths (3 mm, 4 mm, 5 mm, 6 mm, 7 mm and 8 mm below the tread surface) is used for the calculation. The SIF of different crack depths are plotted in Fig. 52. From Fig. 52, the SIF does not change monotonically with respect to different crack depths. The SIF experiences local maxima around a depth of about 6~7 mm. This possibly explains why the crack observed in the field shows a similar depth about 5~10 mm below the tread surface.

A 0.914 meter (36") railroad wheel under 146.2 KN vertical loading with different crack surface friction coefficients (0, 0.1, 0.2, 0.3, 0.4 and 0.5) is used for the calculation. The SIF of different crack surface friction coefficients are plotted in Fig. 53.

From Fig. 53, the crack surface friction coefficient has little effect on the SIF and its effect can be ignored in the current study.

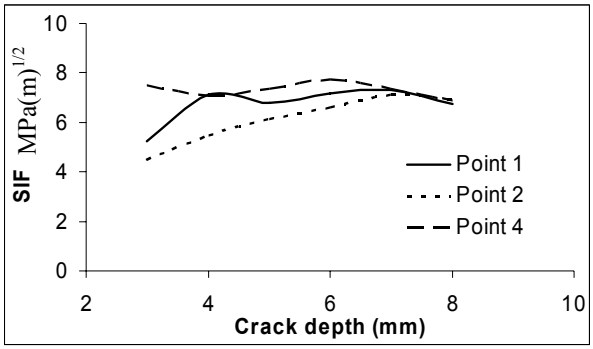

Fig. 52 Crack depth effect on the stress intensity factor

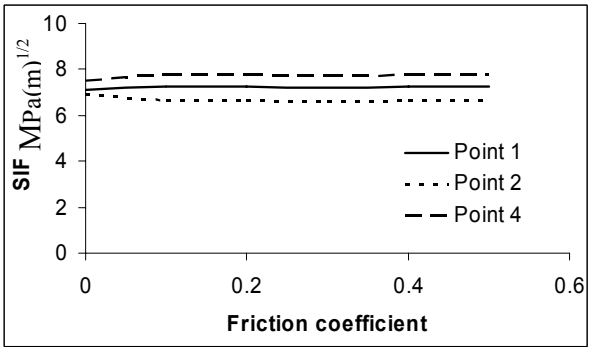

Fig. 53 Crack surface friction coefficient effect on the stress intensity factor

3.4 Summary

A multiaxial fatigue crack initiation and propagation propagation life prediction model is developed in this chapter, which is based on the multiaxial fatigue theory and mixed-mode crack propagation model developed in Chapter 2.

The new multiaxial fatigue model is applied to the fatigue life prediction of wheel/rail contact problem. Non-linear finite element analysis is used for stress and stress intensity factor computation and a submodeling technique is used to improve the efficiency and accuracy. The stress and stress intensity factor history is then used to calculate the fatigue life. A numerical example is implemented and compared with field observation of failure pattern. The effect of several parameters, namely wheel diameter, material properties, vertical loads, crack length, crack orientation, crack depth and crack surface friction, on the equivalent damage and stress intensity in railroad wheels are studied using the proposed model.

In the current study, the effects of different parameters have been studied individually. Future research needs to consider interactive effects of those parameters because the wheel/rail contact problem is highly nonlinear. For example, what is the variation of the equivalent stress intensity factor if both crack depth and vertical loading change? Extensive experimental data is needed to validate such interaction models. Also, other effects, such as residual stress from manufacturing, brake loading, thermal loading, dynamic and impact loadings, material defects, etc, need to be included in the proposed methodology.

CHAPTER IV

STOCHASTIC FATIGUE MODELING AND RELIABILITY

4.1 Overview

In Chapters II and III, a general deterministic methodology for multiaxial fatigue analysis has been developed and applied to the wheel/rail rolling contact problem. However, due to the large scatter observed in field and experimental data, it is more appropriate to include the variability in assessing the reliability of the railroad wheels.

In this chapter, the previous deterministic analysis methodology is extended to probabilistic analysis. An efficient statistical design of experiments technique is used to reduce the computational cost, and a response surface is developed based on the numerical experiments. A simulation based methodology for reliability calculation is proposed.

The reliability analysis of railroad wheels is a time-dependent reliability problem. The fatigue damage caused within the wheel varies with location and time, and is deemed as a random field/process. Stochastic field/process expansion techniques are applied for increased accuracy in describing the random damage field/process. Due to the modular nature of the proposed method, the analyst could choose classical statistical analysis if the prediction accuracy is acceptable or the experimental data is not sufficient.

The methodology used for railroad wheel reliability analysis in this chapter is organized as follows:

The stochastic fatigue damage accumulation process under variable amplitude loading and spectrum loading is studied first. A non-linear damage accumulation rule is proposed. Uncertainty modeling of material properties and applied loading is explored to describe the randomness observed in service based on the experimental data from laboratory.

The multiaxial fatigue damage accumulation process is numerically simulated using deterministic analysis techniques (finite element and fatigue damage analysis). This work has been done in Chapters II and III.

A response surface method (RSM) combined with design of experiments (DOE) is used to obtain a simplified empirical formula for the damage accumulation process considering several sources of variation.

Time-dependent failure probability is evaluated, where the failure is defined to occur when the accumulated damage exceeds an acceptable value or the crack exceeds a critical value. A Monte Carlo simulation method is used to calculate the probabilistic life distribution.

Experimental and field data are collected and analyzed. The information is used to calibrate and validate the proposed methodology.

4.2 Stochastic fatigue damage accumulation

The fatigue process of mechanical components under service loading is stochastic in nature. Life prediction and reliability evaluation is still a challenging problem despite extensive progress made in the past decades. A comprehensive review of early developments can be found in Yao et al (1986).

Compared to fatigue under constant amplitude loading, the fatigue modeling under variable amplitude loading becomes more complex both from deterministic and probabilistic points of view. An accurate deterministic damage accumulation rule is required first, since the frequently used linear Palmgren-Miner's rule may not be sufficient to describe the physics (Fatemi and Yang, 1997). Second, an appropriate uncertainty modeling technique is required to include the stochasticity in both material properties and external loadings, which should accurately represent the randomness of the input variables and their covariance structures. In addition to the above difficulties, such a model should also be computationally and experimentally inexpensive. The last characteristic is the main reason for the popularity of simpler models despite their inadequacies.

In this section, a general methodology for stochastic fatigue life prediction under variable loadings is proposed, which combines a nonlinear fatigue damage accumulation rule and uncertainty modeling methods for material properties and applied loading. A brief review of fatigue damage accumulation rule is given first and a simple nonlinear damage accumulation model is proposed. Next, the uncertainty modeling is discussed and a stochastic S-N curve approach using the Karhunen-Loeve expansion technique is proposed to represent the covariance behavior observed in the experimental data. A rain-flow counting technique together with a random loading generation method is used to represent the uncertainty observed in the applied loading. The numerically generated material properties and applied loading are used in the Monte Carlo simulation to calculate the fatigue life distribution of mechanical components. A wide range of experimental data is explored to validate the proposed methodology. The probabilistic

fatigue life predictions of the numerical model are compared with those from experimental data under variable loadings.

The proposed model offers several advantages over existing approaches. It uses a nonlinear fatigue damage accumulation rule, which improves the accuracy of the Miner's rule by considering the load dependence effect of the fatigue damage. Unlike most of the previous nonlinear fatigue damage accumulation models, the proposed model does not require cycle-by-cycle calculation and can directly use the cycle counting results from the loading history, which significantly reduces the calculation effort, especially for the reliability evaluation. A stochastic S-N curve approach can capture the covariance structure of the fatigue damage process under different stress levels (which is usually ignored by other models), and thus makes the reliability evaluation more accurate compared to the available models.

4.2.1 Damage accumulation rule

Fatigue damage increases with applied loading cycles in both constant loading and variable loading. However, the characteristics of damage accumulation under different loadings are different. For more than eighty years, researchers have tried to find the best rule to describe the fatigue damage accumulation behavior. A comprehensive review is not the objective of this paper and can be found in Fatemi and Yang (1998). Only a few damage accumulation rules are briefly described below.

Among all the fatigue damage accumulation rules, the LDR (linear damage accumulation rule), also known as Palmgren-Miner's rule, is probably the most commonly used. Miner (1945) expressed the fatigue damage accumulation under variable loadings as

$$D = \sum_{i=1}^{k} \frac{n_i}{N_i} \qquad (100)$$

where D is the fatigue damage of the material, n_i is the number of applied loading cycles corresponding to the ith load level, N_i is the number of cycles to failure at the ith load level, from constant amplitude experiments. Eq. (100) implies that fatigue damage accumulates is in a linear manner.

If LDR is used for fatigue life prediction, it is usually assumed that the material fails when the damage D reaches unity. However, it has been shown that LDR produces a large scatter in the fatigue life prediction of both metal and composites (Shimokawa and Tanaka, 1980; Kawai and Hachinohe, 2002). Also, LDR cannot explain the load level dependence of fatigue damage observed in the experiments (Halford, 1997). Despite all those deficiencies, LDR is still frequently used due to its simplicity.

In order to improve the accuracy of LDR, nonlinear functions have been proposed to describe the damage accumulation. Marco and Starkey (1954) expressed the damage accumulation function as

$$D = \sum_{i=1}^{k} \left(\frac{n_i}{N_i}\right)^{C_i} \qquad (101)$$

where C_i is a material parameter related to ith loading level. A similar formula named damage curve approach has been proposed by Manson and Halford (1981). Eq. (101) can reflect the load-level dependence and load-sequence dependence effects of the fatigue damage accumulation. It is shown that the Miner's sum $\sum_{i=1}^{k} \frac{n_i}{N_i} > 1$ for low-high load sequences and $\sum_{i=1}^{k} \frac{n_i}{N_i} < 1$ for high-low sequence (Fatemi and Yang, 1998). As pointed

out by Van Paepegem and Degrieck (2002), this conclusion cannot be applied to all materials in the existing experimental data base in the literature.

Due to the nonlinearity of Eq. (101), the fatigue damage under service loading needs to be computed in a cycle-by-cycle manner, which requires a large amount of computational effort. This disadvantage can be circumvented by approximating the nonlinear function by double linear functions (Halford, 1997). In each stage, a linear damage accumulation rule is applied. For two-block loading, the double linear damage model is easy to implement. For the multi-block loading or spectrum loading, the determination of the parameters in the model becomes complicated (Halford, 1997, Goodin et al, 2004).

Several more complex fatigue damage accumulation functions have been proposed for increased accuracy. Halford and Manson (1985) proposed a double damage curve approach, which combines the accurate parts of both the double linear damage approach and the damage curve approach. A similar result was obtained by using the fatigue crack growth concept (Vasek and Polak, 1991). A more recent approach for fatigue damage accumulation is to use a nonlinear continuum damage mechanics model (Fatemi and Yang, 1998; Cheng and Plumtree, 1998; Shang and Yao, 1999). Despite the different proposed damage functions, the basic idea is to calculate the fatigue damage in an evolutionary manner using a scalar damage variable. The main differences lie in the number and characteristics of the parameters used in the model, in the requirements for additional experiments, and in their applicability (Fatemi and Yang, 1998).

From the brief discussion above, it is found that most of the nonlinear fatigue damage models improve the deficiencies within LDR by considering additional loading

effects. However, they are usually computationally expensive compared to LDR especially when the applied loading is repeated block loading or spectrum loading, since most of them require cycle-by-cycle calculation. This disadvantage makes it difficult to perform simulation-based reliability evaluation. Furthermore, the parameters calibration using experimental results is hard to perform for some nonlinear fatigue damage models. The model parameter calibration of double linear damage rule is difficult if only multi-block loading test is available. Some models contain several parameters and need couples of different variable amplitude loading data to solve these parameters uniquely (Goodin et al, 2004). In the following section, we are trying to develop a nonlinear damage accumulation model, which improves the deficiencies within the linear damage accumulation rule but still maintains its computational simplicity. Since the major deficiency of LDR is that it is independent of applied load levels, this paper attempts to modify the LDR to make it load level dependent and yet preserve the linear summation form to make the calculation easier.

We first discuss the stationary loading process. Under laboratory conditions, the stationary loading process is usually approximated by repeated multi-block loading. Within each block, the loading is not stationary. But this assumption of stationary process holds when the material experiences many blocks before it fails (i.e. high-cycle fatigue problem). Under the stationarity assumption, the distribution of applied loading cycles is adequate to describe the loading process.

To make the discussion easier for the fatigue damage accumulation under stationary loading, let us consider a fatigue problem under a repeated two-block loading

first. N_f is the total number of cycles to failure. If the linear damage accumulation rule is used, we obtain:

$$\begin{cases} \frac{n_1}{N_1} + \frac{n_2}{N_2} = 1 \\ n_1 + n_2 = N_f \end{cases} \quad (102)$$

Eq. (100) can be rewritten as

$$\begin{cases} \frac{n_1}{N_1} + A_1 \frac{N_f - n_1}{N_1} = 1 \\ A_1 = \frac{N_1}{N_2} \end{cases} \quad (103)$$

From Eq. (103) we can express the cycle ratio $\frac{n_1}{N_1}$ as a function of cycle distribution $\omega_1 = \frac{n_1}{N_f}$ as

$$\frac{n_1}{N_1} = \frac{1}{\frac{A_1}{\omega_1} + 1 - A_1} \quad (104)$$

If the fatigue S-N curve under constant amplitude loading (s) is expressed as

$$N = g(s) \quad (105)$$

then, A_1 in Eq. (103) is a material parameter depending on the stress levels and equals $\frac{g(s_1)}{g(s_2)}$. Similarly, the cycle ratio of the second stress level can be expressed as a function of the cycle distribution as

$$\frac{n_2}{N_2} = \frac{1}{\frac{A_2}{\omega_2} + 1 - A_2} \quad (106)$$

where A_2 is a material parameter depending on the stress levels and equals $\frac{g(s_2)}{g(s_1)}$.

Substituting Eq. (106) and Eq. (104) into Eq. (103), we obtain

$$\frac{n_1}{N_1}+\frac{n_2}{N_2}=\sum_{i=1}^{2}\frac{1}{\frac{A_i}{\omega_i}+1-A_i} \qquad (107)$$

The above derivation is under the assumption of a linear damage accumulation rule. For the materials that follow this rule, the right hand of Eq. (107) equals unity. For materials that do not follow the linear rule, A_i cannot be determined only by constant amplitude experiments. They depend on the material properties and loading conditions. This parameter can be calibrated using one additional fatigue experiment under variable loading. In the proposed model, we plot the cycle ratio and cycle distribution together for each stress level. Then we compute the coefficients A_i in Eq. (104) through least square regression. Based on the experimental data collected in this study, the following empirical function is used to calculate A_i:

$$A_i=\alpha(s_i/\bar{s})^{\beta} \qquad (108)$$

where α and β are material parameters; s_i is the current stress level and $\bar{s}$ is the mean value of all the stress amplitudes in each block. Notice that the modified LDR (Eq. (107)) is stress dependent.

Eq. (107) is extended for repeated multi-block loading as

$$\sum_{i=1}^{k}\frac{n_i}{N_i}=\sum_{i=1}^{k}\frac{1}{\frac{A_i}{\omega_i}+1-A_i}=\Psi \qquad (109)$$

For continuous stationary spectrum loading, Eq. (109) is expressed as

$$\int \frac{n(s)}{N(s)} ds = \int \frac{1}{\frac{A(s)}{f(s)} + 1 - A(s)} ds = \Psi \qquad (110)$$

where the cycle distribution ω_i (probability description for block loading) becomes the probability density function $f(s)$ of the applied continuous random loading (see Fig. 54). Eq. (109) and Eq. (110) constitute the proposed fatigue damage accumulation model under stationary loading. Compared with the linear damage rule, the proposed model includes the effect of the stress levels. The Miner's sum is not a constant but depends on the cycle distribution of the applied loadings.

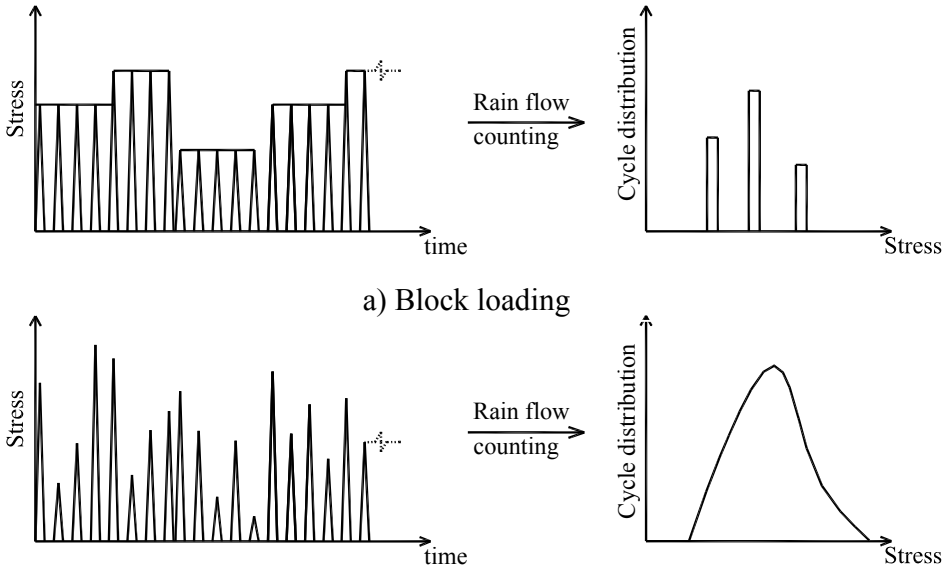

a) Block loading

b) Continuous random loading

Fig. 54 Schematic illustration of cycle distribution using rain-flow counting method

When using Eq. (109) (or Eq. (110)) for fatigue life prediction, the right hand side of Eq. (109) (or Eq. (110)) is first calculated. For repeated multi-block loading, the cycle

distribution of the different stress levels at failure can be approximated using the cycle distribution value in a single block. For high-cycle fatigue, this is a reasonable approximation. Then the fatigue life prediction is performed in the same way as the classical procedure using the linear damage rule.

From Eq. (109) (or Eq. (110)), it is seen that the proposed model still maintains the simplicity of the linear damage rule. It can directly use the cycle counting results and does not require cycle-by-cycle calculation. The proposed model includes the load level effect and load contents effects, which improve the deficiencies within the LDR model. In the later part of this paper, it is shown the proposed model give a more accurate prediction with similar calculation effort compared to the LDR model.

Fatigue damage accumulation under non-stationary loading is complicated compared with that under stationary loading. The proposed model described above is only applicable to stationary loading as it only considers the cycle distribution of the applied loading. For non-stationary applied loading, the cycle distribution is not sufficient to describe the loading process. Under laboratory conditions, step loading is also used for variable loading tests. The material is first pre-cycled under one or several stress levels. Then the material is cycled till failure at a certain stress level. This type of loading is non-stationary as the mean value and variance of the applied loading change corresponding to time. For this type of loading, load sequence effect of the fatigue damage accumulation is observed for some materials (Fatemi and Yang, 1998). The high-low and the low-high loading sequences result in different Miner's sum. A comprehensive study of the general non-stationary loading needs further work. In the current study, several step loading

experimental data are collected. The proposed model shown above is modified to include the load sequence effect for step loadings.

The model coefficients A_i expressed in Eq. (108) are modified as

$$log(A_i) = \alpha + \beta log(\frac{s_i}{\bar{s}}) + \gamma log(\frac{\bar{s}}{s_k}) \qquad (111)$$

where γ is a material parameter to describe the load sequence effect of the material, and s_k is the stress amplitude at the last step. The third term in Eq. (111) represents the load sequence effect on the final fatigue damage of the material. When the material does not experience load sequence effect ($\gamma = 0$) or the applied loading is stationary ($log(\frac{\bar{s}}{s_k}) = 0$), Eq. (111) reduces to Eq. (108). The material parameters in Eq. (111) can be calibrated using the high-low and the low-high step loading experiments following the same procedure for repeated block loading.

Eq. (109) and Eq. (111) are used together for fatigue life prediction under step loadings. For non-stationary loading, the cycle distribution at failure is not known before hand. Therefore a trial and error method can be used to find the solution of Eq. (109). The initial values for cycle distribution can be computated using the LDR model. It is found that usually a few iterations are enough for convergence.

The prediction results using the proposed nonlinear damage accumulation rule are compared with experimental data available in the literature. Only the mean value for the fatigue damage is compared here. The comparison of the variability of the fatigue damage is shown in the next section. The objective is to show the applicability of the model to different materials and different loadings. The collected experimental data

includes metals and composites under step and multi-block loadings. Another guideline in collecting the data is that the experimental data should have enough data points both in the constant amplitude tests and variable amplitude tests, so that reliable statistical analysis and comparisons can be performed.

A brief summary of the collected experimental data is shown in Table 14, which includes material name, reference, variable loading type, and specimen numbers at constant and variable loading tests. In Table 14, the abbreviation and schematic illustration of the applied variable loading is shown in Fig. 54.

Table 14. Experimental description of collected materials

Material name	Refence	Types of Variable loading*	Number of specimens**	
			Constant loading	Variable loading
Nickel-silver	Tanaka et al (1984)	TS	200	50
16Mn steel	Xie (1999)	TS and MS	15	10
LY12CZ aluminum alloy	Wu (1985)	MB	N/A	15~21
Carbon steel	Xie (1999)	TS	15~18	13~15
45 steel-1	Zheng and Wei (2005)	MB	10	9
45 steel-2	Yan et al (2000)	MB	10	6
DD16 fiberglass composite laminates	Mandell and Samborsky (2003)	TB	15~20	3~62

*The abbreviation and schematic illustration of the type of the variable loading is shown in Fig. 54.
** The number of specimens indicates the number under the same stress level (constant loading) or the same type of variable loading.

The material fatigue properties (constant S-N experimental data) are plotted in Fig. 55. The statistics of the experimental data are shown in Table 15, which includes the mean value and standard deviation of the fatigue life at different stress levels. The original data for LY12CZ aluminum alloy under constant amplitude tests are not

available, thus only the statistics of the test data are listed in Table 15. The fatigue lives under constant amplitude tests are assumed to follow the lognormal distribution.

Table 15. Statistics of constant amplitude S-N curve data

Material	Stress amplitude (MPa)	Statistics of Fatigue life (log(N))		Material	Stress amplitude (MPa)	Statistics of Fatigue life (log(N))	
		Mean	Std.			Mean	Std.
Nickel-silver	478	5.62	0.10	45 steel-1	525	5.33	0.32
	583	5.09	0.09		500	5.50	0.34
	666	4.73	0.07		475	5.59	0.29
16Mn steel	394	5.05	0.10		450	5.82	0.35
	373	5.29	0.06		400	6.15	0.26
	344	5.85	0.07	45 steel-2	750	4.49	0.15
LY12CZ	125.44	4.37	0.10		650	5.00	0.14
	101.92	4.76	0.04		630	5.04	0.12
	78.79	5.16	0.09		590	5.24	0.10
	49.98	5.65	0.15		520	5.65	0.24
	46.06	6.01	0.25	DD16 fiberglass composite laminates	206	5.48	0.39
	37.04	6.82	0.13		241	4.83	0.34
Carbon steel	366	4.73	0.19		328	3.29	0.27
	331	5.16	0.14		414	2.44	0.30
	309	5.79	0.16				

The comparison of the prediction results using the proposed nonlinear fatigue damage accumulation rule and the experimental results is performed first. As shown in section 4.2.2, the three different uncertainty modeling techniques have no effect on the mean value of the fatigue damage. In order to minimize the randomness effect on the fatigue damage accumulation modeling, the mean values of the experimental data are used. The comparisons of Miner's sum of the LDR and the proposed model are plotted in Fig. 56. The *x*-axis is the cycle distribution and the *y*-axis is the cycle ratio as described in Eq. (109). The dashed curves are the prediction of the proposed method and the points are experimental results. From Fig. 56, it is seen that the proposed function (Eq. (109))

give a satisfactory prediction and relate the cycle ratio and cycle distribution under different loading conditions.

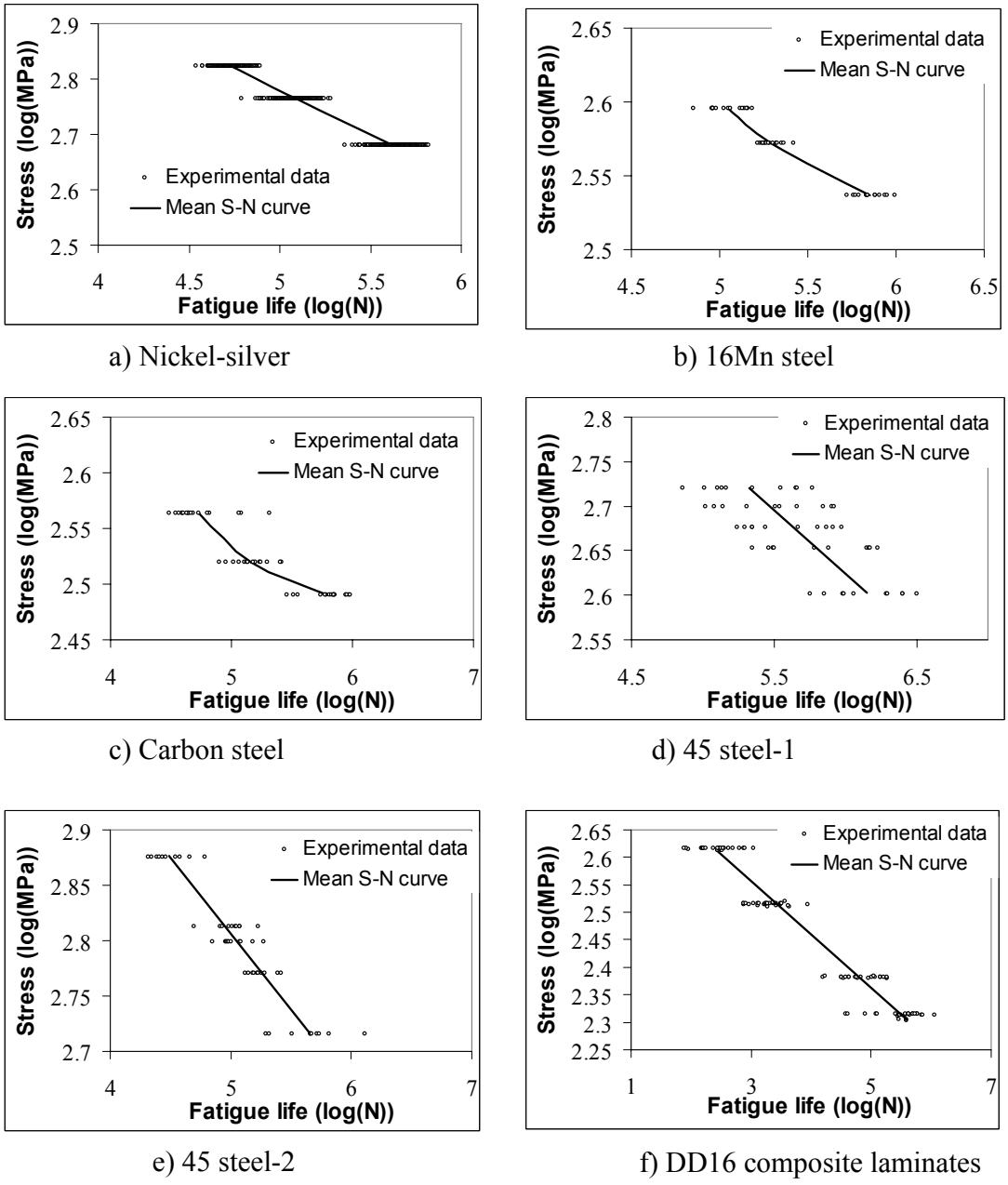

Fig. 55 Constant amplitude S-N curve data for different materials

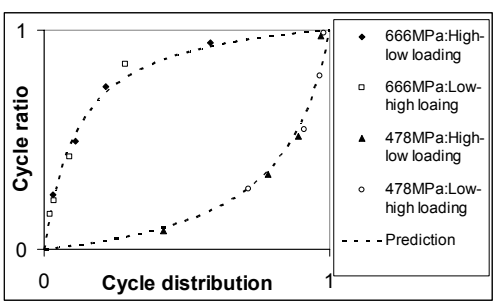

a) Nickel-silver

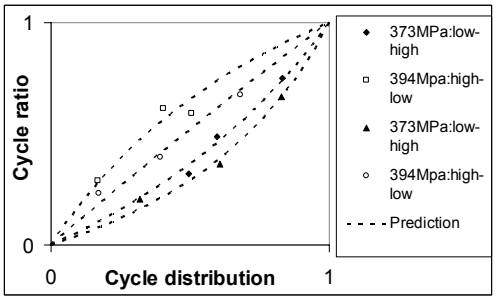

b) 16Mn steel

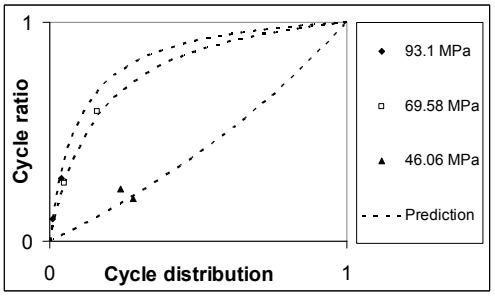

c) LY12CZ aluminum alloy

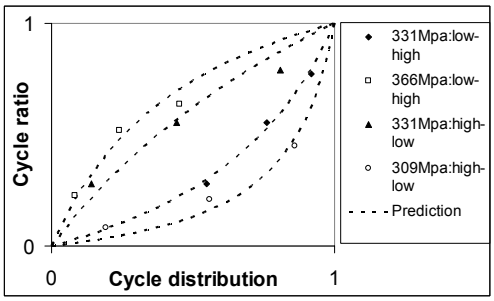

d) Carbon steel

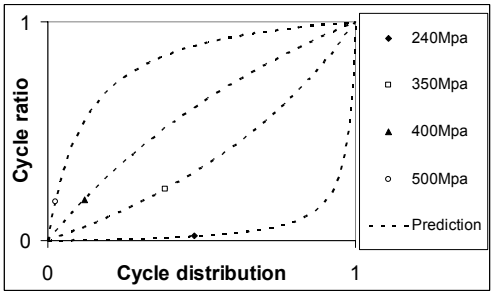

e) 45 steel-1

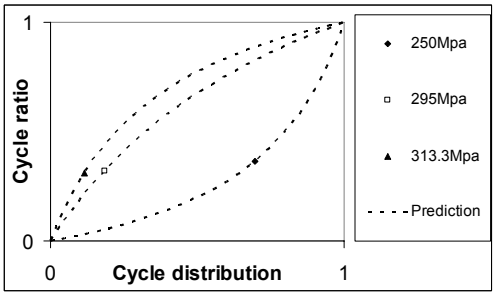

f) 45 steel-1

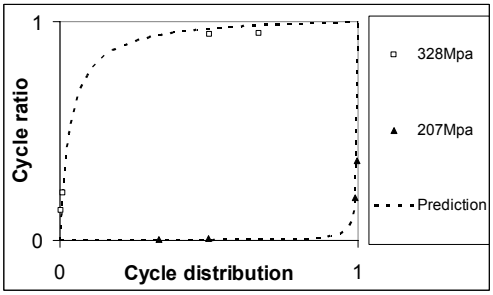

g) DD16 composite laminates

Fig. 56 Cycle ratio and cycle distribution relationship for different materials

The predicted Miner's sums under variable loadings are compared with experimental results for all the materials in Fig. 57. From Fig. 57, it is seen that the proposed method gives a better prediction compared to the LDR. For composite laminates DD16 collected in this study, the average Miner's sum is about 0.5, which is much lower than that predicted by the nonlinear damage accumulation rule. Using the LDR under this condition results a highly non-conservative prediction.

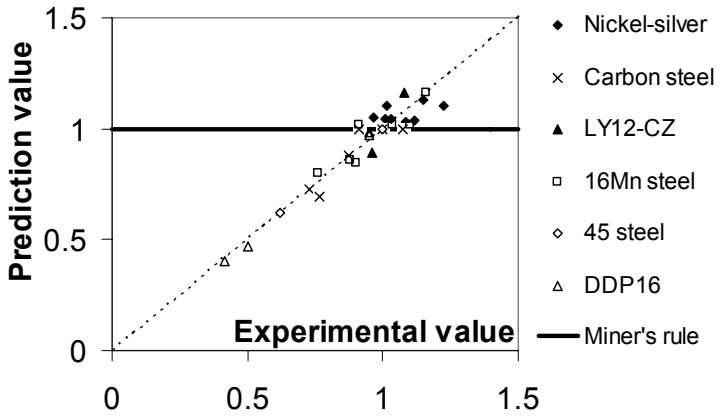

Fig. 57 Comparisons between predicted and experimental Miner's sum for different materials

4.2.2 Uncertainty modeling of material properties

In classical fatigue life analysis, a fatigue damage accumulation rule together with the material properties under constant amplitude loading is used to predict the fatigue life under variable loadings. Many probabilistic methods have been proposed to describe the statistics observed under constant amplitude fatigue tests and to evaluate the reliability under variable loadings. Depending on the method to handle the randomness in constant amplitude tests, the probabilistic methods can be grouped into two categories.

One type is to treat the fatigue lives at different stress levels as independent variables. The statistics of the random variables are described using a statistical distribution function, such as Weibull or lognormal. In this paper, we name this type of approach as statistical S-N curve approach. Liao et al (1995) used a model named dynamic interference statistical model to evaluate the reliability under spectrum loading, which assumes independent lognormally distributed life and linear fatigue damage accumulation. Kam et al (1998) compared several damage accumulation rules including the Miner's rule using both Lognormal and Weibull distribution of fatigue life for composites. Le and Peterson (1999) also used lognormal distribution and the LDR for fatigue reliability analysis of engine blades. Shen et al (2000) used similar assumptions for fatigue life prediction under a narrow band Gaussian stochastic stress process. Kaminski (2002) used a perturbation-based stochastic finite element method for fatigue analysis of composites, in which the LDR was also used. The restrictions of input random variables of fatigue life is looser since only the numerical characteristics of the random variables are required in the computational methodology, such as mean and variance.

The other widely used approach is to use a family of S-N curves corresponding to different survival probability of the material. This approach is also known as quantile or percentile S-N curve (referred as Q-S-N curve in this chapter later on). Shimakawa and Tanaka (1980) used the quantile S-N curve and the LDR to analyze the fatigue reliability under a two-step loading. Both lognormal and Weibull distribution assumption of fatigue life were explored. Kopnov (1993, 1997) proposed a method named intrinsic fatigue curve (IFC), which is another format of the quantile S-N curve approach, combined with the LDR for fatigue analysis. The difference between quantile S-N curve and IFC is that

Q-S-N uses a set of deterministic S-N curves and each represents a different survival probability level. IFC uses a single random function in which the realizations of the random function are the same as Q-S-N. A similar methodology for describing the scatter in the constant amplitude S-N curves was proposed by Pascual and Meeker (1999) using a random fatigue-limit model. This random fatigue limit is explicitly included in the S-N model. Maximum likelihood methods are then used to estimate the parameters of the S-N equation as well as the parameters of the fatigue limit distribution. If the fatigue limit takes the quantile value from the distribution, the resulting S-N curve is the quantile S-N curve. Rowatt and Spanos (1998) used Q-S-N curves and Markov chain models proposed by Bogdanoff and Kozin (1984) for fatigue life prediction of composites. Ni and Zhang (2000) used Q-S-N and LDR for fatigue reliability and compared their prediction results with the experimental results under two-step loading. Zheng and Wei (2005) assumed that the constant fatigue life follows a lognormal distribution and used Q-S-N with LDR for probabilistic fatigue life prediction under repeated block loading. The model predictions were compared with experimental results for one type of steel.

From a statistical point of view, both statistical S-N curve and Q-S-N curve have an important implicit assumption in representing the set of random variables. The statistical S-N curve approach assumes the covariance function of these variables is zero and the quantile S-N curve approach assumes the covariance function is unity. Either assumption can be barely achieved in the realistic condition. A more appropriate approach is to propose an S-N curve representation technique which can include the covariance structure of the constant amplitude fatigue lives. A schematic comparison of the various methods for representing the S-N curves is plotted in Fig. 58.

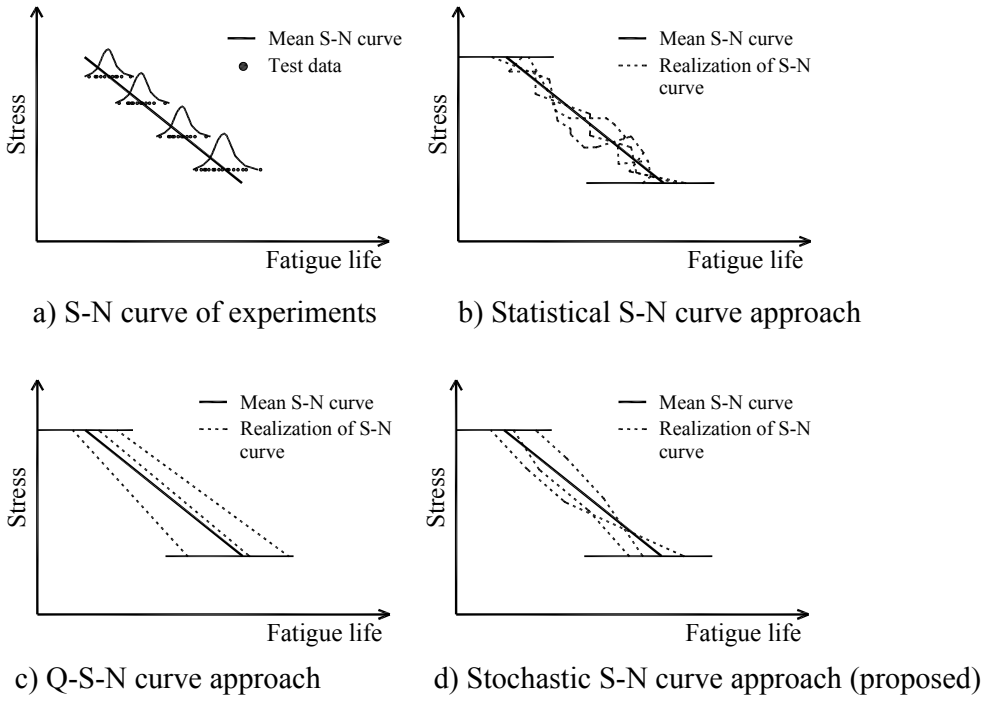

Fig. 58 Schematic comparisons of different approaches in representing the fatigue S-N curve

In this work, the fatigue lives N under different constant amplitude tests are treated as random fields/processes with respect to different stress levels s. Stochastic expansion techniques are very successful in describing the variation in the corresponding random field/process. Several methods are available, such as spectral representation method (Grigoriu, 1993; Shinozuka and Deodatis, 1991), Karhunen-Loeve (KL) expansion method (Loeve, 1977), polynomial chaos expansion (Ghanem and Spanos, 1991; Ghanem, 1999) etc. In this study, the KL expansion technique is used and a new stochastic S-N curve method is proposed based on the KL expansion technique.

The fatigue lives under constant amplitude loading are assumed to follow the lognormal distribution for the sake of illustration. As mentioned earlier in this section,

both lognormal and Weibull distributions are commonly used in the literature. The lognormal assumption makes the $log(N(s))$ a Gaussian process with mean value process of $log(\overline{N}(s))$ and standard deviation of $\sigma_{log(N)}(s)$, where $log(\overline{N}(s))$ is the mean S-N curve obtained by regression analysis. It needs to be pointed out that the Gaussian assumption is not a requirement in the proposed methodology. Non-Gaussian methods for random field representation are available and can be applied to the problem without difficulty. It is shown that the lognormal distribution gives a satisfactory prediction for the materials collected in this study.

It has been shown that the variance is not a constant but a function of stress level s (Pascual and Meeker; 1999). The $\sigma_{log(N)}(s)$ represents the scatter in the data and can be obtained by classical statistical analysis. Based on the above assumption, the process

$$Z(s) = \frac{(log\, N(s)) - log(\overline{N}(s))}{\sigma_{log(N)}(s)} \qquad (112)$$

is a normal Gaussian process with zero mean and unit variance.

From a physical standpoint, the autocovariance function of the fatigue lives should decrease as the difference between stress levels increases. An exponential decay function is proposed for the covariance function $C(s_1, s_2)$ of $Z(s)$ as

$$C(s_1, s_2) = e^{-\mu|s_1 - s_2|} \qquad (113)$$

where μ is a measure of the correlation distance of $Z(s)$ and depends on the material. In classical S-N fatigue experiments, the specimen is tested until failure or runout at a specified stress level and cannot be tested at the other stress levels. Due to the non-repeatable nature of fatigue tests, the covariance function cannot be determined by constant amplitude fatigue experimental data alone. Since in the proposed methodology,

the nonlinear fatigue damage accumulation model also needs one additional variable loading fatigue test to calibrate the model parameters α , β and/or γ . μ can be calibrated by the same variable loading fatigue test data as well.

In KL expansion, the random process/field $Z(s)$ can be expressed as a function of a set of standard random variables, or, in other words, expressed as a combination of several random functions. Generally, the expansion takes the form

$$Z(s) = \sum_{i=1}^{\infty} \sqrt{\lambda_i}\, \xi_i(\theta) f_i(s) \qquad (114)$$

where $\xi_i(\theta)$ is a set of independent random variables, satisfying

$$\begin{cases} E(\xi_i(\theta)) = 0 \\ E(\xi_i(\theta)\xi_j(\theta)) = \delta_{ij} \end{cases} \qquad (115)$$

where E denotes the mathematical expectation operator, and δ_{ij} is the Kronecker-delta function.

In Eq. (114), $\sqrt{\lambda_i}$ and $f_i(x)$ are the *ith* eigenvalues and eigenfunctions of the covariance function $C(s_1, s_2)$, evaluated by solving the homogenous Fredholm integral equation analytically or numerically:

$$\int_D C(s_1, s_2) f_i(s_2) = \lambda_i f_i(s_1) \qquad (116)$$

In practical calculation, only a truncated number of terms in Eq. (114) is required to achieve the satisfied accuracy. Under the standard Gaussian assumption, ten to twenty terms are adequate to get very precise results. The detailed computational procedure for KL expansion can be found elsewhere (Phoon et al, 2002; Huang et al, 2002).

From Eqs. (111)~(115), we obtain

$$\log(N(s)) = \sigma_{\log(N)}(s)\sum_{i=1}^{\infty}\sqrt{\lambda_i}\,\xi_i(\theta)f_i(s) + \log(\overline{N}(s)) \qquad (117)$$

Substituting Eq. (118) into Eq. (109) (or Eq. (110)), we can solve for the fatigue life under variable amplitude loading. No analytical solution exists and Monte-Carlo simulation is used to find the probabilistic fatigue life distribution.

The proposed uncertainty modeling method in this section includes the covariance structure in the fatigue analysis. The importance of the covariance structure on the final reliability evaluation can be illustrated using the example problem below.

Consider a two-block loading case under linear damage accumulation assumption. The covariance function for statistical S-N approach, Q-S-N and the proposed stochastic S-N approach can be expressed as

$$\begin{cases} C(s_1, s_2) = 0 & statistical\ S-N\ \ curve \\ C(s_1, s_2) = 1 & Q-S-N \\ C(s_1, s_2) = e^{-\mu|s_1 - s_2|} & stochastic\ S-N\ \ curve \end{cases} \qquad (118)$$

For fatigue damage accumulation

$$D = \frac{n_1}{N_1} + \frac{n_2}{N_2} = D_1 + D_2 \qquad (119)$$

the mean value of the fatigue damage is

$$E(D) = E(D_1) + E(D_2) \qquad (120)$$

and the variance of the fatigue damage is

$$Var(D) = Var(D_1) + Var(D_2) + 2\rho Var(D_1)Var(D_2) \qquad (121)$$

where ρ is the correlation coefficient of the random variables D_1 and D_2. It is seen that the different approaches have no effect on the mean value of the fatigue damage but have effect on the variance. Thus,

$$Var(\text{statistical} \quad S-N) \le Var(\text{stochastic} \quad S-N) \le Var(Q-S-N) \qquad (122)$$

A schematic representation of the failure probability with respect to time from the three methods is shown in Fig. 59. The mean value of the fatigue life is 5 (log scale) and standard deviation is 0.1, 0.15 and 0.2 (log scale) for statistical S-N, stochastic S-N and Q-S-N, respectively. These amounts of difference in the standard deviation are observed for the collected materials in this study. Thus different approaches give different fatigue reliability estimates. The difference is especially significant around the tail region. For design and maintenance against fatigue, it is usually required that the mechanical component stay at a very low failure probability (i.e. less than 0.1%). At this stage, the difference among the three approaches is around 0.16 in log scale, which is about 45% difference in real life cycles. Zheng and Wei (2005) used Q-S-N approach and observed that the standard deviation of the predicted fatigue life of 45 steel notched elements under variable amplitude loading is longer than that of test results. The authors stated that the reason behind it should be further investigated. Eqs. (118) - (122) give a possible explanation for this phenomenon, i.e., the effect of the correlation structure. Since the fully un-correlated and fully correlated cases can be barely found in reality, the standard deviation of the experimental results should lie between those predicted by the statistical S-N approach and the Q-S-N approach. In the next section, it is shown that this phenomenon is not only for 45 steel but also for other materials.

It is interesting to notice that the statistical S-N approach and Q-S-N are two special cases of the proposed method. If μ in Eq. (119) approaches positive infinity, the covariance function reduces to zero, giving the statistical S-N method. If μ in Eq. (119) approaches zero, the covariance function reduces to 1, giving the Q-S-N method.

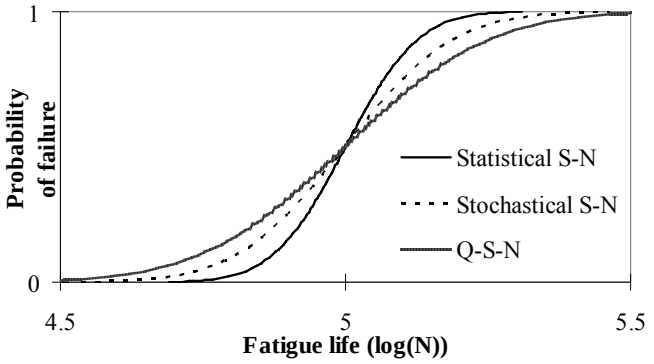

Fig. 59 Failure probability predictions by different approaches

For the stochastic fatigue modeling methodology, the final objective is to predict the fatigue life distribution under different variable loadings. This enables the reliability estimation of mechanical components. In this section, the predicted fatigue life distributions are compared with the empirical fatigue life distribution of experimental data. Due to large number of experimental data collected in this study and the space limitations, we only show the comparisons under several loading conditions for each material. The comparisons are shown in Fig. 60 by plotting the predicted and experimental distribution together. The details of the plotted experimental distributions are listed in Table 16. All the prediction results are obtained using 10,000 Monte Carlo simulations. Since the proposed nonlinear damage accumulation model does not require cycle-by-cycle calculation, the computational time is very short and ranges from 5-20 seconds for 10,000 Monte Carlo simulations. In Fig. 60, the stepped lines are experimental results and the smooth lines are prediction results. It is observed that the prediction results agree with the experimental results very well for different variable loadings.

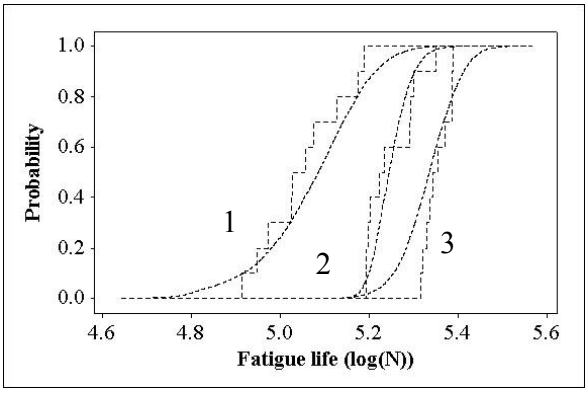

a) Nickel-silver

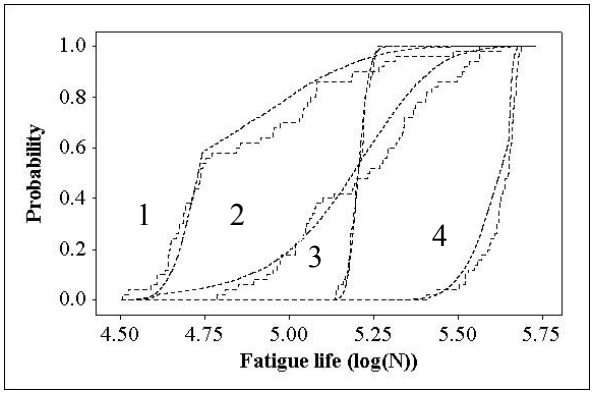

b) 16Mn steel

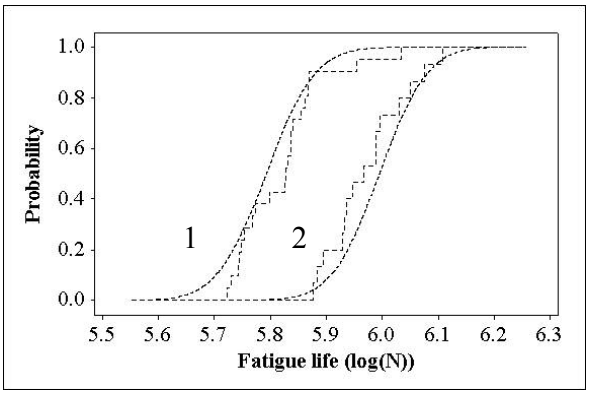

c) LY12CZ aluminum alloy

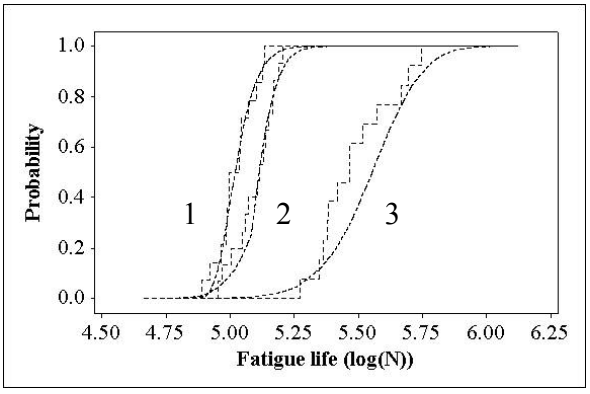

d) Carbon steel

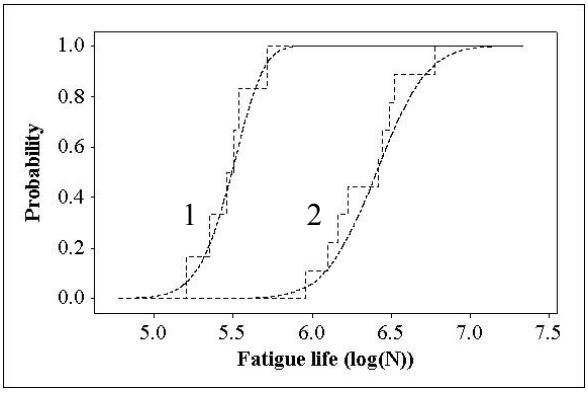

e) 45 steel

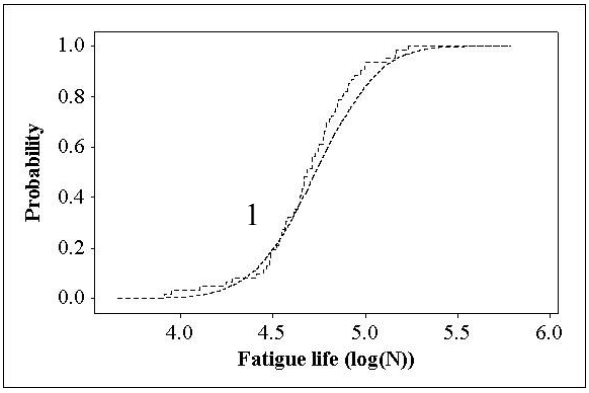

f) DD16 composite laminates

Fig. 60 Empirical cumulative distribution function comparisons between prediction and experimental results

Table 16. Experiments description shown in Fig. 60

Material	Symbol in Fig. 60	Variable loading*
Nickel-silver	1-Fig. 60(a)	TS: 666 (5.54x104) → 478 (X)
	2-Fig. 60(a)	TS: 666 (3.98x104) → 478 (X)
	3-Fig. 60(a)	TS: 478 (1.15 x105) → 666 (X)
	4-Fig. 60(a)	TS: 478 (4.46 x105) → 666 (X)
16Mn steel	1-Fig. 60(b)	TS: 394 (7.5 x104) → 373 (X)
	2-Fig. 60(b)	TS: 373 (1.46 x105) → 394 (X)
	3-Fig. 60(b)	MS: 373 (105) → 394 (105) → 373 (105) → 344 (105) → 394 (105) → 344 (105) → 394 (X)
LY12CZ	1-Fig. 60(c)	MB: 93.1 (2.64x103) → 69.58 (1.056x104) → 46.06 (1.848x104) → 23.52 (3.432x104)
	2-Fig. 60(c)	MB: 93.1 (6.6x102) → 69.58 (3.3x103) → 55.86 (6.6x103) → 46.06 (1.584x104) → 37.24 (3.96x104)
Carbon steel	1-Fig. 60(d)	TS: 331 (8.06 x104) → 373 (X)
	2-Fig. 60(d)	TS: 331 (1.21 x105) → 373 (X)
	3-Fig. 60(d)	TS: 331 (4.03 x105) → 309 (X)
45 steel-1	2-Fig. 60(e)	MB: 240 (105) → 350 (8x104) → 400 (2.5x104) → 500 (104) → 400 (2.5x104) → 350 (8x104) →240 (105)
45 steel-2	1-Fig. 60(e)	MB: 500 (1.5x104) → 590 (4x103) → 626.6 (5x103) → 590 (4x103) → 500 (1.5x104)
DD16	1-Fig. 60(f)	TB: 328 (10) → 207 (103)

* The number before the bracket indicates the stress level and the number in the bracket is the applied cycle numbers. For the step loadings (TS and MS), the applied cycle number of the last stress level is not known as prior and thus an "X" is used.

The standard deviation of the fatigue life of experiments and predictions are plotted in Fig. 61, for all the experimental data collected in this study. The predictions using statistical S-N approach, Q-S-N approach and the proposed stochastic S-N approach are plotted together. The prediction results of all three approaches use 10,000 Monte Carlo simulations. Points lying close to the diagonal line indicate close agreement between the experimental results and the prediction results. From Fig. 61, it is seen that the statistical S-N approach tends give a smaller variance prediction, since most of the prediction results lie below the diagonal line. The Q-S-N tends to give a larger variance prediction, since most of them lie above the diagonal line. The proposed stochastic S-N approach is closer to the experimental results, since the variance prediction is between the

statistical S-N approach and Q-S-N approach. This type of observation is consistent with Eq. (122). It can be concluded that the covariance structure in the S-N curve is important for probabilistic fatigue life prediction under variable loading and thus needs to be considered in analysis and design.

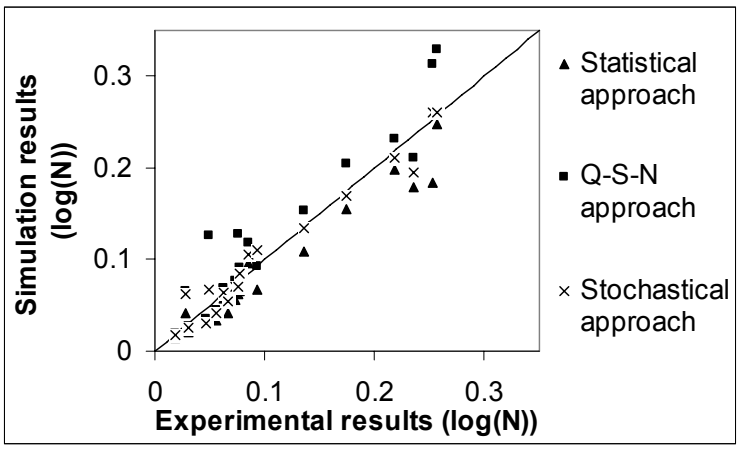

Fig. 61. Comparisons between predicted and experimental Std. for different approaches

4.2.3 Uncertainty modeling of applied loading

Two approaches are commonly used to describe the scatter in the random applied loading to describe the scatter in the random applied loading. One is in the frequency domain and uses power spectral density methods. The other is in the time domain and uses cycle counting techniques. The major advantages of the frequency domain approach are that it is more efficient and can obtain an analytical solution under some assumptions of the applied loading process, such as Gaussian process, stationary and narrow banded. This of cause limits the applicability of the frequency domain approach to some real problems (Jiao 1995; Tovo, 2000). Also, most of the frequency domain approaches

assume the linear fatigue damage accumulation rule (Fu and Cebon, 2000; Banvillet et al, 2004, Benasciutti and Tovo, 2005), due to the loss loading sequence information during the computation of the power spectral density function from the loading history.

The time domain approach is used in this paper. Among many different cycle counting techniques, rain flow counting is predominantly used and is adopted in the proposed methodology. A detailed description of the rain flow counting method can be found in Suresh (1998).

In the proposed fatigue damage accumulation model, the cycle distribution is required for fatigue life prediction. This information can be obtained by performing rain flow counting of the loading history. A schematic explanation is shown in Fig. 54 for two different loading histories.

A Monte Carlo (MC) simulation technique is used for damage accumulation and probabilistic life prediction. As shown in the section 4.2.1 of damage accumulation rule, the whole life of the mechanical components is divided into small blocks. Each block has the specific stress amplitude and the number of cycles. For stochastic loading during a certain time period, not only is the stress amplitude S_{eq} a random variable, but also the number of cycles n_i at the stress amplitude S_{eq}. Nagode and Fajdiga (1998) proved that conditional PDF ($f_{n_i|S_{eq}}(n_i)$) of number of cycles n_i at the stress amplitude level S_{eq} can be modeled by Normal distribution based on the DeMoivre–Laplace principle with the mean and standard deviation expressed in Eq. (123).

$$\begin{cases} \mu = 1 + (N-1)(1 - F(S_{eq})) \\ \sigma = \sqrt{(N-1)(1 - F(S_{eq}))F(S_{eq})} \end{cases} \quad (123)$$

where N is a long enough loading cycle, $F(S_{eq})$ is the cumulative density function (CDF) of the stress amplitude, which can be obtained by rain-flow counting technique.

The proposed stochastic fatigue life prediction methodology includes various uncertainties in the material and loadings. It also includes the randomness of spatial and temporal domain.

First, consider the stress response at a specific location and time instant. The equivalent stress amplitude S_{eq} is calculated using Eq. (5). At any fixed location, S_{eq} is a random variable with probability density function (PDF) of $f_{S_{eq}}(S_{eq})$. Next, the fatigue damage caused by the stress amplitude is usually expressed as a fraction of total number of cycles to failure:

$$D = \frac{1}{N_s} \tag{124}$$

where N_s is the fatigue life estimation from the S-N curve under constant stress amplitude S_{eq}. N_s represents the material resistance to fatigue loading. It is also a random variable at certain stress amplitude. The conditional PDF of N_s can be found from experimental data and expressed as $f_{N_s|S_{eq}}(N_s)$. The single cycle damage considering both the randomness in material resistance and applied stress amplitude is a random variable and its joint PDF can be expressed as:

$$f_D(D) = f_{D|S_{eq}}(D) f_{S_{eq}}(S_{eq}) = \frac{1}{D^2} f_{N_s|S_{eq}}\left(\frac{1}{D}\right) f_{S_{eq}}(S_{eq}) \tag{125}$$

For the fatigue damage accumulation process in the time domain, a damage accumulation rule is required. In the current study, the nonlinear damage accumulation rule is used (Eq. (108)).

Combining Eq. (108) and Eq. (124), the PDF of the total damage at a specific location can be expressed as:

$$f_{D_{total}}(D_{total}) = \frac{1}{\Psi}\frac{1}{D^2} f_{N_s|S_{eq}}(\frac{1}{D}) f_{n_i|S_{eq}}(n_i) f_{S_{eq}}(S_{eq}) \quad (126)$$

Fatigue crack initiation is assumed to occur when the fatigue damage equals or exceeds Ψ. For multiple site fatigue, we check the damage accumulation at different locations. If fatigue damage exceeds Ψ at one location, the number of loading blocks is the fatigue life of the structure. Eq. (127) is a general expression for structural fatigue damage.

$$D_{structure} = max(D_{total,x_j}) = G(x_j, N_i, R_1, ...R_P) = 1 \quad (127)$$

where x_j is the coordinate at the different location, N_i is the number of loading cycles to fatigue crack initiation, R_1 through R_P are random variables which affect the fatigue damage in the structure. Solve Eq. (127) for N_i, we obtain

$$N_i = f_i(x_j, R_1, ...R_P) \quad (128)$$

Eq. (128) shows that the fatigue crack initiation life is a function of geometric locations and input random variables. Analytical solution for N_i using Eq. (128) is rather complicated and sometimes impractical. Therefore, we use Monte Carlo simulation to calculate the fatigue crack initiation life.

Once the fatigue crack is initiated, we use the proposed fatigue crack propagation model to predict the fatigue crack propagation life. The equivalent stress intensity amplitude K_{eq} is calculated using Eq. (89). At any point at the crack tip, K_{eq} is a random variable with probability density function (PDF) of $f_{K_{eq}}(K_{eq})$. Following the similar

procedure for the stochastic fatigue crack initiation life prediction, the loading histories can be divided into many small blocks. In each block, the crack propagation length is accumulated to the initial crack length. When the crack reaches the critical length, the mechanical component is assumed to fail. The failure criterion is expressed as

$$a_{total} = a_i + \sum_{m=1}^{R} a_m \geq a_c \qquad (129)$$

where R is the number of loading blocks, a_m is the crack length increment during each loading block. In Eq. (129), a_i, a_m and a_c are random variables. a_i is the initial crack length after the crack initiation and can be calculated using the Kitagawa diagram (Eq. (78)) and is related to material properties. a_c is obtained using field observations of failure components (failed railroad wheels in the current paper). a_m is calculated using the proposed crack propagation model and is related to the applied stochastic loading and material properties. Solve Eq. (128) for fatigue crack propagation life N_p, we obtain

$$N_p = f_p(a_i, a_c, R_1, ...R_p) \qquad (130)$$

Eq. (130) shows that the fatigue crack propagation life is a function of several random variables. Analytical solution for N_p using Eq. (130) is rather complicated and sometimes impractical. Therefore, we use Monte Carlo simulation to calculate the fatigue crack propagation life.

Combining the fatigue crack initiation life and propagation life together, we obtain the total life of mechanical components.

4.3 Response surface approximation and design of experiments

The response surface method (RSM) was originally proposed by Box and Wilson (1954) as a statistical tool, to find the operating conditions of a chemical process at which some response was optimized. Myers and Montgomery (1995) and Khuri and Cornell (1997) describe the application of RSM to a wide range of physical problems. The basic idea in RSM is to describe the approximate relation between input variables and output variables using a few sample points. Despite numerous different methods suggested by different authors, the general steps involved in RSM are the same: (1) choose the input sample points, which is called design of experiments (DOE); (2) analyze the system performance using the chosen input samples and obtain the interested output results; (3) develop the mathematical relationship between input variables and output variables using least squares curve fitting.

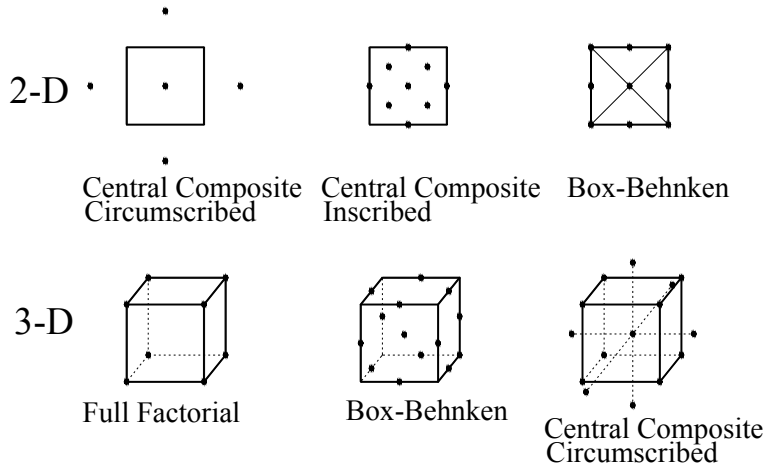

Fig. 62. Several DOE rules

Several DOE methods are available and are suitable for different types of problems and random parameters (Ghiocel, 2001). Some of these are shown in Fig. 62. The choice of DOE is critical for computational efficiency and accuracy. In DOE, some authors build the experimental design in the physical space (Bucher and Bourgund, 1990; Liu and Moses, 1994); while some others build the experimental design in the uncorrelated standard normal space (Enevoldsen, 1994; Lemaire, 1998).

Due to the expensive computational effort involved in the rolling contact finite element modeling, the response surface method (RSM) is used here to describe the approximate relation between input variables and output variables using a few sample points.

In the current study, three random variables are considered for the crack initiation and the crack propagation analysis. Full factorial design is used to illustrate the methodology for probabilistic fatigue life prediction. If the number of random variables increased, efficient DOE methods (i.e., Latin Hypercube sampling) can be used to reduce the computational cost. The final objective of current response surface approximation is to find the relationship between the equivalent fatigue stress and the equivalent stress intensity factor under multiaxial loading corresponding to some input random variables.

4.3.1 Fatigue crack initiation life

Previous parametric studies showed that several geometric and material variables have important effects on the final fatigue life of railroad wheels. The wheel diameter, material hardness and applied loading have important effects on the fatigue crack initiation life railroad wheels. The initial crack location, crack length and applied loading have important effects on the fatigue crack propagation life of railroad wheels. The lower,

middle and upper design values for five variables are listed in Table 17. In Table 17, the applied loading is normalized with the maximum design loading specified in AAR (1998). A total of 54 numerical experiments for fatigue crack initiation analysis and fatigue crack propagation analysis are evaluated using the finite element modeling and fatigue modeling described in the present study.

Table 17. Design values for the three random variables

Random variables (unit)	**Lower**	**Middle**	**Upper**
Wheel diameter D (in)	28	33	38
Hardness Ha (BHN)	235	320	405
Applied loading F	0.4	1.0	1.5
Crack depth a (mm)	5	6	8
Crack length d (mm)	1	5	15

Analysis of the numerical results shows that the maximum equivalent stress not only varies its amplitude but also its location (depth below the tread surface). A two-step regression analysis is performed to handle this problem. First, for each numerical experiment, a rational regression function (Eq. (131) is used to formulate the stress variation corresponding to the depth.

$$S_{eq} = \frac{1}{A + Bx + Cx^2} \qquad (131)$$

where S_{eq} is the equivalent stress, A, B and C are the function of input random variables, x is the depth below the tread surface.

The regression results using Eq. (131) for two specific numerical examples are plotted in Fig. 63(a). The regression results for all the numerical examples are plotted in Fig. 63(b). It needs to be pointed out that Eq. (131) is a random function, which

represents the stress variation corresponding to spatial domain. The regression result of Eq. (131) is used for fatigue life prediction in the next section.

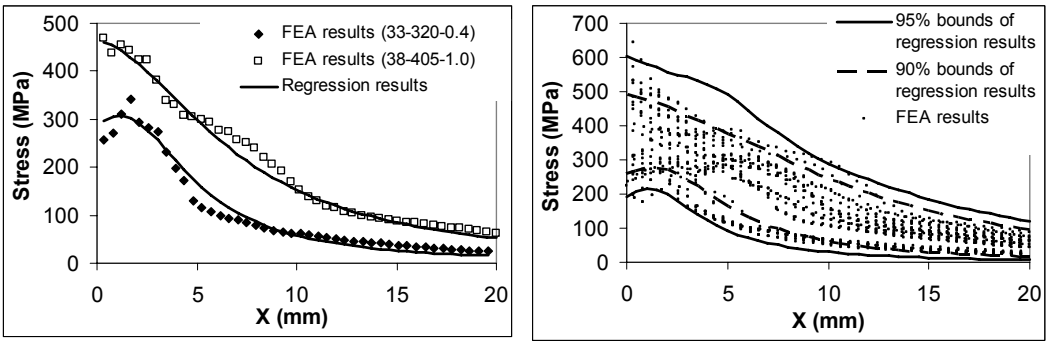

(a) Individual comparison (b) Overall comparison

Fig. 63 Comparison between FEA results and regression results

4.3.2 Fatigue crack propagation life

For the crack propagation analysis, the equivalent stress intensity factor is expressed as

$$K_{eq} = f(F, a, d) \qquad (132)$$

As shown before in the parametric study, the stress intensity factor at the different locations around the crack front show different behavior. In the current study, we use the stress intensity factor the critical crack length along the major axis to predict the fatigue crack propagation life.

In the previous parametric study, it is shown that the equivalent stress intensity is almost linear to the applied loading. But the curve does not go through the origin point, which is due to the friction effect between the two crack surfaces. When the loading is very small, the two surfaces can not slip and result no mode II and III stress intensity. When the loading is high enough and exceeds a threshold value, it causes the slip motion

between the two crack surfaces and the mode II and III stress intensity factors. A reasonable formula needs to include this effect.

The crack depth effect in the previous parametric study shows that the equivalent stress intensity factor achieves local maxima at a certain depth below the tread surface. This effect can be included into the formula by a critical depth parameter. The stress intensity factor decreases as the distance between the crack and the critical depth increases.

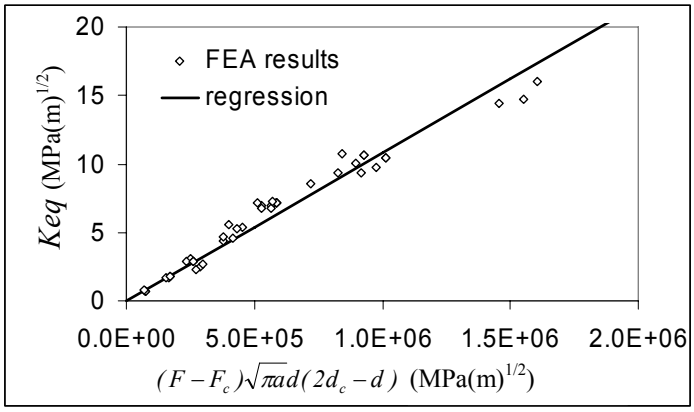

Fig. 64 Comparison between the simplified formula and FEA results

Based on the above discussion and the finite element results, a simple formula is proposed to calculate the equivalent stress intensity factor as

$$K_{eq} = \xi(F - F_c)\sqrt{\pi a d(2d_c - d)} \qquad (133)$$

where F_c is the characteristic loading to trigger the slip motion of the two crack surfaces. d_c is the critical depth at which the stress intensity factor achieve the local maxima. ξ is a scale factor. The prediction using Eq. (133) and the finite element results are plotted in

Fig. 64. It is seen that the proposed formula agrees with the finite element results very well.

4.4 Monte Carlo simulation and field observations

A Monte Carlo simulation-based methodology is used to calculate the probabilistic life distribution of railroad wheels. The response surface developed in Section 4.3 is used to calculate the fatigue crack initiation and propagation life. Various uncertainties from material properties, wheel geometry, applied loading and crack profiles are included in the proposed calculation. The predicted fatigue lives are compared with field observations from the UP failure database.

4.4.1 Statistics of input random variables

For the wheel-rail rolling contact problem, the required distribution function of the input random variables are obtained from experimental data or using some assumptions. The details are shown below.

The fatigue S-N curve was obtained using the experimental data reported by Bernasconi et al (2004) for high speed wheel materials. The median fatigue S-N curve and its 90% bounds are plotted with experimental data in Fig. 65. Due to the insufficient data to construct the covariance structure of the fatigue S-N curves, we used the Q-S-N curve as it produced conservative prediction. For wheel diameter, collected field data shows that it can be described as a multinomial distribution. The histogram of wheel diameter is plotted in Fig. 66. The applied loading on railroad wheels appears to be a bimodal distribution. The reason is that the service loading on track can be classified as

empty loaded and full loaded. In the current study, this distribution is simulated using Eq. (134).

$$F_{bi\,mod\,al}(R_L) = 0.44F_{log\,normal}(R_L) + 0.56F_{weibull}(R_L) \quad (134)$$

where $F_{XXXXX}(R_L)$ is the CDF of different distributions. No experimental data for material hardness distribution is available. However, the hardness value for class B and C railroad wheels is bounded between 277 and 363 (AAR, 1998). In the current study, we assume it follows Beta distribution. The PDF of beta distribution is plotted in Fig. 68.

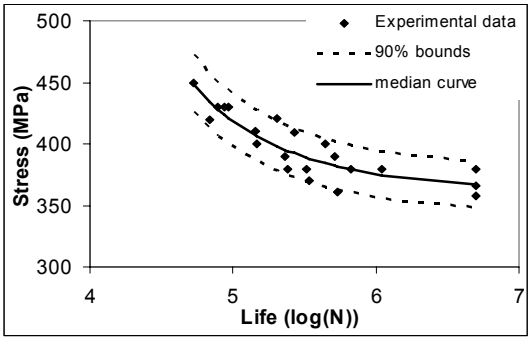

Fig. 65 Fatigue S-N curve

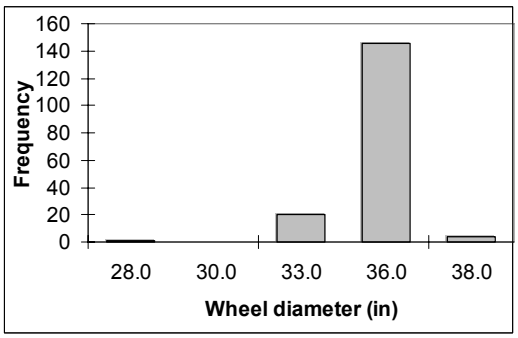

Fig. 66 Histogram of wheel diameter

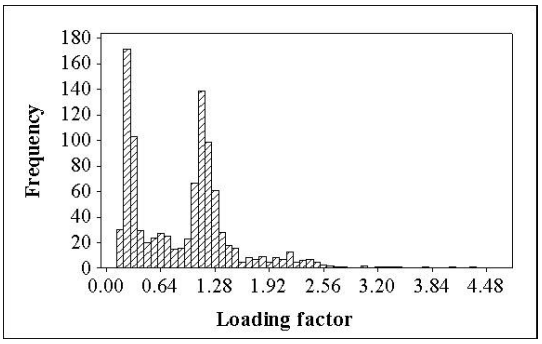

Fig. 67 Histogram of loading factor

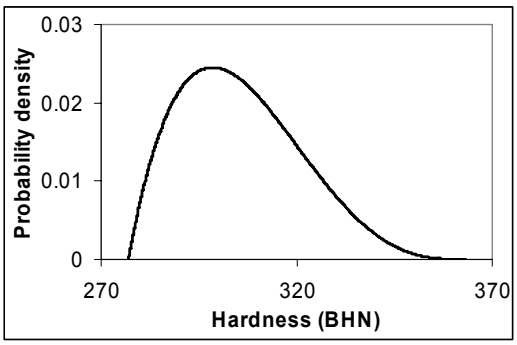

Fig. 68 PDF of hardness distribution

The fatigue crack propagation curve reported in the Union Pacific database is used. The median and 90% confidence bounds are plotted in Fig. 69. The initial crack

size after the fatigue crack initiation is calculated using the Kitagawa diagram. It depends on the fatigue limit and the fatigue crack threshold value. In the current study, the initial crack length is approximated using a lognormal distribution. The PDF of the initial crack length is plotted in Fig. 70. The crack depth uses the previous prediction results of fatigue crack initiation. The final failure crack length uses the collected data from UP failure database. The critical crack length is approximated using a lognormal distribution. The histogram and lognormal fit are plotted in Fig .71.

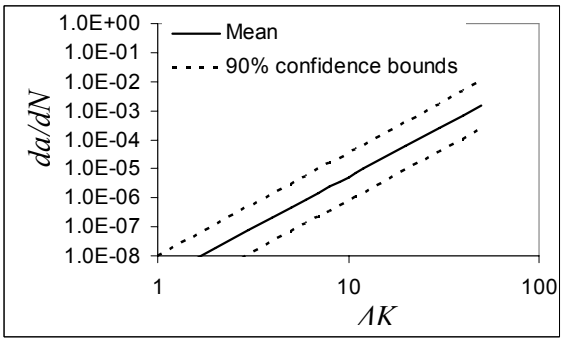

Fig. 69 Fatigue crack growth curve

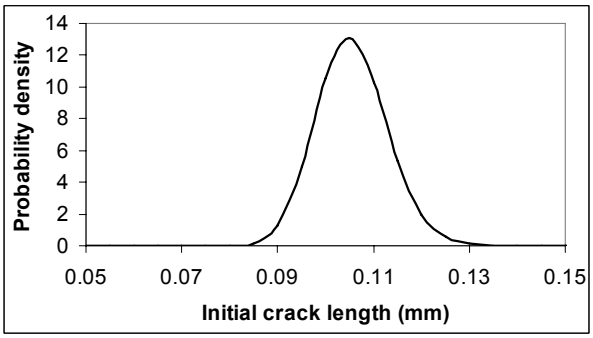

Fig. 70 PDF of initial crack length

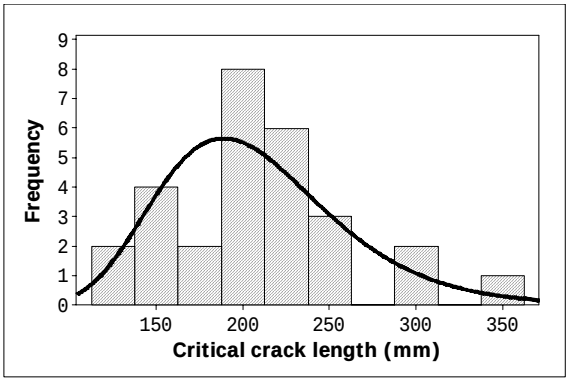

Fig. 71 Histogram of critical crack length

4.4.2 Probabilistic life distribution and reliability

Using the described statistics of the input random variables, the Monte Carlo simulation can be used to predict the final failure of railroad wheels.

Ten thousand Monte Carlo samples are used to simulate the fatigue failure life of railroad wheels. Field data regarding the number of cycles to failure of railroad wheels are collected and compared with the Monte Carlo simulation results. The empirical CDF of the numerical fatigue life prediction and the field observations are plotted in Fig. 72. The fatigue life in Fig. 72 is censored at $2x10^9$ because the wheel would fail due to other failure mechanism by the end of their time-period.

In Fig. 72, the numerical fatigue life prediction agree with the field observation well and capture the major trend of the life distribution. However, a significant difference is observed at the short life region, i.e. the tail region of the CDF of the fatigue life distribution. This type of observation indicates that other factors affecting the fatigue life need to be considered, such as initial defects, brake and thermal loading. The latter two factors are beyond the scope of the current study. Only the effect of initial defect is considered here since the fracture mechanics-based fatigue crack analysis has been developed in this study. Since no information about the initial defect geometry and distribution is available at this stage. Two different lengths of the initial defect are assumed. One is 3.2 mm (1/8 in) according to the regulation of AAR. The other is 10 mm. The location of the initial defect is assumed to be uniformly distributed between 5 mm to 8 mm below the tread surface. It is also assumed that the initial defect can be approximated as an elliptical crack so the proposed fatigue crack propagation analysis can be used. Monte Carlo simulation is used again to calculate the fatigue life of

defective railroad wheels, in which 10% of the failed wheels are assumed to be controlled by the large initial defects. The numerical prediction and field observations are plotted in Fig. 73. It is seen that the numerical prediction are closer to the field observations if the initial defect is considered. For the 10 mm initial defect assumption, the numerical prediction is almost identical with field data. It is clear that large initial defects significantly reduce the wheel reliability. The current comparison is only qualitative as the initial defect information is assumed. Future work is required to study the effect of the initial defect and other factors quantitatively.

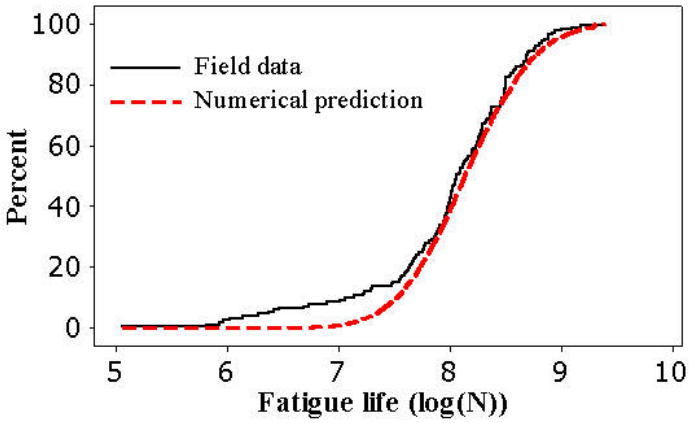

Fig. 72 Empirical CDF of the field data and numerical predictions with no initial defects

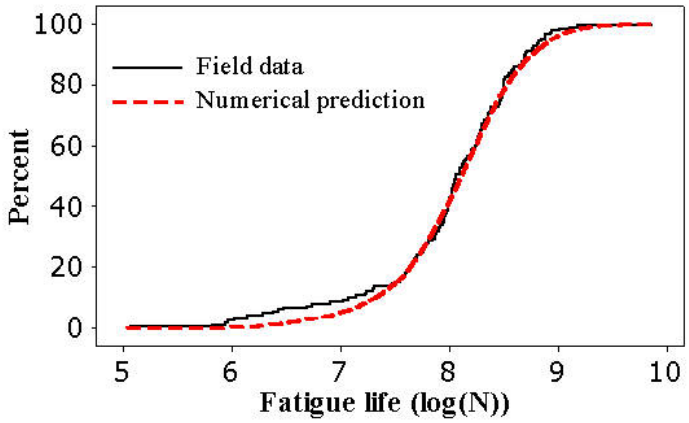

a) 3.2 mm initial defect

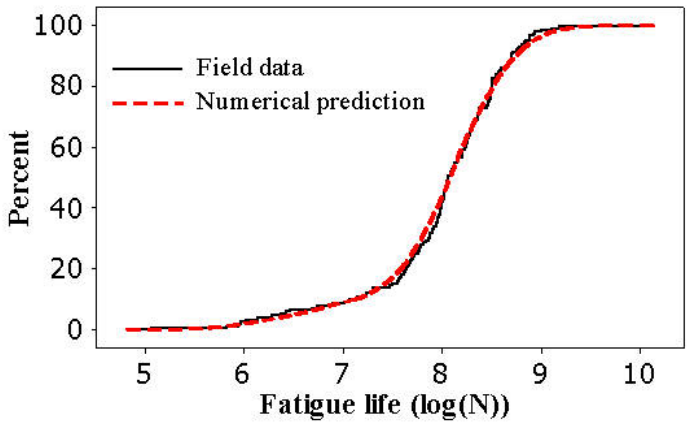

a) 10 mm initial defect

Fig. 73 Empirical CDF of the field data and numerical predictions with initial defects

4.5 Summary

A general stochastic fatigue life prediction methodology under variable loading is proposed in this study. It combines a nonlinear fatigue damage accumulation rule and a stochastic S-N curve representation technique. The nonlinear fatigue damage accumulation rule improves the deficiency inherent in the Miner's rule but still maintain

its simplicity in calculation. The verification with experiments shows that the proposed fatigue damage accumulation rule improves the mean value of the fatigue life prediction while only using the similar computational effort as that of the Miner' rule.

A new uncertainty modeling method for fatigue S-N curve representation is proposed. It uses the Karhunen-Loeve expansion technique to consider the covariance structures within different stress levels. It is shown that the available probabilistic fatigue life prediction methods are two special cases of the proposed method, which implicitly assume that the covariance function is either zero or unity. The verification with experiments shows that ignoring the covariance of the input variables results in different variance predictions of the fatigue life. The difference is especially significant at the low failure probability stage, which is of more interest for practical design and maintenance decision with respect to fatigue.

Compared with traditional fatigue life prediction methods (i.e. using linear damage accumulation rule and ignoring the covariance of input random variables), the proposed methodology requires only one additional set of experimental data under variable loading. The benefits are achieved both in the accuracy of the mean value and variance prediction of the fatigue life.

The proposed methodology is suitable and validated for stationary variable loading and certain types of non-stationary variable loading (step loadings). For general non-stationary variable loadings, further research work is required both for model development and experimental validation. The current validation is only for uniaxial loading. The proposed methodology needs to be extended to general multiaxial loading.

The proposed fundamental multiaxial fatigue analysis methodology is applied to railroad wheels. Both the fatigue crack initiation and propagation life are included in the current study. A response surface method combined with the Monte Carlo simulation technique is used. Several important factors affecting the fatigue life are used for the design of experiments. Field data on the fatigue properties, material properties, wheel geometry and crack profile are collected and analyzed to obtain the statistics for the reliability analysis. Numerical predictions are compared with field failure data and shows excellent agreements.

CHAPTER V

CONCLUSIONS AND FUTURE WORK

The multiaxial fatigue problem is much more complex compared with commonly studied uniaxial fatigue problem. It has been an activate research topic in the past two decades. In the current study, fundamental modeling for multiaxial fatigue problems is investigated in detail. A new approach based on the characteristic plane approach is proposed. Most of the existing critical plane-based models can only be applied to individual types of failure modes, i.e. shear dominated failure or tensile dominated failure. Their applicability generally depends on the material's properties and loading conditions. In the proposed model, the characteristic plane changes corresponding to different material failure modes, thus making the proposed model have almost no applicability limitation with respect to different metals. A useful mechanical parameter is found during the development of the proposed model. The ratio of torsional fatigue strength and uniaxial fatigue strength s appears to be very important for the multiaxial fatigue problem. According to the proposed multiaxial fatigue theory and the experimental data collected in this study, different material failure modes may be related to this parameter. Also, from the experimental results collected from the literature, this parameter shows a good correlation to the extra hardening of the material caused under nonproportional loading.

Due to the unique nature of the proposed multiaxial theory, i.e. not based on the specific failure mode and certain microstructure, it has a great potential to be applied to

many new engineering materials, such as anisotropic composites and inhomogeneous functionally graded materials. In this paper, the proposed model has been extended to isotropic materials and compared with experimental results for unidirectional and multidirectional composite laminates. Future work is needed to extend the proposed model to inhomogeneous material.

A general methodology is proposed to apply the developed multiaxial fatigue theory to the structural/component level, specifically the wheel/rail rolling contact fatigue. Non-linear finite element analysis is used for stress computation and a submodeling technique is used to improve the efficiency and accuracy. The finite element results are then used to calculate the fatigue life. Numerical examples are implemented and compared with field observation of failure pattern. The effect of several parameters on the fatigue damage in railroad wheels is studied using the proposed model.

A general methodology for probabilistic multiaxial fatigue life prediction is still lacking in the open literature. The current study focuses on the uncertainty modeling of the fatigue damage accumulation process. A simulation based calculation procedure is proposed for the multiaxial fatigue life prediction, which combines stochastic process theory, response surface method and Monte Carlo simulation technique. The proposed method can include various types of randomness from material property, applied loading and geometry. Field failure statistics is compared with numerical prediction and very good agreement is obtained.

For fundamental multiaxial fatigue damage modeling, future work is required to explore the fatigue behavior of materials at a smaller scale. The present work focuses on the mesoscopic and macroscopic scale, i.e. from physically small crack to macro crack. It

appears that the multiaxial fatigue is controlled by two dominated failure mechanisms (shear failure and tensile failure). The microstructure effects, such as grain size, grain orientation and grain boundary, on the multiaxial fatigue behavior are still not fully understood.

Various fatigue models available in the open literature are developed a wide range of scales within the engineering context, such as structural level (i.e. steel bridges), component level (i.e. engine blades and shaft bearings), material level (i.e. small specimen tests) and microstructural level (i.e. grain and subgrain fatigue crack analysis). A general framework for integrating models at multiple lengths is still lacking, especially in the context of uncertainty, such as the uncertainty propagation from one length scale to the other. Both the physics and the uncertainty propagation are quite different across different length scales. From this point of view, an integration of both deterministic and probabilistic methods is desired.

The proposed fatigue reliability evaluation method of rail/wheel rolling contact problem is seen to agree with the failure pattern observed in the field and can capture the major trend in the reliability variation. However, a noticeable difference exists at the shorter fatigue life regime, i.e. the tail region of the CDF of the fatigue life. It indicates that some other effects may contribute to the rare early failure of railroad wheels, such as brake loading, thermal loading and initial defects. These effects need to be explored in the future.

The results in this study can be used to develop reliability-based inspection planning to prevent the shattered rim failure. Sensitivity analysis and field data cluster analysis are required to identify the most important factors affecting the wheel reliability.

Proper inspection techniques, sampling methods and optimization theory need be combined with the present numerical prediction methodology to develop a general methodology for optimized inspection procedure.

REFERENCES

[1] Akberg, A., "Rolling Contact Fatigue of railway Wheels-Computer Modelling and In-field Data." *Proceedings of 2nd Miniconference on Contact Mechanics and Wear of Rail/Wheel Systems*, Budapest, Hungary, pp.154-163, 1996.

[2] Ansys, "ANSYS Theory Reference, release 7.0", ANSYS, Inc., 2003.

[3] ASME, Cases of ASME Boiler and Pressure Vessel Code, Code Case N-47-12, American Society of Mechanical Engineers, New York, 1979.

[4] Association of American Railroads, "Manual of Standards and Recommended Practices: Section G-Wheels and Axles", Issue of 1998.

[5] Bannantine, J.A., Socie, D.F. "A variable amplitude multiaxial fatigue life prediction method". In: Kussmaul K, McDiarmid D, Socie D, editors. ESIS10. London: Mechanical Engineering Publications, pp. 35–51,1991.

[6] Banvillet, A., Łagoda, T., Macha, E., Niesłony, A., Palin-Luc T., and Vittori, J.F., "Fatigue life under non-Gaussian random loading from various models", *International Journal of Fatigue*, Vol. 26, pp.349-363, 2004.

[7] Benasciutti, D., and Tovo, R., "Spectral methods for lifetime prediction under wide-band stationary random processes", *International Journal of Fatigue*, Vol. 27, pp.867-877, 2005.

[8] Berge, S., "Shattered Rim Fracture Research", *Proceedings of 2000 Brenco Rail Conference*, October 19-20, 2000, LaQuinta, California.

[9] Bhargava, V., Hahn, G.T., Rubin, C.A., "An elastic–plastic finite element model of rolling contact", *ASME J Appl Mech*, Vol 52, pp. 66–82, 1985.

[10] Biner, S. "Fatigue crack growth studies under mixed-mode loading", *International Journal of Fatigue*, Vol. 23, pp. 259–263, 2001.

[11] Bogdanoff, J.L., Kozin, F., Probabilistic models of cumulative damage, New York, NY: John Wiley & Sons, 1985.

[12] Bold, P.E., Brown, M.W. and Alle,n R.J. "A review of fatigue crack growth in steels under mixed mode I and II loading", *Fatigue & Fracture of Engineering Materials and Structures*, Vol. 15, pp. 965-977, 1992.

[13] Bond, I.P., "Fatigue life prediction for GRP subjected to variable amplitude loading", Composite Part A, *Appl Sci and Manuf*, Vol.30, pp.363-367, 1999.

[14] Bonacuse, P.J., Kalluri, S., "Elevated temperature axial and torsional fatigue behavior of Haynes 188", NASA Center for AeroSpace Information (CASI) NASA-TM-105396; E-6788; NAS 1.15:105396; AVSCOM-TR-91-C-045, 19920601, 1992.

[15] Borodii, M.V., Kucher, N.K., Strizhalo, V.A. "Development of a constitutive model for biaxial low-cycle fatigue", *Fatigue Fract. Engng. Mater. Struct.,* Vol. 19, pp. 69–1179, 1996.

[16] Borodii, M.V. and Strizhalo, V.A., "Analysis of the experimental data on a low cycle fatigue under nonproportional straining", *Int. J. Fatigue*, Vol 22, Issue 4, pp. 275-282, 2000.

[17] Box, G., Wilson K.B. "The exploration and exploitation of response surfaces: some general considerations and examples", *Biometrics*, Vol. 10, pp.16–60, 1954.

[18] Brown, M.W., Miller, K.J., "Two decades of progress in the assessment of multiaxial low-cycle fatigue life", In: Amzallag, C., Leis, B., Rabbe, P., editors. Low-cycle fatigue and life prediction, ASTM STP 770. Philadelphia: ASTM; pp. 482–499, 1982.

[19] Brown, M.W., Miller, K.J. "A theory for fatigue failure under multiaxial stress–strain conditions", *Proc Inst Mech Engrs*, Vol 187, pp. 745–755, 1973.

[20] Bucher, C.G., Bourgund, U., "A fast and efficient response surface approach for structural reliability problems", *Structural Safety*, Vol. 7, pp.57–66, 1990.

[21] Caprino, G., D'Almore, A., and Facciolo, F., "Fatigue sensitivity of random glass fibre reinforced plastics", *Journal of Composite Material*, Vol.32, pp.1203-1220, 1999.

[22] Carpinteri, A., Spagnoli, A., "Multiaxial high-cycle fatigue criterion for hard metals", *Int. J. Fatigue*, Vol. 23, pp. 135-145, 2001.

[23] Carpinteri, A., Macha, E., Brighenti, R., Spagnoli, A., "Expected fracture plane for multiaxial random stress state - Part I: Theoretical aspects of the weight function method", *Int. J. Fatigue*, Vol. 21, pp. 83-88, 1999a.

[24] Carpinteri, A., Macha, E., Brighenti, R., Spagnoli A., "Expected fracture plane for multiaxial random stress state - Part II: Numerical simulation and experimental assessment through the weight function method", *Int. J. Fatigue*, Vol. 21, pp. 89-96, 1999b.

[25] Chambers, A.C., Hyde, T.H. and Webster, J.J. "Mixed mode fatigue crack growth at 550[deg]c under plane stress conditions in Jethete M152", *Engineering Fracture Mechanics*, Vol. 39, pp.603-619, 1991.

[26] Chao, Y.J. and Liu, S. “On the failure of cracks under mixed-mode loads”, *International Journal of Fracture*, Vol. 87, pp.201-223, 1997.

[27] Chaudonneret, M., “A simple and efficient multiaxial fatigue damage model for engineering applications of macro-crack initiation”, *Journal of Engineering Materials and Technology*, Vol. 115, pp. 373-379, 1993.

[28] Chen, X., Xu, S., Huang, D. “A critical plane-strain energy density criterion for multiaxial low-cycle fatigue life under non-proportional loading”, *Fatigue Fract Eng Mater Struct*, Vol 22, pp.679–686, 1999.

[29] Chen, X., An, K., and Kim, K.S., “Low-cycle fatigue of 1Cr-18Ni-9Ti stainless steel and related weld metal under axial, torsional and 90° out-of-phase loading”, *Fatigue Fract Eng Mater Struct*, Vol 27, pp. 439-448, 2004.

[30] Cheng, G. and Plumtree, A., “A fatigue damage accumulation model based on continuum damage mechanics and ductility exhaustion”, *International Journal of Fatigue*, Vol. 20, pp. 495-501, 1998.

[31] Chu, C.C., Conle, F.A., Bonnen, J.J., “Multiaxial stress–strain modeling and fatigue life prediction of SAE axle shafts”, In: McDowell DL, Ellis R, editors. Advances in multiaxial fatigue, ASTM STP 1191. Philadelphia: ASTM; pp. 37–54, 1993.

[32] Cotterell, B. and Rice, J.R. “Slightly curved or kinked cracks”, *International Journal of Fracture*, Vol. 16, pp.155-169, 1980.

[33] Crossland, B., “Effect of large hydrostatic pressures on the torsional fatigue strength of an alloy steel”, In: *Proceedings of the International Conference on Fatigue of Metals, Institution of Mechanical Engineers*, London. pp. 138–149, 1956.

[34] Daniel, I.M., and Ishai, O., “Engineering Mechanics of Composite Materials”, Oxford University Press, New York, 1994.

[35] Dang Van, K., et al., “Criterion for High Cycle Fatigue Failure under Multiaxial Loading,in Biaxial and Multiaxial Fatigue”, Mechanical Engineering Publications, London, pp. 459-478, 1989.

[36] Davoli, P., Bernasconi, A., Filippini, M., Foletti, S. and Papadopoulos, IV., “Independence of the torsional fatigue limit upon a mean shear stress”, *Int. J. Fatigue*, Vol. 25, Issue 6, pp. 471-480, 2003.

[37] Degrieck J., and Van Paepegem W., “Fatigue Damage Modelling of Fibre-Reinforced Composite Materials: Review”, Applied Mechanics Reviews, Vol.54, No.4, pp.279-300, 2001.

[38] Devine, T.J., Alber, R.H., “Wheel flange wear test results in heavy haul service”, *Second International Heavy Haul Railway Conference*, 1982.

[39] Diao, X., Lessard, L., Shokrieh, M., “Statistical model for multiaxial fatigue behavior of unidirectional plies”, *Compos Sci Technol*, Vol 59, pp.2025–2035, 1999.

[40] Doong, S.H., Socie, D.F., “Constitutive modeling of metals under nonproportional cyclic loading”, *J Engng Mater Tech*, Trans ASME, Vol 113, pp. 23–30, 1991.

[41] Ekberg, A., E. Kabo, and H. Andersson., “An engineering model for prediction of rolling contact fatigue of railway wheels”, *Fatigue & Fracture of Engineering Materials and Structures*, Vol. 25, pp. 899-909, 2002.

[42] Ekberg. A., “Rolling contact fatigue of railway wheels – towards tread life prediction through numerical modelling considering material imperfections, probabilistic loading and operational data”, PhD-thesis, Chalmers University of Technology, Department of Solid Mechanics, Göteborg, Sweden, 2000.

[43] Ekberg, A. and Marais, J., “Effects of imperfections on fatigue initiation in railway wheels”, IMechE, *Journal of Rail and Rapid Transit*, Vol. 214, pp. 45–54, 1999.

[44] Ekberg A. “Rolling contact fatigue of railway wheels - computer modelling and in-field data”, in *Proc. 2nd miniconference on Contact Mechanics and Wear of Rail/Wheel Systems*, Budapest, Hungary, pp.154-163, 1996

[45] Ekberg, A., Bjarnehed, H. and Lundén, R., “A Fatigue Life Model for General Rolling Contact with Application to Wheel/Rail Damage”, *Fatigue & Fracture of Engineering Materials & Structures*, Vol. 18, Issue 10, pp. 1189-1199, 1995.

[46] El Haddad, M.H., Topper, T.H., Smith K.N., “Prediction of nonpropagating cracks”, *Engineering Fracture Mechanics*, Vol. 11, pp.573-584, 1979.

[47] Ellyin, F., Xia, Z., “A general fatigue theory and its application to out-of-phase cyclic loading”, *J Eng Mater Technol*, Trans ASME, Vol 115, pp. 411–416, 1993.

[48] Ellyin, F., Golos, K., Xia, Z., “In-phase and out-of-phase multiaxial fatigue”, *J Eng Mater Technol*, Trans ASME, Vol 113, pp. 112–118, 1991.

[49] Ellyin, F., and Valarie, B., “High strain multiaxial fatigue,” *J Eng Mater Technol*, Trans ASME, Vol. 104, pp. 165-173, 1982.

[50] Erdogan, F. and Sih, G.C. “On the Crack Extension in Plates under Plane Loading and Transverse Shear,” *Journal of Basic Engineering*, Vol.85, pp. 519-527, 1963.

[51] Farahani, A.V., "A new energy critical plane parameter for fatigue life assessment of various metallic materials subjected to in-phase and out-of-phase multiaxial fatigue loading conditions", *Int. J. Fatigue*, Vol 22, pp. 295–305, 2000.

[52] Fatemi, A, Socie, D.F., "A critical plane approach to multiaxial fatigue damage including out of phase loading", *Fatigue Fract Eng Mater Struct,* Vol.11, pp.149–65,1988.

[53] Fateri, A., Stephens, RI., "Biaxial Fatigue of 1045 Steel Under In-Phase and 90 Deg Out-of-Phase Loading Conditions", In: Leese GE, Socie DF, editors. Multiaxial fatigue: analysis and experiments, SAE, AE-14. Warrendale: SAE, pp. 121-138, 1989.

[54] Fawaz, Z. and Ellyin, F., "Fatigue damage model for fiber-reinforced materials under general loading conditions", *Journal of Composite Material*, Vol.28, pp.1432-1451, 1994.

[55] Feng, M., Ding, F. and Jiang, Y., "A study of loading path influence on fatigue crack growth under combined loading", *International Journal of Fatigue*, Vol. 28, pp. 19-27, 2006.

[56] Findley, W.N., "A theory for the effect of mean stress on fatigue of metals under combined torsion and axial load or bending", *J Eng Ind*, Trans ASME, Vol. 81, Issue 4, pp. 301–306, 1959.

[57] Forth, S.C., Favrow, L.H., Keat W.D., and Newman J.A. "Three-dimensional mixed-mode fatigue crack growth in a functionally graded titanium alloy", *Engineering Fracture Mechanics*, Vol. 70, pp.2175-2185, 2003.

[58] Fong, J.T., "what is fatigue damage?", in Reifsnider KL (ed.), Damage in composite materials. ASTM STP 775, American Society for Testing and Materials, pp.243-266, 1982.

[59] Fround M.S., "Multiaxial Fatigue", ASTM STP 853 (Eds K.J. Miller and M.W. Brown) American Society for Testing and Materials, Philadelphia, pp.381-395, 1985.

[60] Fu, T.T., and Cebon, D., "Predicting fatigue lives for bi-modal stress spectral densities", *International Journal of Fatigue*, Vol. 22, pp. 11-21, 2000.

[61] Gao H., Brown M.W. and Miller K.J. "Mixed-mode fatigue thresholds", *Fatigue of Engineering Materials and Structures*, Vol. 5, No. 1, pp.1-17, 1982.

[62] Garud, Y.S. "A new approach to the evaluation of fatigue under multiaxial loadings", Methods for Predicting material life, ASME, pp.247-263, 1979.

[63] Garud, Y.S., "Multiaxial fatigue: a survey of the state-of-the-art", *J Test Evaluation*, Vol 9, Issue 3, pp.165–78, 1981.

[64] Gerber, H., "Bestimmung der zulassigen Spannungen in Eisen-konstructionen. Zeitschrift des Bayerischen Architeckten und ingenieur-Vereins", Vol 6, pp. 101-10, 1874.

[65] Ghanem, R., "Stochastic Finite Elements with Multiple Random Non-Gaussian Properties", *Journal of Engineering Mechanics*, pp. 26-40, 1999.

[66] Ghanem R., and Spanos P., "Stochastic finite elements: A spectral approach", Springer, N.Y., 1991.

[67] Giammarise, A. W., and Gilmore, R. S. "Wheel Quality: A North American Locomotive Builder's Perspective", GE Research & Development Center, CRD140, Sep, 2001.

[68] Gimenez, J.G., and H. Sobejano., "Theoretical approach to the crack growth and fracture of wheels", *11th International Wheelset Congress*. Paris: 15-20. 1995.

[69] Goodin, E., Kallmeyer, A., Kurath, P., "Evaluation of Nonlinear Cumulative Damage Models for Assessing HCF/LCF Interactions in Multiaxial Loadings", *Proceedings of the 9th National Turbine Engine High Cycle Fatigue (HCF) Conference*, March 16-19, Pinehurst, NC, 2004.

[70] Goodman, J. Mechanics Applied to Engineering. London: Longmans Green, 1899.

[71] Gordon, J., and Perlman, A. B., "Estimation of Residual Stresses in Railroad Commuter Car Wheels Following Manufacture", *Proceedings, International Mechanical Engineering Congress and Exhibition*, ASME RTD Vol. 15, pp.13 – 18, 1998.

[72] Gough, H.J., Pollard, H.V., "The strength of metals under combined alternating stress", *Proc Inst Mech Engrs*, Vol, 131, pp. 3–18, 1935.

[73] Gough, H.J., Pollard, H.V., Clenshaw, W.J., "Some experiments on the resistance of metals to fatigue under combined stresses", Aeronautical Research Council Reports, R and M 2522, London: HMSO, 1951.

[74] Grigoriu, M, "On the spectral representation in simulation", *Prob Engng Mech*, Vol. 8, No. 2, pp. 75-90, 1993.

[75] Grubisic, V, Simbu¨rger, A., "Fatigue under combined out-of-phase multiaxial stresses." *International Conference on Fatigue, Testing and Design*. Society of Environmental Engineers, London, Vol 27, pp.1–27, 1976.

[76] Guo, Y. B. and Barkey, Mark E., "Modeling of rolling contact fatigue for hard machined components with process-induced residual stress", *Int. J. Fatigue*, Vol. 26, Issue 6, pp. 605-613, 2004.

[77] Gupta, V., Bastias, P., Hahn, G.T., Rubin, C.A., "Elasto-plastic finite element analysis of 2-D rolling plus sliding contact with temperature dependent bearing steel material properties", *Wear*, Vol 169, pp. 251–256, 1993.

[78] Hahn, G.T., Bhargava, V., Rubin, C.A., Chen, Q., Kim, K., "Analysis of the rolling contact residual stresses and cyclic plastic deformation of SAE 52100 steel ball bearings", *ASME J Tribology*, Vol 109, pp. 618–626, 1987.

[79] Halford, G.R. and Manson, S.S., "Reexamination of cumulative fatigue damage laws", Structure Integrity and Durability of Reusable Space Propulsion Systems, NASA CP-2381, pp. 139-145,1985.

[80] Halford, G.R., "Cumulative fatigue damage modeling—crack nucleation and early growth", *International Journal of Fatigue*, Vol. 19, pp.253-260, 1997.

[81] Hanlon, D.N., Rainforth, W.M., Sellars, C.M., "The effect of processing route, composition and hardness on the wear resistance of chromium bearing steels in a rolling–sliding configuration", *Wear*, pp. 220–229, 1997.

[82] Haris, B., "Fatigue behavior of polymer-based composite and life prediction methods", AIB-Vincotte Leerstoel, 2 maart 1995, Belgium, National Fonds voor Wetenschappelijk Onderzoek, 28p, 1985.

[83] Hasin, Z., Rotem, A., "A fatigue criterion for fiber reinforced composite material", *Journal of Composite Materials*, Vol.7, pp.448-464, 1973.

[84] Howell, M., Hahn, G.T., Rubin, C.A., McDowell, D.L., "Finite element analysis of rolling contact for nonlinear kinematic hardening bearing steel", *ASME J Tribology*, Vol 117, pp. 729–736, 1995.

[85] Huang, S.P., Quek, S.T., and Phoon, K.K., "Convergence study of the truncated Karhunen-Loeve expansion for simulation of stochastic processes", *International Journal for Numerical Methods in Engineering*, Vol. 52, pp. 1029-1043, 2001.

[86] Hwang, W. and Han, K.S., "Cumulative models and multi-stress fatigue life prediction", *Journal of Composite Material*, Vol.20, pp.125-153, 1986(a).

[87] Hwang, W. and Han, K.S., "Fatigue of composite- Fatigue modulus concepts and life prediction", *Journal of Composite Material,* Vol.20, pp.154-165, 1986(b).

[88] Inglis, C.E., "Stresses in a plate due to the presence of cracks and sharp corners" *Transactions of the Institute of Naval Architects*, Vol. 55, pp. 219-241, 1913.

[89] Isakov, E., "Mechanical Properties of Work Materials", Hanser Gardner Publications, 2000.

[90] Itoh, T., Sakane, M., Ohnami, M., Socie, D.F. "Nonproportional low cycle fatigue criterion for type 304 stainless steel", *J. Eng. Mater. Technol. Trans ASME*, Vol. 117, pp. 285–292, 1995.

[91] Jayaraman, N., Ditmars, M.M. "Torsional and biaxial (tension–torsion) fatigue damage mechanisms in Waspaloy at room temperature", *Int. J. Fatigue*, Vol 11, pp. 309–318, 1989.

[92] Jen, M.H.R. and Lee, C.H., "Strength and life in the thermaloplastic composite laminates under static and fatigue loads", *Int. J. Fatigue*, Vol.20, pp.605-615, 1998.

[93] Jiang, Y, Sehitoglu, H., "A model for rolling contact failure", *Wear*, Vol. 224, pp. 38–49, 1999.

[94] Jiao, G., "A theoretical model for the prediction of fatigue under combined Gaussian and impact loads", *International Journal of Fatigue*, Vol. 17, pp.215-219, 1995.

[95] Johnson, K.L., "The strength of surfaces in rolling contact", *Proceedings of the Institution of Mechanical Engineers (IMechE)*, Vol. 203, pp. 151–163, 1989.

[96] Johnson, K.L., "Contact mechanics", Cambridge University Press, 1985.

[97] Johnson, M., Moore, L. and Ylvisaker, D. "Minimax and Maximin Distance Designs", *Journal of Statistical Planning and Inference*, Vol. 26, pp.131-148, 1990.

[98] Jordan, E.H., "Elevated temperature biaxial fatigue", NASA Center for AeroSpace Information (CASI), NASA-CR-175009; NAS 1.26:175009 , 19851001, 1985.

[99] Kadi, E.l., Ellyin, H.F. "Effect of stress ratio on the fatigue of unidirectional glass fibre/epoxy composite laminae", *Composites*, Vol, 25, pp.917–924, 1994.

[100] Kakuno, H., Kawada, Y., "A new criterion of fatigue strength of a round bar subjected to combined static and repeated bending and torsion", *Fatigue Eng Mater Struct*, Vol 2, Issue 2, pp.229-236, 1979.

[101] Kam, T.Y., Chu, K.H., and Tsai, S.Y., "Fatigue reliability evaluation for composite laminates via a direct numerical integration technique", *International Journal of Solids and Structures*, Vol. 35, pp. 1411-1423, 1998.

[102] Kaminski, M., "On probabilistic fatigue models for composite materials", *International Journal of Fatigue*, Vol. 22, pp. 477-495, 2002.

[103] Kandil, F.A., Brown, M.W., Miller, K.J., "Biaxial low cycle fatigue fracture of 316 stainless steel at elevated temperatures", The Metal Society, London, Vol 280, pp. 203–210, 1982.

[104] Kakuno, H., Kawada, Y., "A new criterion of fatigue strength of a round bar subjected to combined static and repeated bending and torsion", *Fatigue Eng Mater Struct*, Vol 2, Issue 2, pp.229-236, 1979.

[105] Kallmeyer, A.R. , Ahmo, K., and Kurath, P., "Evaluation of Multiaxial Fatigue Life Prediction Methodologies for Ti-6Al-4V", *J Eng Mater Technol*, Trans ASME, Vol 124, pp. 229-237, 2002.

[106] Kalluri, S., Bonacuse, P.J., "In-phase and out-of-phase axial-torsional fatigue behavior of Haynes 188 at 760 C", NASA Center for AeroSpace Information (CASI), NASA-TM-105765; E-7182; NAS 1.15:105765; AVSCOM-TR-91-C-046; Symposium on Multiaxial Fatigue, San Diego, CA, United States, 19911001, 1991.

[107] Kanazawa, K., Miller, K.J., Brown, M.W., "Low-cycle fatigue under out-of-phase loading conditions", *J Eng Mater Technol*, Trans ASME, Vol 99, pp. 222–228, 1977.

[108] Kanazawa, K., Miller, K.J., Brown, M.W., "Cyclic deformation of 1% Cr–Mo–V steel under out-of-phase loads", *Fatigue Fract Eng Mater Struct*, Vol 2, pp. 217–228, 1979.

[109] Kawai, M., Hachinohe, A., Takumida, K., Kawase, Y., "Off-axis fatigue behaviour and its damage mechanics modelling for unidirectional fibre–metal hybrid composite: GLARE 2", *Composites: Part A*, Vol. 32, pp. 13–23, 2001.

[110] Kawai, M., "A phenomenological model for off-axis fatigue behavior of unidirectional polymer matrix composites under different stress ratios", *Composites: Part A*, Vol. 35, pp. 955–963, 2004.

[111] Kawai, M., Suda, H., "Effects of Non-Negative Mean Stress on the Off-Axis Fatigue Behavior of Unidirectional Carbon/Epoxy Composites at Room Temperature", *Journal of Composite Materials*, Vol. 38, pp. 833-854, 2004.

[112] Khuri, AI, Cornell, JA. Response surfaces: design and analyses. New York: Marcel and Dekker; 1997.

[113] Kim, K.S., Park, J.C., Lee, J.W., "Multiaxial fatigue under variable amplitude loads", *J Eng Mater Technol*, Trans ASME, Vol 121, pp. 286–293, 1999.

[114] Kim, K.S., Nam, K.M., Kwak, G.J. and Hwang, S.M., "A fatigue life model for 5% chrome work roll steel under multiaxial loading", *Int. J. Fatigue*., In Press, Corrected Proof, Available online 3 February 2004.

[115] Kitagawa, H. and Takahashi, S. “Applicability of fracture mechanics to vary small cracks or cracks in early stage. In: Proceedings of 2nd International Coference on Mechanical behavior of Materials. Metal Park (OH,USA): ASM International, pp. 627-631, 1976.

[116] Kopnov, V.A., “A randomized endurance limit in fatigue damage accumulation models”, *Fatigue & Fracture of Engineering Materials and Structures,* Vol. 16, pp. 1041-1059, 1993.

[117] Kopnov, V.A., “Intrinsic fatigue curves applied to damage evaluation and life prediction of laminate and fabric material”, T*heoretical and Applied Fracture Mechanics*, Vol. 26, pp.169-176, 1997.

[118] Kujawski, D. and Ellyin, F. “A unified approach to mean stress effect on fatigue threshold conditions”, *International Journal of Fatigue,* Volume 17, Issue 2, pp. 101-106, 1995.

[119] Kurath, P., Downing, S.D., Galliart, D., “Summary of non-hardened notched shaft round robin program”, In: Leese GE, Socie DF, editors. Multiaxial fatigue: analysis and experiments, SAE, AE-14. Warrendale: SAE; pp. 12–32. 1989

[120] Landau, L.D. and Lifschitz, E.M., “Mechanics”, 3rd ed. Oxford, England, Pergamon Press, 1976.

[121] Langer, B.F. Design of Pressure Vessels Involving Fatigue, Pressure Vessel Engineering (Edited By Nichols, R.W.), Elsevier, Amsterdam, pp. 59-100, 1979.

[122] Lawson, L., Chen, E.Y. and Meshii, M., “Near-threshold fatigue: a review”, *International Journal of Fatigue*, Vol. 21, pp.15-34, 1999.

[123] Le, X., and Peterson, M.L., “A method for fatigue based reliability when the loading of a component is unknown”, *International Journal of Fatigue*, Vol. 21, pp. 603-610, 1999.

[124] Learch, B.A., Jayaraman, A., and Antolovice, S.D., “A study of fatigue damage mechanism in Waspaloy from 25 to 800.C”, *Materials Science and Engineering*, Vol 66, pp. 151-166, 1984.

[125] Lee S-B., “Out-of-phase bending and torsion fatigue of steels”, In: Brown MW, Miller KJ, editors. Biaxial and multiaxial fatigue, EGF3, London: Mechanical Engineering Publications, pp. 612–634, 1989.

[126] Lee, B.L., Kim, K.S. and Nam, K.M., “Fatigue analysis under variable amplitude loading using an energy parameter”, *Int. J. Fatigue*, Vol 25, Issue 7, pp. 621-631, 2003.

[127] Lemaire, M. Finite element and reliability: combined methods by response surface. In: Frantziskonis GN. editor, PROBAMAT-21st century: probabilities

and materials. Tests, models and applications for the 21st century, vol. NATO ASI series 3. High technology, vol. 46. Kluwer Academic;317–31, 1998.

[128] Liao, M., Xu, X., and Yang, Q.X., "Cumulative fatigue damage dynamic interference statistical model", *International Journal of Fatigue*, Vol. 17, pp.559-566, 1995.

[129] Lin, H., Nayeb-Hashemi, H., Pelloux, R.M., "A multiaxial fatigue damage model for orthotropic materials under proportional loading", *Fatigue Fract Eng Mater Struct*, Vol 16, pp. 723–742, 1993.

[130] Liu, J, Zenner, H., "Berechnung der Dauerschwingfestigkeit bei mehrachsiger Beanspruchung", Mat-wiss u Werkstofftech, Vol 24, pp. 240–249, 1993.

[131] Liu, P. and Wang, Z., "Mixed-mode I and II fatigue threshold and crack deflection angle in SiCp/2024Al composite", *Scripta Materidia*, Vol. 34, No. 8, pp. 1323-1330, 1996.

[132] Liu, Y., Mahadevan, S., "Multiaxial High-Cycle Fatigue Criterion and Life Prediction for Metals", *International Journal of Fatigue*, Vol. 7, Issue 7, pp. 790-800, 2005(a).

[133] Liu, Y., Mahadevan, S., "Probabilistic Fatigue Life Prediction of Multidirectional Composite Laminates", *Composite Structures*, Vol. 69, pp.11-19, 2005(b).

[134] Liu Y, Stratman B, Mahadevan S. "Fatigue crack initiation life prediction of railroad wheels", International Journal of Fatigue, 2006. (in press)

[135] Liu, Y.W., Moses F., "A sequential response surface method and its application in the reliability analysis of aircraft structural systems", *Structural Safety*, Vol.16, pp.39–46, 1994.

[136] Lohr, R.D., Ellison, E.G., "A simple theory for low cycle multiaxial fatigue", *Fatigue Fract Eng Mater Struct*, Vol 3, pp. 1–17, 1980.

[137] Loeve M, Probability Theory, 4th Ed., Springer, New York, 1977.

[138] Lovelace, W.S., "Study of rim stresses resulting from static loads on different 36-inch railroad wheel designs", IEEE-ASME Joint Railroad Conference, New York, 1971.

[139] Macha E., "Simulation investigations of the position of fatigue fracture plane in materials with biaxial loads", Mat.-wiss.u.Werk-stofftech, Vol 20, pp. 132-136 and pp. 153-163, 1989.

[140] Macha, E., Sonsino, C.M., "Energy criteria of multiaxial fatigue failure", *Fatigue Fract Eng Mater Struct*, Vol 22, pp. 1053–1070, 1999.

[141] Mandell, J.F., and Samborsky, D.D., "DOE/MSU Composite Materials Fatigue Database: Test Methods, Materials, and Analysis", Sandia National Laboratories, Albuquerque, NM, Feb, 2003.

[142] Manson. S.S. and Halford, G.R., "Practical implementation of the double linear damage rule and damage curve approach for treating cumulative fatigue damage", *International Journal of Fracture*, Vol. 17, pp.169-192, 1981.

[143] Mao, H., Mahadevan, S., "Fatigue damage modelling of composite materials", *Composite Structures*, Vol.58, pp.405 – 410, 2002.

[144] Marais, J.J, "Wheel failures on heavy haul freight wheels due to subsurface effects", *Proc 12th International Wheelset Congress*, Qingdao, China, pp. 306-314, 1998.

[145] Marais, J.J., and P. G. H. Pistorius., "Terminal fatigue of tires on urban transport service", *4th International Conference of Contact Mechanics and Wear of Rail/Wheel Systems (preliminary proceedings)*, Vancouver, 1994.

[146] Marco, S.M. and Starkey, W.L., "A concept of fatigue damage", *Transaction of the ASME*, Vol. 76, pp. 627-632, 1954.

[147] Matake, T., "An explanation on fatigue limit under combined stress", *Bull JSME*, Vol 20, pp. 257-263, 1977.

[148] McDiarmid, DL., "Fatigue under out-of-phase bending and torsion", *Fatigue Engng Mater Struct*, Vol 9, Issue 6, pp. 457–75, 1987.

[149] McDowell, D.L., Socie, D.F., Lamba, H.S. (1982) Multiaxial nonproportional cyclic deformation. Low-cycle Fatigue and Life Prediction, ASTM STP770, 500–518.

[150] McEvily, A.J., "On Closure in Fatigue Crack Growth" ASTM STP 982, American Society for testing and Materials, Philadelphia, pp. 35-43, 1988.

[151] Miner, M. A., "Cumulative damage in fatigure", *Journal of Applied Mechunics*, Vol. 67, A159-A164, 1945.

[152] Moyar, G.J., and Stone, D.H., "An analysis of the thermal contributions to railway wheel shelling", *Wear*, Vol. 144, pp. 117-138, 1991.

[153] Morrow J.D., "Fatigue design handbook-Advances in Engineering", Vol. 4, Sec. 3.2, pp.21-29, Warrendale, PA: Society of Automotive Engineers, 1968.

[154] Mutton, P.J., Epp, C.J. and Dudek, J., "Rolling contact fatigue in railway wheels under high axle loads", *Wear*, Vol. 144, pp. 139-152, 1991.

[155] Myers, R.H., Montgomery, D.C., Response surface methodology: process and product optimization using designed experiments. John Wiley and Sons; 1995.

[156] Nadot, Y, Mendez, J, Ranganathan, N, Beranger, S., "Fatigue life assessment of nodular cast iron containing casting defects", *Fatigue and Fracture in Engineering Materials and Structures*, Vol 22, pp.289–300, 1999.

[157] Ni, K., and Zhang, S., "Fatigue reliability analysis under two-stage loading", *Reliability Engineering & System Safety*, Vol. 68, pp. 153-158, 2000.

[158] Nelson, D.V., Rostami, A., "Biaxial fatigue of A533B pressure vessel steel", *Journal of Pressure Vessel Technology*, ASME, Vol. 119, pp.325-331, 1997.

[159] Nishihara, T, Kawamoto, M., "The strength of metals under combined alternating bending and torsion with phase difference", Memoirs College of Engineering, Kyoto Imperial University, Vol 11, Issue 5, pp. 85–112, 1945.

[160] Orringer, O., Gray, D.E. and McCown, R.J., "Evaluation of Immediate Actions Taken to Deal with Cracking Problems in Wheels of Rail Commuter Cars," Final Report, DOT/FRA/ORD-93/15, July, 1993.

[161] Otsuka, A., Mori, K. and Miyata, T., "The condition of fatigue crack growth in mixed mode condition", *Engineering Fracture Mechanics*, Vol. 7, pp. 429-439, 1975.

[162] Otsuka, A. and Tohgo, K., "Fatigue crack initiation and growth under mixed mode loading in aluminum alloys 2017-T3 and 7075-T6", *Engineering Fracture Mechanics*, Vol. 28, pp.721-732, 1987.

[163] Pascoe, K.J., and DeVilliers, J.W.R. (1967) Low-cycle fatigue of steels under biaxial strainings. *I. Strain Analysis*. 2, 117-126.

[164] Pan, W.F., Hung, C.Y., Chen, L.L., "Fatigue life estimation under multiaxial loadings", *Int. J. Fatigue*, Vol 21, pp. 3–10, 1999.

[165] Papadopoulos, IV, Davoli, P, Gorla, C, Filippini, M, Bernasconi, A., "A comparative study of multiaxial high-cycle fatigue criteria for metals", *Int, J, Fatigue*, Vol 19, Issue 3, pp. 219–35, 1997.

[166] Papadopoulos, IV., "Long life fatigue under multiaxial loading", *Int. J. Fatigue*, Vol 23, Issue 10, pp. 839-849, 2001

[167] Paris, P.C. and Erdogan, F., "A critical analysis of crack propagation law.", *Jounal of Basic Engineering*, Vol. 85, pp.528-534, 1960.

[168] Park, J. and Nelson, D., "Evaluation of an energy-based approach and a critical plane approach for predicting constant amplitude multiaxial fatigue life", *Int. J. Fatigue*, Vol 22, Issue 1, pp. 23-39, 2000.

[169] Pascual, F.G., and Meeker, W.Q., "Estimating Fatigue Curves with the Random Fatigue-Limit Model", *Technometrics*, Vol.41, pp.277-302, 1999.

[170] Petermanna, J., Plumtreeb, A., "A unified fatigue failure criterion for unidirectional laminates", *Composites: Part A*, Vol. 32, pp. 107–118, 2001.

[171] Philippidis, T.P., Vassilopoulos, R.P, "Fatigue strength prediction under multiaxial stress", *Journal of Composite Materials*, Vol.33, pp.1578-1599, 1999.

[172] Phoon, K.K., Huang, S.P., and Quek, S.T., "Simulation of non-Gaussian processes using Karhunen-Loeve Expansion", *Computers & Structures*, Vol. 80, pp. 1049-1060, 2002.

[173] Plank, R. and Kuhn, G., "Fatigue crack propagation under non-proportional mixed mode loading", *Engineering Fracture Mechanics*, Vol. 62, pp.203-229, 1999.

[174] Pook, L.P., "The fatigue crack direction and threshold behavior of mild steel under mixed Mode I and III loading", *International Journal of Fatigue*, Vol. 7, pp. 21-30, 1985.

[175] Qian, J. and Fatemi, A., "Mixed mode fatigue crack growth: A literature survey", *Engineering Fracture Mechanics*, Vol. 55, pp. 969-990, 1996.

[176] Reddy, S.C. and Fatemi, A. "Small crack growth in multiaxial fatigue", Advances in Fatigue Lifetime Predictive Techniques, ASTM STP 1122, ed. M. R. Mitchell and R. W. Landgraf. American Society for Testing and Materials, Philadelphia, PA, pp. 276-298, 1992.

[177] Reifsnider, K.L. and Gao, Z., "A micromechanics model for composite under fatigue loading", *International Journal of Fatigue,* Vol.13, pp.149-156, 1991.

[178] Ringsberg, Jonas W., "Life prediction of rolling contact fatigue crack initiation", *Int. J. Fatigue*, Vol. 23, Issue 7, pp. 575-586, 2001.

[179] Rowatt, J.D., and Spanos, P.D., "Markov chain models for life prediction of composite laminates", *Structural Safety*, Vol. 20, pp.117-135, 1998.

[180] Shang, D., and Yao, W., "A nonlinear damage cumulative model for uniaxial fatigue", *International Journal of Fatigue*, Vol. 21, pp.187-194, 1999.

[181] Shen, H., Lin, J., and Mu, E., "Probabilistic model on stochastic fatigue damage", *International Journal of Fatigue*, Vol. 22, pp.569-572, 2000.

[182] Shimokawa, T. and Tanaka, S., "A statistical consideration of Miner's rule", *International Journal of Fatigue*, Vol. 4, pp. 165-170, 1980.

[183] Shinozuka, M., and Deodatis, G., "Simulation of the stochastic process by spectral representation", *Applied Mechanics Reviews*, ASME, Vol. 44, pp. 29-53, 1991.

[184] Shokrieh, M., and Lessard, L., "Mutiaxial fatigue behavior of unidirectional plies based on uniaxial fatigue experiments-I. Modelling", *Int. J. Fatigue*, Vol. 19, pp, 201-207, 1997.

[185] Sidoroff, F. and Subagio, B., "Fatigue damage modeling of composite materials from bending tests", Sixth International Conference on Composite Materials (ICCM-VI) & Second European Conference on Composite Materials (ECCM-II), Vol.4, Proceeding.20-24, pp.432-439, July 1987, London, UK.

[186] Sih, G.C., and Macdonal, B., "Fracture Mechanics applied to engineering problems-strain energy density fracture criterion", *Engineering Fracture Mechanics*, Vol. 6, pp. 361-386, 1974(a).

[187] Sih, G.C., "Strain Energy density criterion applied to mixed mode crack problems", *International Journal of Fracture*, Vol. 10, pp. 305-321, 1974(b).

[188] Sih, G.C., Cha, B.C.K., "A fracture criterion for three dimensional crack problems", *Engineering Fracture Mechanics*, Vol. 6, pp. 699-723, 1974(c).

[189] Sih, G.C. and Barthelemy, B.M., "Mixed mode fatigue crack growth predictions", *Engineering Fracture Mechanics*, Vol. 13, pp. 439-451, 1980.

[190] Sines, G., "Behaviour of metals under complex stresses", In: Sines G, Waisman JL, editors. Metal fatigue, New York: McGraw-Hill, pp. 145–69, 1959.

[191] Sines, G., "The prediction of fatigue fracture under combined stresses at stress concentrations", *Bull Jpn Soc Mech Eng*, Vol 4, Issue 15, pp.443–53, 1961.

[192] Shokrieh, M,. and Lessard, L., "Mutiaxial fatigue behavior of unidirectional plies based on uniaxial fatigue experiments-I. Modelling", Int. J. Fatigue, Vol. 19, No. 3, pp. 201-207, 1997.

[193] Smith, J.O., "Effect of range of stress on fatigue strength of metals", University of Illinois, Engineering Experiment Station, Bull No.334, 1942.

[194] Smith, K.N., Watson, P., Topper, T.H., "A stress–strain function for the fatigue of metals", *J Mater*, Vol 5, pp. 767–78, 1970.

[195] Snyder, T., Personal communication, 2003.

[196] Socie, D., "Low-cycle fatigue and elasto-plastic behaviour of materials", Multiaxial fatigue assessment, In: Rie KT, editor. UK:Elsevier Applied Science, pp. 465-72, 1987.

[197] Socie, D., “A summary and interpretation of the Society of Automotive Engineers' Biaxial Testing Program”, In: Multiaxial fatigue: analysis and experiments. Warrendale, PA: Society of Automotive Engineers, SAE. AE-14, pp. 1~11, 1989.

[198] Socie, D, Marquis, G, editors. Multiaxial fatigue. Society of Automotive Engineers, 2000.

[199] Soderberg, C.R. “Factor safety and working stress”, Transactions of ASME, Vol. 52, pp. 13-28, 1939.

[200] Soh, A.K. and Bian, L.C. “Mixed mode fatigue crack growth criteria”, *International Journal of Fatigue*, Vol. 23, pp. 427–439, 2001.

[201] Šraml, M., Flašker, J. and Potrč, I., “Numerical procedure for predicting the rolling contact fatigue crack initiation”, *Int. J. Fatigue*, Vol. 25, Issue 7, pp. 585-595, 2003.

[202] Stone, D.H., Majumder G., Bowaj V.S., “Shattered rim wheel defects and the effect of lateral loads and brake heating on their growth”, ASME International Mechanical Engineering Congress & Exposition. New Orleans, Louisiana, 1-4, Nov, 2002.

[203] Stone, D., Lonsdale, C., and Kalay, S., “Effect of Wheel Impact Loading on Shattered Rims”, *Proc. 13th International Wheelset Congress*, Rome, 2001.

[204] Stone, D.H., and Geoffrey, E.D., “The Effect of Discontinuity Size on the Initiation of Shattered Rim Defects,” ASME Transportation Division- Vol. 19, pp. 7-14, ASME Spring 2000.

[205] Stone, D.H. and Moyar G.J., “Wheel shelling and spalling – an interpretive review”, in Rail Transportation 1989, ASME, pp.19-31, 1989.

[206] Suresh, S. Fatigue of Materials, Second Edition, Cambridge, 1998

[207] Telliskivi, T., Olofsson, U., Sellgren, U., Kruse, P., “A tool and A method for FE analysis of wheel and rail interaction”, Ansys Conference, 2000.

[208] Theocaris, P.S. and Andrianopoulos, N.P., “The T-criterion applied to ductile fracture”, *Int. J. Fracture*, Vol. 20, pp.125–130, 1982.

[209] Toshimitsu, A., Yokobori, J., Yokobori, T., Sato, K. and Syoji, K., “Fatigue crack growth under mixed modes I and II”, *Fatigue & Fracture of Engineering Materials and Structures*, Vol. 8, pp. 315-325, 1985.

[210] Tournay, H.M. and Mulder, J.M., “The transition from the wear to the stress regime”, *Wear*, Vol.191, pp.107-112, 1996.

[211] Tovo, R., "A damage-based evaluation of probability density distribution for rain-flow ranges from random processes", *International Journal of Fatigue*, Vol. 22, pp. 425-429, 2000.

[212] Tserpes, K.I., Papanikos, P., Labeas, G., and Pantelakis, S., "Fatigue damage accumulation and residual strength assessment of CFRP laminates", *Composite Structures*, Vol.63, Issue 2, pp.219-230, 2004.

[213] Van Paepegem, W., and Degrieck, J., "Numerical modelling of fatigue degradation of fibre-reinforced composite materials", Proceedings of the Fifth International Conference on Computational Structures Technology, Volume F: Computational Techniques for Materials, Composites and Composite Structures. Leuven, Belgium, 6-8 September 2000, Civil-Comp Press, pp. 319-326, 2000.

[214] Van Paepegem, W., and Degrieck, J., "Tensile and Compressive Damage Coupling for Fully-reversed Bending Fatigue of Fibre-reinforced Composites", *Fatigue and Fracture of Engineering Materials & Structures*, Vol.25, pp.547-562, 2002.

[215] Vasek, A. and Polak, J., "Low cycle fatigue damage accumulation in Armci-iron", *Fatigue of Engineering Materials and Structures*, Vol. 14, pp. 193-204, 1991.

[216] Wang, C.H., and Brown M.W., "Life prediction techniques for variable amplitude multiaxial fatigue-part1: theories", *Journal of materials and technology*, Vol. 118, pp. 367-370, 1996.

[217] Wang, D.Z., Ye, F., Liu, J., Yao, C.K., Wang, Z.G. and Yu, W.C., "Fatigue crack propagation of extruded 19V-SiCw/6061Al composite under mixed mode (I+II) loading", *Scripta Metallurgica et Materialia*, Vol. 32, pp.1637-1642, 1995.

[218] Wang YY, Yao WX., "Evaluation and comparison of several multiaxial fatigue criteria", *Int. J. Fatigue*, Vol 26, Issue 1, pp.17-25, 2004.

[219] Weertman, J., "Rate of growth of fatigue cracks calculated from theory of infinitesimal dislocation distributed on a plane", *International Journal of Fracture Mechanics*, Vol. 2, pp.460-467, 1996.

[220] Whitworth, H.A., "Evaluation of the residual strength degradation in composite laminates under fatigue loading", *Composite Structures*, Vol.48, pp.262-264, 2000.

[221] Wu, L., "Thermal and mechanical fatigue analysis of CFRP laminates", *Composite Structures*, Vol.25, pp.339-344, 1993.

[222] Wu, Y., "Experimental verification and statistical analysis of Miner's accumulative damage rule", *Chinese Journal of Aeronautics*, Vol. 6, pp. 351~360, 1985. (in Chinese)

[223] Yan, J.H., Zheng, X.L., and Zhao, K., "Prediction of fatigue life and its probability distribution of notched friction welded joints under variable-amplitude loading", *International Journal of Fatigue*, Vol. 22, pp. 481-494, 2000.

[224] Yan, X., Zhang, Z. and Du, S. "Mixed mode fracture criteria for the materials with different yield strengths in tension and compression", *Engng Fracture Mech*, Vol. 42, pp.109–116, 1992.

[225] Yao, J.T.P., Kozin, F., Wen, Y.K., Yang, J.N., Schueller, G.I. and Ditlevsen, O., "Stochastic fatigue, fracture and damage analysis", *Structural Safety*, Vol. 3, pp. 231-267, 1986.

[226] Yao, W.X. and Himmel, N., "A new cumulative damage model for fiber-reiforced plastics", *Composite Science and Technology,* Vol.60, pp.59-64, 2000.

[227] Yates, J.R. and Mohammed, R.A. "The determination of fatigue crack propagation rates under mixed mode (I+III) loading", *International Journal of Fatigue*, Vol. 18, 197-203, 1996.

[228] You, B.R., Lee, S.B., "A critical review on multiaxial fatigue assessments of metals", *Int. J. Fatigue*, Vol 18, Issue 4, pp. 235–44, 1996.

[229] Yu, J., Peter, K., Liaw, and Huang, M., "The Impact-Fatigue Fracture of Metallic Materials," *Journal of Metals*, pp: 15-18, April, 1999.

[230] Zheng, X., and Wei, J., "On the prediction of P–S–N curves of 45 steel notched elements and probability distribution of fatigue life under variable amplitude loading from tensile properties", *International Journal of Fatigue*, Vol. 27, pp. 601-609, 2005.